
Dynamics of DNA-repair factors and chromosomes studied by laser-UVA- microirradiation and laser-photobleaching

Joachim Walter



München 2003

**Dynamics of DNA-repair factors and
chromosomes studied by laser-UVA-
microirradiation and laser-photobleaching**

Joachim Walter

DISSERTATION
an der FAKULTÄT FÜR BIOLOGIE
LUDWIG-MAXIMILIANS-UNIVERSITÄT MÜNCHEN

vorgelegt von
Joachim Walter
aus Kassel

München, den 2. Juni 2003

Dissertation eingereicht am 2. Juni 2003

1. Gutachter: Prof. Dr. T. Cremer
2. Gutachter: Prof. Dr. F. Eckardt-Schupp

Tag der mündlichen Prüfung: 16. Oktober 2003

*Destruction is not negative
you must destroy to build*

from: „Zeichnungen des
Patienten OT“
Einstürzende Neubauten

Contents

LIST OF FIGURES	VIII
SUMMARY	1
1 INTRODUCTION	3
1.1 DNA double-strand break repair	3
1.1.1 Phosphorylation of H2AX marks broken chromatin.....	4
1.1.2 The Mre11-Rad50 complex.....	5
1.1.3 Rad51.....	6
1.2 Laser-UV-microirradiation	6
1.3 Nuclear architecture and dynamics	6
1.3.1 The arrangement of chromosome territories in interphase cell nuclei.....	7
1.3.2 The dynamics of nuclear proteins.....	9
1.4 Confocal microscopy	10
1.5 Questions addressed in this work	12
2 MATERIALS AND PROTOCOLS	14
2.1 Cell culture	14
2.1.1 Cell types and culture media.....	14
2.1.2 Starting a cell culture from frozen cells.....	15
2.1.3 Subcultivation of adherently growing cells.....	16
2.1.4 Seeding cells to coverslips at a defined ratio.....	17
2.1.5 Synchronization of HeLa cells with aphidicolin.....	18
2.1.6 Lipofection of GFP-Rad51 plasmid and NLS-vimentin with Pfx-1 or Fugene 6.....	18
2.2 Laser-UVA-microirradiation	20
2.2.1 Preparation of gridded coverslips.....	20
2.2.2 Polylysine coating of coverslips.....	21
2.2.3 Preparation of cells for Laser-UVA-microirradiation.....	22
2.2.4 Laser-UVA-microirradiation with the P.A.L.M. microdissection system.....	23
2.2.5 Laser-UVA-microirradiation at an LSM 510 with UV-laser.....	24
2.2.6 Fixation and immunofluorescence staining of Rad51 and Mre11 after microirradiation.....	25
2.2.7 Immunofluorescence staining of BrdU.....	27
2.2.8 Antibodies used in this work.....	29
2.2.9 Staining of nuclear DNA with Propidium Iodide (PI).....	30
2.3 Microscopy	30
2.3.1 Transmitted light microscopy.....	30
2.3.2 Epifluorescence microscopy with widefield excitation.....	31
2.3.3 Laser-scanning microscopy.....	32

2.3.4	Measurement of the chromatic shift.....	34
2.3.5	Preparation of cells for live cell microscopy.....	35
2.3.6	Laser-photo-bleaching and live cell microscopy at the LSM 410.....	37
2.4	Evaluation.....	38
2.4.1	Software.....	38
2.4.2	The fourfold-point correlation.....	39
3	RESULTS.....	40
3.1	Localization and dynamics of DNA-repair proteins studied by laser-UVA-microirradiation.....	40
3.1.1	Setup of the microirradiation systems.....	40
3.1.1.1	The P.A.L.M. microdissection system.....	40
3.1.1.2	Adaption of a Zeiss LSM 510 for microirradiation.....	41
3.1.2	Rad51 accumulates at irradiated nuclear sites in human fibroblasts.....	44
3.1.3	Rad51 accumulation at irradiated sites is a specific reaction to DNA damage.....	49
3.1.4	Mre11 accumulates at laser-UVA-microirradiated nuclear sites and colocalizes with Rad51 accumulations.....	51
3.1.5	Accumulation of other DNA-repair related proteins after laser-UVA-microirradiation.....	55
3.1.6	The nuclear distribution of PML after microirradiation.....	56
3.1.7	The fraction of cells with focal Rad51 nuclear staining remains unchanged after microirradiation with 30 nJ.....	57
3.1.8	Chromosome territory arrangements during DSB repair.....	59
3.1.9	Localization of Rad51 in unirradiated nuclei.....	60
3.1.9.1	Endogenous Rad51 foci.....	60
3.1.9.2	GFP-Rad51 filaments.....	62
3.2	Chromosome territory dynamics studied in living cells by photobleaching of GFP-tagged chromatin (H2B-GFP).....	65
3.2.1	Setup of a 4D live cell imaging system at an LSM 410.....	65
3.2.2	Calibration of the detector response.....	67
3.2.3	Stability of CT arrangements in interphase nuclei visualized by stripes of photobleached H2B-GFP.....	70
3.2.4	Changes of CT arrangements in mitosis visualized by unbleached H2B-GFP tagged chromatin.....	72
3.2.5	Quantitative evaluation of changes in the radial distribution of unbleached chromatin in mitosis.....	78
3.2.6	Quantitative evaluation of the degree of clustering of unbleached chromatin by an autocorrelation method.....	81
4	DISCUSSION.....	87
4.1	Technical advances in laser-microirradiation.....	87
4.2	Localization and dynamics of DNA-repair proteins.....	91
4.2.1	Rad51-accumulation at irradiated sites and its relation to Mre11.....	91
4.2.2	Persistence of Rad51 S-Phase foci during repair.....	95

4.2.3 Post-irradiation arrangements of Rad51 accumulations are stably maintained	96
4.2.4 The relation of Rad51 to the Interchromatin compartment	96
4.3 Chromosome territory dynamics.....	98
4.3.1 CT dynamics in interphase nuclei.....	98
4.3.2 Changes of CT order from one cell cycle to the next.....	99
 LITERATURE.....	 103
 APPENDIX	 113
Abbreviations	113
Contents of the supplemental CD	114
 DANKSAGUNG	 115
 LEBENS LAUF	 117
 LIST OF PUBLICATIONS	 118

List of Figures

Figure 1.1: Schematic presentation of different DSB repair mechanisms	3
Figure 1.2: Chromosome arrangements in blastomere nuclei of <i>Parascaris equorum</i> ($2n = 2$) drawn by Theodor Boveri (Boveri 1909).....	8
Figure 1.3: Schematic lightpath of a beam scanning confocal microscope	11
Figure 2.1: Live primary human fibroblasts growing on a coverslip with a manually scratched grid	21
Figure 3.1: Scheme depicting a microirradiation beam hitting a fibroblast cell nucleus.	40
Figure 3.2: Measurements and extrapolation of the UV pulse energy of the P.A.L.M. laser	41
Figure 3.3: Scheme of Laser-UV-microirradiation with the “Bleach ROI” function.....	42
Figure 3.4: Rad51 immunostaining in non-irradiated GM02063 cells.	44
Figure 3.5: GM02063 cells after laser-UVA-microirradiation at a single nuclear site.....	45
Figure 3.6: GM02063 cells after laser-UVA-microirradiation at two nuclear sites.....	46
Figure 3.7: Dose dependence of Rad51 accumulation after microirradiation	47
Figure 3.8: Letter-like patterns irradiated in GM02063 cell nuclei.....	48
Figure 3.9: RNA-Pol II immunostaining of unirradiated GM02063 cells.....	49
Figure 3.10: Rad51 and RNA-Pol II immunostaining of microirradiated GM02063 cells	50
Figure 3.11: Rad51 and NC2 immunostaining of unirradiated and microirradiated GM02063 cells....	50
Figure 3.12: Rad51 and SC35 immunostaining of microirradiated GM02063 cells	51
Figure 3.13: γ -H2AX and Mre11 immunostaining of microirradiated primary human fibroblasts 2.5 to 5 min after irradiation	51
Figure 3.14: Rad51 and Mre11 immunostaining of microirradiated GM02063 cells fixed 30-40 min after irradiation	52
Figure 3.15: Bar plot of the fractions of GM02063 cell nuclei containing Rad51 accumulations and Mre11 accumulations after microirradiation.....	53
Figure 3.16: Bar plot of the fractions of primary fibroblast cell nuclei containing Rad51 accumulations and Mre11 accumulations after microirradiation	54
Figure 3.17: γ -H2AX and Ku70/80 immunostaining of microirradiated primary human fibroblasts 10 to 15 min after irradiation	55
Figure 3.18: Rad51 and RPA immunostaining of microirradiated GM02063 cells 30 min after irradiation	55
Figure 3.19: Localization of Rad51 and PML 8 and 24 hours after microirradiation	57
Figure 3.20: Bar plot of the fractions of GM02063 cell nuclei containing Rad51 accumulations and Rad51 foci after microirradiation.....	58
Figure 3.21: Bar plot of the fractions of primary fibroblast cell nuclei containing Rad51 accumulations and Rad51 foci after microirradiation.....	59
Figure 3.22: Stability of CT organization in interphase GM02063 cell nuclei during recombination repair of DSBs.....	60
Figure 3.23: Light-optical section of a GM02063 cell showing Rad51 (green) and nuclear DNA (PI, red).....	61
Figure 3.24: Light-optical section of a HeLa cell showing Rad51 foci (red) and nuclear DNA (H2B- GFP, green)	61
Figure 3.25: Light optical section of a GM02063 cell showing GFP-Rad51 filaments (green) and NLS-vimentin filaments (red).	62
Figure 3.26: GFP-Rad51 filaments (green) and PI (red) in a GM02063 cell.....	63
Figure 3.27: FRAP of nuclear GFP-Rad51 filaments.....	64
Figure 3.28: Light optical section of two GM02063 cell nuclei connected by GFP-Rad51 filaments two days after transfection of GFP-Rad51	64
Figure 3.29: Experimental setup (A) and scheme (B) of the live cell imaging system.....	65
Figure 3.30: Macro for live cell confocal microscopy at the LSM 410.....	66
Figure 3.31: Calibration of the photomultiplier PMT1 of the LSM 410: fit of the variance versus graylevel.....	68
Figure 3.32: Calibration of the photomultiplier PMT1 of the LSM 410: parameters for different contrast settings.....	69
Figure 3.33: Possible results of live cell observations of photobleached stripes in H2B-GFP labeled nuclei.....	70
Figure 3.34: Nuclear stripe photobleaching experiments indicate stability of large scale chromosome territory arrangements during interphase of HeLa cells.....	71
Figure 3.35: Large scale chromosome territory arrangements in HeLa cell nuclei change from one cell cycle to the next.	73

Figure 3.36: Daughter nuclei with clustered unbleached patches (pattern 1).....	74
Figure 3.37: Daughter nuclei with a cluster of unbleached patches and individual patches remote from the cluster (pattern 2)	75
Figure 3.38: Daughter nuclei with unbleached patches scattered over the nucleus.....	76
Figure 3.39: Signal of unbleached H2B-GFP-patches and nuclear counterstain of a pair of daughter nuclei of a partially bleached nucleus.....	77
Figure 3.40: GFP staining pattern of a completely bleached nucleus and its daughter nuclei	77
Figure 3.41: Segmentation of a nucleus for the quantification of the radial distribution of unbleached chromatin	79
Figure 3.42: Average radial distribution of the 10% highest intensity chromatin fraction in partially bleached and unbleached H2B-GFP HeLa cells.....	80
Figure 3.43: Average radial distribution of the 2% highest intensity chromatin fraction in partially bleached and unbleached H2B-GFP HeLa cells.....	81
Figure 3.44: Radial autocorrelation function (<i>RAC</i>) shown for simulations of typical distributions of unbleached chromatin.	83
Figure 3.45: Average <i>RAC</i> curves established from 24 mother cell nuclei before bleaching, after bleaching and before prophase, as well as for their 48 daughter cell nuclei.....	84
Figure 3.46: Average <i>RAC</i> curves established from the daughter nuclei classified by the degree of clustering of their unbleached chromatin patches	85

Summary

Modern light microscopical techniques were employed to follow dynamical nuclear processes during the cell cycle and during DNA-repair.

The role of Rad51 in DNA-repair

The protein Rad51 is essential for the repair of double-strand breaks (DSBs) via the conservative homologous recombination repair pathway (Shinohara *et al.* 1992; Shinohara *et al.* 1993; Baumann *et al.* 1996). In mammalian cells Rad51 is primarily located in the cell nucleus. In immunofluorescence micrographs Rad51 is concentrated in speckles dispersed over the nucleus called "Rad51 foci" in S-Phase cells and is dispersed in the nucleus in the other cell cycle stages (Tashiro *et al.* 1996; Scully *et al.* 1997a). In cells treated with ionizing radiation, nuclear Rad51 foci, are seen at high levels (Haaf *et al.* 1995; Scully *et al.* 1997a), and colocalize with sites of single-stranded DNA (Raderschall *et al.* 1999). This observation suggested that during the repair of a DSB Rad51 functions at the damaged site. Surprisingly, a previous study (Nelms *et al.* 1998) could not show the localization of Rad51 at damaged DNA in nuclei irradiated with ultrasoft X-rays structured by a striped mask.

Laser-UVA-microirradiation

To test the hypothesis that Rad51 localizes to damaged sites during DSB repair, a laser-UVA-microirradiation system was established based on a microdissection system coupled into a laser-scanning microscope (Zeiss LSM 410). With this system spots with sizes around 1 μm in nuclei of living cells can be irradiated with UVA-light (337 nm). After sensitization of cells by incorporation of BrdU into nuclear DNA and staining with the live cell dye Hoechst 33258 (Limoli and Ward 1993), the system can be used to introduce double-strand breaks and single-strand breaks in the irradiated spots. An improved microirradiation system was established at a laser-scanning microscope (Zeiss LSM 510) equipped with a UVA-laser.

The response of Rad51 to microirradiation

By use of laser-UVA microirradiation the localization of Rad51 at damaged sites containing DNA double-strand breaks could be demonstrated. The accumulation of Rad51 at microirradiated sites was followed in cells fixed at increasing times after microirradiation. First Rad51 accumulations were visible 5 - 10 minutes after irradiation, and the number of cells with Rad51 accumulations increased until a plateau was reached 20 - 30 minutes after irradiation. In contrast, the majority of irradiated cells had accumulations of Mre11 protein already 5 - 10 minutes after irradiation. This is consistent with reports that nuclear Mre11 foci appeared early in the response to ionizing radiation (Paull *et al.* 2000; Mirzoeva and Petrini 2001), but absolute response times were faster after microirradiation than after ionizing radiation. Possible reasons are discussed.

Large-scale nuclear patterns were microirradiated, and Rad51 accumulations that reflected the shape of the irradiated patterns were found up to eight hours after irradiation. This conservation of the pattern of Rad51 accumulations, which reflect sites containing the damaged DNA, indicated that the chromatin in the irradiated cells performs no large scale reordering in response to DNA damage.

The dynamics of chromosomes and chromosome territories

In 1909 Theodor Boveri forwarded the hypothesis that arrangements of chromosome territories (CTs) are stably maintained during interphase, but subject to changes during mitosis (Boveri 1909). In the last decade several groups reported

evidence for the stability of CT arrangements (Shelby *et al.* 1996; Abney *et al.* 1997; Zink *et al.* 1998; Bornfleth *et al.* 1999; Chubb *et al.* 2002; Lucas and Cervantes 2002), but considerable movements of chromosomal subregions were also observed (Martou and De Boni 2000; Cremer *et al.* 2003). The data concerning the maintenance or reordering of CTs during mitosis have been contradictory. Nagele *et al.* (1995) reported a precise spatial positioning of chromosomes in prometaphase chromosome rosettes from human cells. Other groups reported variable chromosome neighborhoods (Lesko *et al.* 1995; Allison and Nestor 1999; Cremer *et al.* 2001; Habermann *et al.* 2001).

Live cell imaging

To follow the movements of chromosomes and CTs, a novel experimental approach was taken. Cells expressing a fusion protein of the core histone H2B with GFP (H2B-GFP) stably incorporate H2B-GFP into nucleosomes (Kanda *et al.* 1998). In these cells chromatin regions were selectively marked by laser-photobleaching and followed by live cell microscopy. To this end, a live cell imaging system was established at a confocal laser-scanning microscope, which allows the observation of living cells for several days.

Chromatin movements visualized by photobleached H2B-GFP

To track possible movements in interphase cell nuclei, stripe patterns were bleached into nuclei at several stages of interphase. These patterns were retained for up to two hours, until they became invisible due to the replacement of bleached H2B-GFP by unbleached H2B-GFP, supporting the hypothesis that CT order is stably maintained during interphase.

Nuclei, in which all chromatin except for a contiguous zone at one nuclear pole was bleached, were followed through mitosis. The unbleached chromatin zone retained its location and shape until prophase further supporting the stability of CT order during interphase. At prophase a number of unbleached chromosomal segments became visible. The segments showed a variable degree of clustering in metaphase. When daughter nuclei were formed, the segments locally decondensed into patches of unbleached chromatin. In all daughter cells the patches were separated by bleached chromatin, and clustered to a variable extent. These observations support the hypothesis that changes of chromosome neighborhoods occur during mitosis and that CT neighborhoods can profoundly vary from one cell cycle to the next.

1 Introduction

1.1 DNA double-strand break repair

DNA damage can cause the alteration of genes with the possible consequence that important gene products can no longer be produced by the cell or are malfunctioning leading to uncontrolled growth or cell death. Hence cells have mechanisms to repair all possible forms of DNA damage (Friedberg *et al.* 1995; Schärer 2003). DNA double-strand breaks (DSBs) are a particularly dangerous type of damage, since at the site of a DSB there is no intact strand, by which the correctness of a repair can be checked, and repair of DSBs can cause chromosomal translocations (Jackson 2001).

There are two groups of DSB-repair mechanisms: homology-dependent mechanisms (homologous recombination repair, HRR) and homology-independent mechanisms (non-homologous end joining, NHEJ) (for reviews see Kanaar *et al.* 1998; Pfeiffer *et al.* 2000; Jackson 2001; Khanna and Jackson 2001; Symington 2002). HRR can be further subdivided into the conservative mechanism gene conversion and the non-conservative mechanism of single-strand annealing (SSA) (Figure 1.1).

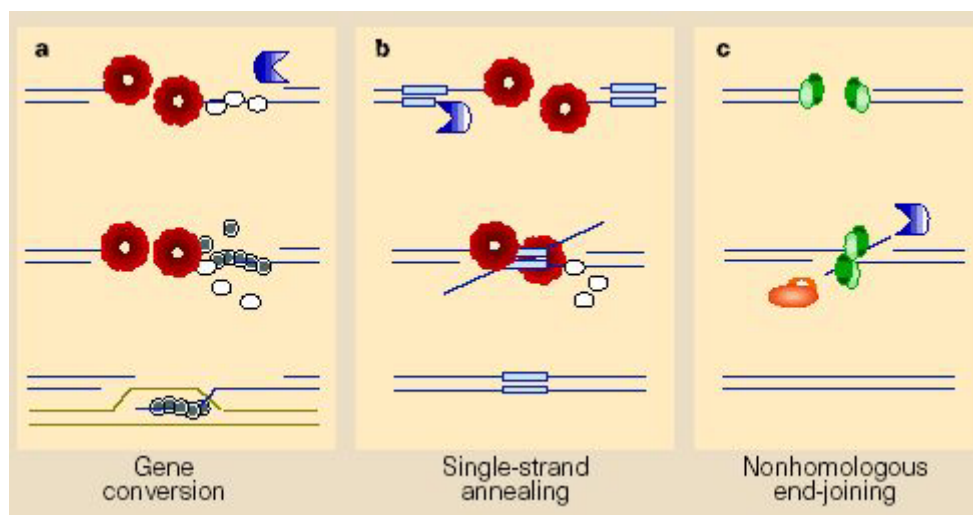


Figure 1.1: Schematic presentation of different DSB repair mechanisms

from (Haber 1999)

(a) Gene conversion: the broken ends are exonucleolytically resected, and an overhanging single-strand is paired with a homologous chromosome or sister chromatid. Proteins shown: Rad52 (red), the MRX/MRN complex (blue), RPA (white) and Rad51 (gray)

(b) Single-strand annealing: the broken ends are resected, until homologous regions are exposed on both sides of the break. Proteins: see (a)

(c) Non-homologous end joining: the broken ends are joined end to end, possibly involving pairing of microhomologies at the ends. Proteins shown: DNA-PK (green), the MRX/MRN complex (blue), DNA ligase IV and XRCC4 (orange).

In the case of gene conversion (Figure 1.1a) an overhanging 3'-ended strand of the broken chromatid is exchanged with an intact homologous strand. The exchanged intact strand serves as a template for the repair of the break. Due to the use of an intact template this pathway allows the accurate restoration of the DNA sequence at the broken site ("conservative" repair). Before strand exchange the broken ends are resected by a 5' to 3' exonuclease to produce a 3' overhang, which is used for homology search. Mre11, which forms a complex with Rad50 and Xrs2 (in

yeast, MRX) or Rad50 and NBS1 (in vertebrates, MRN), has been hypothesized but not proven to perform this resection (Symington 2002). The 3' overhang is initially stabilized by the single-strand binding protein RPA. Then Rad51 forms nucleoprotein filaments on ssDNA and promotes pairing of homologous strands and strand exchange (Shinohara *et al.* 1992; Shinohara *et al.* 1993; Baumann *et al.* 1996). Rad52 binds to and protects ssDNA ends, promotes end-to-end interaction (Van Dyck *et al.* 1998; Van Dyck *et al.* 1999) and mediates replacement of RPA by Rad51 on ssDNA strands (Song and Sung 2000; Sugiyama and Kowalczykowski 2002). In vertebrates the function of Rad52 can be substituted by the Rad51 paralog XRCC3 (Fujimori *et al.* 2001).

SSA (Figure 1.1b) takes place between two repeat sequences flanking a DSB. It does not require an intact template strand and causes the loss of one of the repeats and of the sequence between the repeats ("non-conservative" repair). SSA is initiated by 5' to 3' resection of the broken ends (possibly by Mre11), which exposes substantial (~400 bp) regions of homology. Subsequently, the exposed 3'-tails are annealed. Annealing is dependent on Rad52 (Pfeiffer *et al.* 2000).

Repair by NHEJ, also called "illegitimate recombination", results in the rejoining of broken ends without a requirement for homologous sequences, although microhomologies (1-10 bp) at broken ends can be used. If the two ends are compatible and no bases were lost from the ends, the repair is potentially accurate without causing a mutation, but the NHEJ pathway cannot recover lost sequences (Pfeiffer *et al.* 2000). NHEJ involves the Ku-proteins Ku70 and Ku80 (Featherstone and Jackson 1999), which form the Ku heterodimer. In vertebrates the Ku proteins form the DNA dependent protein kinase (DNA-PK) together with a third protein, the DNA-PK catalytic subunit (DNA-PKcs) (Smith and Jackson 1999). Ku can transiently bridge DSBs and stimulates the activity of DNA ligases (Ramsden and Gellert 1998). Other factors are the DNA ligase IV, its cofactor XRCC4 and the MRX/MRN complex. An error-prone Ku-independent NHEJ was detected in cells with non-functional Ku (Critchlow and Jackson 1998).

The three repair mechanisms are present in yeast and in vertebrate cells. However, as gene conversion was first discovered in yeast and NHEJ was first found in mammalian cells, it was initially believed that these repair mechanisms are exclusive to the respective cell types. Later, homologues of proteins involved in gene conversion were identified in vertebrate cells (Bezzubova *et al.* 1993; Morita *et al.* 1993; Shinohara *et al.* 1993) and NHEJ-proteins in yeast (reviewed in Critchlow and Jackson 1998). However, traces of NHEJ in yeast were only found in *rad52* mutant cells or in haploid G1 cells (Siede *et al.* 1996). In mammalian cells the expression of the *rad51* and *rad52* genes, involved in gene conversion, is induced in late G1 phase (Chen, F. *et al.* 1997). Furthermore, it was found that the primary target for gene conversion in mammalian cells is the sister chromatid of an already replicated chromosome (Johnson and Jasin 2000; Johnson and Jasin 2001). These findings led to the view that in yeast the major pathway for DSB repair is gene conversion with NHEJ as a backup pathway (Symington 2002), whereas in mammalian cells the gene conversion repair mechanism acts on broken chromatids in already replicated DNA, and SSA and NHEJ act on non-replicated DNA (Hendrickson 1997). However, the biochemical mechanism which chooses between the different pathways of DSB-repair is not known (Haber 1999; Pfeiffer *et al.* 2000).

1.1.1 Phosphorylation of H2AX marks broken chromatin

An early event at the site of a double-strand break is the phosphorylation of the H2A variant H2AX at serine 139 in megabase chromatin domains at broken DNA

ends (Rogakou *et al.* 1998; Rogakou *et al.* 1999). H2AX phosphorylation appears at sites of DSBs during DSB-repair, meiotic recombination, apoptotic digestion, V(D)J splicing and class switch recombination (for a review see Ausio and Abbott 2002), and therefore seems to be a universal cellular reaction to DSBs. The kinase responsible for phosphorylation is DNA-PK, ATM or ATR, possibly depending on the process, in whose course the phosphorylation happens (Redon *et al.* 2002). ATM is the major kinase phosphorylating H2AX during DSB-repair of lesions induced by γ -radiation (Andegeko *et al.* 2001; Burma *et al.* 2001). ATR phosphorylates H2AX in response to replicational stress (Ward and Chen 2001).

Recently, NBS1, which is a part of the vertebrate MRN complex, has been shown to directly bind to phosphorylated H2AX (γ -H2AX) through its FHA/BRCT domain (Kobayashi *et al.* 2002). As foci of NBS1, BRCA1, 53BP1 and MDC1 - all proteins containing BRCT domains - appear early after induction of DSBs, this interaction could provide a mechanism for targeting DSB-repair factors to a broken site (Schultz *et al.* 2000; Kobayashi *et al.* 2002; Goldberg *et al.* 2003). This view is supported by the finding that focus formation of several repair proteins in response to ionizing radiation is suppressed when the phosphorylation of H2AX is inhibited (Paull *et al.* 2000).

1.1.2 The Mre11-Rad50 complex

The Mre11-Rad50 complex is evolutionarily conserved. Its proteins are encoded in bacteriophages, archaea, eubacteria and eukaryotes (for reviews see Haber 1998; D'Amours and Jackson 2002). In yeast, the complex also contains Xrs2 (MRX-complex), in vertebrates NBS1 (MRN-complex). Although Xrs2 and NBS1 are considered "functional homologues", they show only weak sequence homology (D'Amours and Jackson 2002). The complex is implicated in NHEJ and HRR. It has DNA nuclease, helicase, annealing and ATPase activities. The particular function in DNA repair is unknown. MRN/MRX has been hypothesized to exonucleolytically resect broken ends prior to recombination/religation. However, two findings argue against this function. First, Mre11 exonuclease activity *in vitro* proceeds from the 3' to the 5' end, whereas during DSB repair broken DNA ends are resected in the 5' to 3' direction (Paull and Gellert 1998; Trujillo *et al.* 1998). Second, nuclease deficient mutants of Mre11 are still competent for repair of DNA DSBs (Bressan *et al.* 1999). Recently a structural role of MRX/MRN in DSB repair was proposed, in which the DNA-binding sites of Mre11 hold the broken DNA ends together. In the case of gene conversion, a homologous chromatid could be trapped by the extended coiled-coil regions of Rad50 (Connelly and Leach 2002). Alternatively or additionally, MRX/MRN could function in checkpoint signaling (D'Amours and Jackson 2002).

Mre11 immunofluorescence signal is homogenously distributed in nuclei of undamaged human cells and localizes to sites of DSBs selectively created by partial volume irradiation (Nelms *et al.* 1998). After detergent extraction of unbound nuclear Mre11, foci of Mre11 become visible in undamaged nuclei, which colocalize with PML bodies (Mirzoeva and Petrini 2001). 20 min to 8 h after treatment with 12 Gray of ionizing radiation, a more punctate pattern of small Mre11 foci distinct from PML bodies is seen. 4 h to 24 h after irradiation, a fraction of the irradiated nuclei exhibit a pattern of large, irregularly shaped Mre11 foci (Maser *et al.* 1997; Mirzoeva and Petrini 2001). Mre11 signals after ionizing radiation were reported to be distinct from Rad51 signals (Nelms *et al.* 1998; Mirzoeva and Petrini 2001).

1.1.3 Rad51

The Rad51 protein is the eukaryotic homolog of the bacterial RecA recombination protein. It is highly conserved from yeast to human and plays a central role in homologous recombination repair by gene conversion and in meiotic recombination (Shinohara *et al.* 1992). Rad51 forms helical filaments on both single-stranded DNA (ssDNA) and double-stranded DNA, promoting homologous pairing and strand exchange (Shinohara *et al.* 1992; Shinohara *et al.* 1993; Baumann *et al.* 1996). Human Rad51 protein interacts with Rad52, replication protein A (RPA), and the tumor suppressors p53, Brca1 and Brca2 (Shen *et al.* 1996; Buchhop *et al.* 1997; Scully *et al.* 1997b; Wong *et al.* 1997; Golub *et al.* 1998). In yeast, lilies, mice, and humans, Rad51 forms nuclear protein complexes on meiotic chromosomes (Bishop 1994; Haaf *et al.* 1995; Terasawa *et al.* 1995; Scully *et al.* 1997b).

Rad51 transcription in mammalian cells is induced in late G1 phase (Tashiro *et al.* 1996; Yamamoto *et al.* 1996), but the Rad51 protein is also detectable in quiescent and G1 cells (Chen, F. *et al.* 1997; Bischof *et al.* 2001). Human Rad51 protein shows discrete foci in nuclei of somatic cells typically during S phase (Tashiro *et al.* 1996; Scully *et al.* 1997b). Notably, a fraction of the S phase Rad51 foci colocalize with Brca1 foci and Brca2 foci (Scully *et al.* 1997b; Chen, J. J. *et al.* 1999).

60 minutes after treatment with agents inducing double-strand breaks, Rad51 focus formation is enhanced (Haaf *et al.* 1995; Raderschall *et al.* 1999). Damage induced Rad51 foci are formed at sites of ssDNA (Raderschall *et al.* 1999). 24 h after irradiation with 10 Gy, Rad51 together with RPA but not Rad52 is sequestered into micronuclei (Haaf *et al.* 1999). Several lines of evidence suggest that Rad51 foci correspond with nuclear protein complexes for recombinational DNA repair (Scully *et al.* 1997a; Raderschall *et al.* 1999; Paull *et al.* 2000), and the work presented here added evidence to this (Tashiro *et al.* 2000). Damage-induced Rad51 foci colocalize with RPA (Golub *et al.* 1998), Rad52 (Liu and Maizels 2000), Brca1 (Paull *et al.* 2000), PCNA (Scully *et al.* 1997a), and BLM (Bischof *et al.* 2001).

1.2 Laser-UV-microirradiation

Local irradiation of cells with a focused UV-microbeam is a well established tool in experimental cell research and radiation biology (Tschachotin 1912; Cremer *et al.* 1974; Berns 1978). As compared to whole cell irradiation, microirradiation approaches provide the great advantage that pre-selected cellular sites can be manipulated. In particular, excision repair of thymidine dimers was studied in microirradiated interphase nuclei of mammalian cells (Cremer *et al.* 1981a). UV-microirradiation as a tool in radiation biology has the drawback that it cannot be used per se to produce DSBs. Microirradiation with ultrasoft X-rays (Nelms *et al.* 1998) or focused ion beams (Brenner 2000) has been used for the local nuclear induction of DSBs, but requires sophisticated and costly equipment. Limoli & Ward (1993), however, have demonstrated that UVA exposure produces single-strand breaks, as well as DSBs, after a sensitising treatment of the nuclear DNA by the incorporation of the thymidine analogue BrdU and staining with the DNA dye Hoechst 33258. Recently, this approach was combined with laser-UVA-microirradiation to study the phosphorylation of H2AX at sites of DSBs (Rogakou *et al.* 1999) and the recruitment of DNA-repair proteins to such sites (Paull *et al.* 2000).

1.3 Nuclear architecture and dynamics

The cell nucleus is a compartmentalized organelle. Apart from chromatin, which is organized in distinct chromosome territories (Cremer *et al.* 1981a; Manuelidis

1985; Cremer *et al.* 1993), it contains several substructures consisting of RNA and proteins, which are located in the interchromatin compartment (IC, Cremer and Cremer 2001). Among these substructures the nucleoli are the most prominent (Carmo-Fonseca *et al.* 2000). They are formed around the nucleolar organizing regions, which are clusters of ribosomal genes, and in human cells are located on chromosomes 13, 14, 15, 21 and 22. In the nucleoli, rRNA is transcribed and processed. Recently, they have been implicated in cell-cycle regulation (Carmo-Fonseca *et al.* 2000). Splicing factor compartments (SFCs), also called “speckles”, contain a high concentration of pre-mRNA splicing factors and are believed to be storage or assembly sites of spliceosomal components (Misteli 2000). Replication factories assemble and disassemble during S-phase in a coordinated, but asynchronous manner (Leonhardt *et al.* 2000). Other nuclear substructures are the coiled bodies or Cajal bodies (Gall 2000) and the PML bodies (Maul *et al.* 2000).

1.3.1 The arrangement of chromosome territories in interphase cell nuclei

Chromosome order during cell cycle and cell differentiation has become a focus of research to analyze the nuclear architecture and its functional implications (for reviews see Lamond and Earnshaw 1998; Cremer *et al.* 2000; Leitch 2000; Cremer and Cremer 2001; Parada and Misteli 2002). Early attempts to study higher order interphase chromosome arrangements were undertaken in the 19th century. In his work “Über Zelltheilung” (Rabl 1885), published in 1885, Carl Rabl not only argued for the first time that cells have a constant number of chromosomes, but also that chromosomes maintain their structure and nuclear position during interphase. Further indirect evidence for the hypothesis of stable arrangement of chromosome territories (CTs) during interphase was published by Theodor Boveri (Boveri 1909). Boveri observed that the ends of chromosomes in blastomere nuclei of the nematode *Ascaris megalocephala* (now *Parascaris equorum*) were marked by characteristic evaginations in the nuclear envelope. These evaginations showed the same spatial distribution in sister nuclei both at the beginning of the “silent stage” (G1) and in the following prophase. In subsequent cell cycles, however, the spatial pattern of these evaginations could change distinctly (see Figure 1.2).

From these observations Boveri developed the following hypothesis (Boveri 1909):

1. Chromosomes occupy distinct chromosome territories (CTs) in the cell nucleus.
2. CT order is stably maintained during interphase.
3. Changes of chromosome neighborhoods occur during mitosis, in particular during prometaphase, when chromosomes become attached to the spindle and move towards the metaphase plate. Accordingly, chromosome order in the metaphase plate and hence CT order during interphase can profoundly vary from one cell cycle to the next.
4. Chromosomal neighborhoods established in the metaphase plate are maintained during anaphase and telophase in the two separated sets of chromatids. This results in a rather symmetrical CT arrangement in the two daughter nuclei.

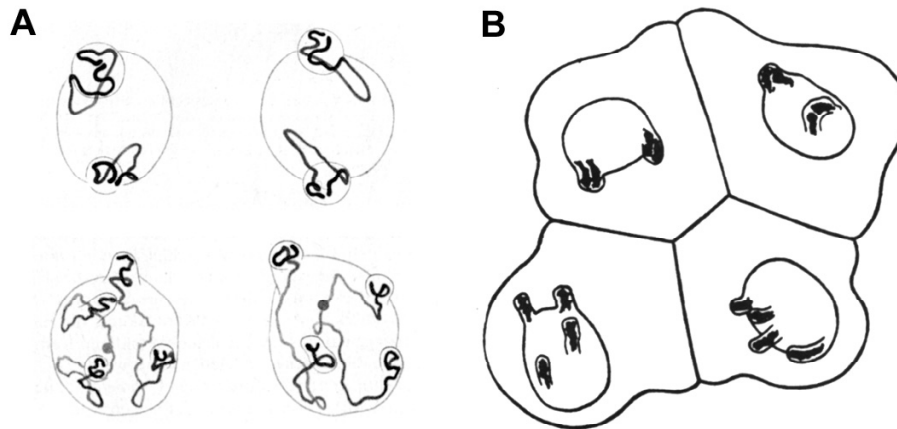


Figure 1.2: Chromosome arrangements in blastomere nuclei of *Parascaris equorum* ($2n = 2$) drawn by Theodor Boveri (Boveri 1909).

(A) The two nuclei above and below each represent a pair of daughter nuclei from blastomeres studied at prophase of the two-cell stage. Chromosome ends are fixed within evaginations of the nuclear envelope. Note that chromosome arrangements and the positions of the evaginations are similar in each pair, while different pairs show striking differences. (B) Interphase blastomere cells from an embryo drawn at the four-cell stage. Chromosome arrangements within the nucleus are invisible except for nuclear evaginations that indicate telomere positions. Each pair of daughter nuclei shows symmetrical positions of the evaginations, while a comparison of the two pairs reveals gross differences.

During the last decade numerous studies provided conclusive evidence for Boveri's first assumption in various animal and plant species. The chromatin masses of individual interphase chromosomes are arranged within distinct territories (Cremer *et al.* 1993; Leitch 2000; Cremer and Cremer 2001).

In support of Boveri's second assumption several reports described a high degree of stability of interphase chromosome arrangements in mammalian cell nuclei. *In vivo* microscopy showed a relative immobility of centromeres marked by the centromere binding protein CENP-B tagged with green fluorescent protein (GFP) except for some diffusive movements and occasional directed movements (Shelby *et al.* 1996). Lac Operon sequences integrated into chromosomal sites and visualized by a GFP-lac repressor fusion protein were on average constrained to 0.5 or 0.3 μm depending on the site of integration (Chubb *et al.* 2002). Subchromosomal foci replication labeled *in vivo* by incorporation of fluorochrome coupled thymidine analogs showed little movement (Zink *et al.* 1998; Bornfleth *et al.* 1999; Manders *et al.* 1999). In fluorescence recovery after photobleaching (FRAP) experiments submicrometer-sized spots bleached into fluorescently labeled chromatin persisted for more than one hour (Abney *et al.* 1997). Finally, the number of spatially separated CTs or CT-fragments visualized by a fluorescence *in situ* hybridization- (FISH-) probe for chromosome #18 in γ -irradiated and PHA-stimulated human peripheral blood lymphocytes increased 48 h after irradiation indicating that a mitosis was necessary to separate two fragments of a chromosome split by an unrepaired double-strand break (DSB) (Lucas and Cervantes 2002).

In contrast, more rapid movements of chromatin were reported for nuclei of budding yeast and *Drosophila* than for mammalian cells (for reviews see Gasser 2002; Marshall 2002). Furthermore, a dramatic nuclear reorganization in cell nuclei of *Drosophila* in the 14th cell cycle of embryonic development was reported (Hiraoka *et al.* 1993). Oppositely imprinted homologous chromosomal domains of the Prader-Willi syndrome/Angelman syndrome region in human T-lymphocytes approach in late S-Phase (LaSalle and Lalande 1996). The major histocompatibility complex (MHC)

region in human fibroblasts looped out from chromosome 6 upon transcriptional upregulation of the MHC region with IFN- γ (Volpi *et al.* 2000), and on transition from G1 to G2 centromeres in human T-lymphocytes were observed to move from a peripheral to a more interior location (Ferguson and Ward 1992). In conflict with Lucas and Cervantes (2002) a significant increase of chromosome 4 signals detected by FISH was noted in primary human fibroblasts and human peripheral blood lymphocytes within 1 h after irradiation with X-rays (Figgitt and Savage 1999).

Boveri's third assumption was challenged by Nagele *et al.* (1995) who noted a highly reproducible pattern of chromosome arrangements in prometaphase chromosome rosettes from human fibroblasts and HeLa cells and suggested permanent associations among adjacent chromosomes due to hypothetical centromere interconnections. Such connections could also provide a mechanism for ordered arrangements of CTs during interphase (Koss 1998; Nagele *et al.* 1999). Other groups did not observe highly reproducible neighborhoods of mitotic chromosomes or CTs (Lesko *et al.* 1995; Allison and Nestor 1999; Cremer *et al.* 2001; Habermann *et al.* 2001; Bolzer 2002). Several studies provided evidence for a non-random radial position of specific CTs in the nuclear interior or periphery (Skalnikova *et al.* 2000; Sun *et al.* 2000; Boyle *et al.* 2001; Cremer *et al.* 2001). Notably, such a radial order is fully compatible with a highly variable neighborhood of chromosomes (Cornforth *et al.* 2002).

For Boveri's fourth assumption anecdotal evidence has been reported, but a quantitative, high-resolution analysis has not yet been provided. Early studies indicated rather symmetrical locations of nucleoli as well as chromocenters in daughter nuclei from a variety of plant species (Heitz 1931). FISH-experiments suggested a considerable degree of symmetry in the arrangement of centromeres and whole CTs in daughter nuclei (Sun and Yokota 1999; Habermann *et al.* 2001).

1.3.2 The dynamics of nuclear proteins

Recently, knowledge about the dynamics of nuclear proteins has been boosted by experiments employing photobleaching of GFP-tagged proteins in living cells. The protocol mainly used in these experiments involves bleaching of GFP with a high laser power in a confined region and subsequently monitoring the recovery of GFP-fluorescence in this region (fluorescence recovery after photobleaching, FRAP Axelrod *et al.* 1976; White and Stelzer 1999; Reits and Neefjes 2001). As the photobleaching of GFP in a cellular environment is irreversible (Patterson *et al.* 1997; Swaminathan *et al.* 1997), fluorescence recovery is due to the movement of unbleached GFP-tagged proteins into the bleached region. Hence a FRAP experiment provides information about the mobility of the GFP-tagged protein under observation. In another type of experiment, fluorescence loss in photobleaching (FLIP Cole *et al.* 1996; White and Stelzer 1999), a region is repetitively bleached, and the fluorescence in regions outside the bleached region is monitored, yielding information about transport of proteins between different regions.

In contrast to chromatin, which is relatively immobile, many nuclear proteins have a high mobility (see Dundr and Misteli 2001). Even proteins which are part of apparently stable nuclear compartments can have high mobilities indicated by a short recovery time after photobleaching. This observation argues for a model, in which a protein molecule transiently binds to a compartment and after it is released is replaced by another protein molecule (Misteli 2001). Notably, nuclear proteins can become strongly constrained depending on their function (Houtsmuller *et al.* 1999; Essers *et al.* 2002; Sporbert *et al.* 2002).

A comparison of the measured recovery times may illustrate the different motilities of nuclear chromatin and proteins. Note, that the measured recovery time in a particular experimental setup does not only depend on the motility of the protein (i.e. its diffusion constant) but also on the geometry of the bleached area. However, as the diffusion constant has not been calculated in all cases, the recovery time may illustrate the order of magnitude of the diffusion constant, here. Abney *et al.* (1997) stained the nuclear DNA of Swiss 3T3 and HeLa cells with dihydroethidium, and bleached $\sim 0.4 \mu\text{m}$ sized spots into this counterstain. The spots persisted for more than an hour showing that DNA is immobile over distance scales of $0.4 \mu\text{m}$. Motility-measurements of the core histones confirmed this result and support a stable binding of H3 and H4 to nucleosomes, while $\sim 40\%$ of H2B exchanges with a half-time of 130 min (Kimura and Cook 2001). The linker histone H1 has a significantly shorter recovery time of only 200-250 s (Lever *et al.* 2000; Misteli *et al.* 2000), although there is a less mobile fraction of 10% in euchromatin and 25% in heterochromatin (Misteli *et al.* 2000). DNA-repair enzymes involved in nucleotide excision repair and homologous recombination repair freely diffuse in the nucleus (recovery time ~ 2 s), and after induction of DNA damage bind to damaged sites stably or transiently depending on their function in the repair process (Houtsmuller *et al.* 1999; Essers *et al.* 2002). A similar change from free diffusion of nucleoplasmic protein to more or less stable binding depending on active function has been found for proteins involved in DNA replication (Sporbert *et al.* 2002). High mobilities and fluorescence recovery within seconds have also been shown for transcription factors (McNally *et al.* 2000; Stenoien *et al.* 2001), pre-mRNA splicing factors (Kruhlak *et al.* 2000; Phair and Misteli 2000) and rRNA processing enzymes (Phair and Misteli 2000; Snaar *et al.* 2000). Finally, the recovery time of free GFP in cell nuclei is below 1 s (Essers *et al.* 2002).

1.4 Confocal microscopy

In contrast to a conventional epifluorescence microscope, which forms a blurred image including a wide range above and below the focus plane, the confocal microscope image contains information from only a small range around the plane of focus. Light emerging from above or below the plane of focus is excluded by means of a pinhole (Minski 1957; Cremer and Cremer 1978; Brakenhoff *et al.* 1979; Pawley 1995b). Information about the three dimensional distribution of dye concentration (fluorescence intensity) in a specimen can be collected by taking a series of images ("lightoptical sections") at different axial positions, a so-called "image stack". In this stack the images are separated from each other in axial direction by the "axial stepwidth" (or "z-stepwidth"). This procedure yields a three dimensional array of data elements ("voxels") for image analysis.

The principle of image formation of the confocal microscope is inherently different from that of a widefield microscope, which forms a real optical image in the camera or in the eye. In a confocal microscope (Figure 1.3) the object is scanned sequentially with a laser focus point by point and the fluorescence signal emitted by each point is recorded by a sensor, which is in most systems a photomultiplier tube (PMT). The image is then assembled from the recorded fluorescence intensities that are stored in computer memory. The laser excites fluorochrome molecules in a conical region throughout the specimen. All molecules in this region emit fluorescence light and would in principle contribute to the recorded signal. However, emission light from molecules outside the laser focus is excluded by the pinhole positioned in front of the detector. This pinhole is confocal to the laser focus (hence the term "confocal" microscope), i.e. light that is emitted from molecules in the laser

focus is focused onto the pinhole by the optics of the microscope. Light emitted from molecules outside the laser focus does not hit the pinhole or hits it defocused, so that its contribution to the recorded signal is strongly reduced (“optical sectioning”).

Scanning of the specimen can be performed in two different ways. In stage scanning the specimen is moved and the laser focus stays fixed. In beam scanning the specimen position is fixed and the laser focus is moved by means of galvanometer driven mirrors in the lightpath, as used in our laboratory. Most modern microscopes use beam scanning as it allows for faster scanning. However it goes along with optical aberrations, which result from moving the laser focus away from the optical axis. There are several variants of the beam scanning technique, e.g. the use of acousto-optical beam deflectors for scanning (Tsien and Bacsikai 1995) or the use of a rotating disc for scanning multiple beams over the specimen, simultaneously (Kino 1995).

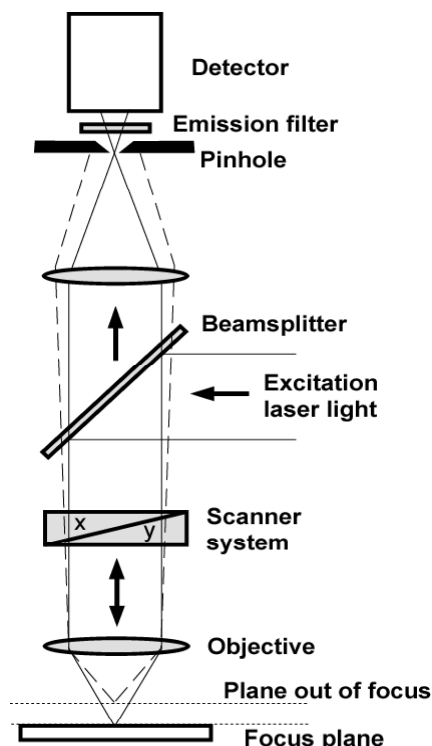


Figure 1.3: Schematic lightpath of a beam scanning confocal microscope taken from (Solovei *et al.* 2002).

The need for scanning the specimen imposes particular constraints on confocal microscopes. Take as an example a single light optical section with 512×512 pixels that is recorded in one second. This leaves for each pixel a maximum dwell time of $3.8 \mu\text{s}$, i.e. the time for which the laser beam illuminates a given point of the specimen. In practice delay times in the instrument make the dwell time even shorter. Thus all photons that contribute to each pixel have to be collected within microseconds. For obtaining a reasonable fluorescence signal one has to use high excitation intensities of the order of 1 MW/m^2 and more in a diffraction-limited spot. Such highly intense well focused monochromatic light currently can only be delivered by lasers, which makes the instrument expensive and limits, if only for funding reasons, the number of available excitation wavelengths. Even with such a high intensity of the excitation light the signal in the pixels of highest intensity rarely will consist of more than 1000 photons (Pawley 1995a) yielding a signal to noise ratio (S/N ratio) of 30. In widefield microscopy every pixel of the CCD camera collects light for the whole exposure time, thus requiring much lower excitation light levels, which

can be delivered by mercury arc or xenon arc lamps. Still during image capture one CCD pixel easily collects 10000 and more photons, yielding an S/N ratio of 100 and more.

Lately there has been a growing interest in 2-photon microscopy (Denk *et al.* 1995). This technique uses the fact that 2-photon fluorochrome excitation requires high light intensities, which are only obtained in the focal region, thus achieving an inherent optical sectioning effect even without a detection pinhole and reducing photobleaching outside the plane of focus. These properties make it specifically useful for thick specimens. Whether 2-photon microscopy also has advantages for thin specimens (in the range of 10 μm) is still being discussed (Patterson and Piston 2000).

Three-dimensionally resolved data can also be gained from a series of focal planes recorded by conventional epifluorescence microscopy throughout the specimen. As the epifluorescence microscope has no optical sectioning capability, in these images blurred signal from structures outside the focal plane adds to signal from within the focal plane leading to a low resolution in axial direction. This blurred signal can be removed by methods known as deconvolution (Shaw 1995). Setups for deconvolution microscopy are usually less expensive than confocal microscopes, and the method has advantages for multicolour FISH where a set of fluorochromes requires a wide range of excitation wavelengths for image acquisition or in cases where short recording times are necessary, e.g. in living cell observations. However, deconvolution can give rise to particular artifacts, which have to be recognized by the user (McNally *et al.* 1999). Deconvolution can also be done on confocal image stacks to further increase the resolution twofold and more.

1.5 Questions addressed in this work

Methodological work on laser-UVA-microirradiation

Studies employing laser-UV-microirradiation to date either used a system solely dedicated to that purpose (Zorn *et al.* 1976) or a commercial system for laser-microdissection (Rogakou *et al.* 1999). This constraint limited the application of laser-UV-microirradiation to specially equipped laboratories. Furthermore, the software used in laser-microdissection systems is designed for microdissection, but does not allow the storage and later retrieval of subnuclear irradiation positions or the start of fluorescence imaging immediately after microirradiation.

The initial goal of this work was to establish microirradiation at a microdissection system integrated into a laser-scanning microscope (Zeiss LSM 410). This system allows the microirradiation of living cells and the subsequent imaging with confocal microscopy.

Later, a laser-UVA-microdissection system could be established at a laser-scanning microscope (LSM 510 at the University of Hiroshima), which is equipped with a UV laser (Ar^+ -laser, 364 nm). This system allows the selection of irradiation positions in a fluorescence or transmission image, the later retrieval of the positions, and the start of confocal fluorescence imaging immediately after irradiation (Walter *et al.* 2003a).

Nuclear localization of Rad51 relative to DNA damage and Rad51 dynamics

Previous work suggested that Rad51 foci correspond with nuclear protein complexes for recombinational DNA repair (Scully *et al.* 1997a; Raderschall *et al.* 1999), but the colocalization of Rad51 with sites of DNA damage had not been conclusively demonstrated. Furthermore, a study based on partial exposure of nuclei to soft X-rays showed that Mre11 is assembled directly at sites of radiation-induced

DNA damage, but did not find Rad51-accumulation at these sites (Nelms *et al.* 1998). Using the laser-UVA-microirradiation method it was shown that Rad51 accumulates at damaged nuclear sites.

To clarify, whether Rad51 accumulating at damaged sites is redistributed from S-Phase Rad51 foci, the fraction of irradiated cells containing Rad51 foci, Rad51 accumulations or both was determined.

Using combined immunostaining of microirradiated cells with antibodies against Rad51 and several proteins not implicated in DNA-repair it was tested, whether Rad51 accumulation is a specific reaction to DNA damage.

Paull *et al.* (2000) indirectly showed that the formation of damage-induced Rad51-foci happens on a longer time scale than the assembly of foci containing the MRN-complex (visualized by Rad50 immunostaining). Here, the dynamics of Rad51 accumulation at irradiated sites was directly compared to that of Mre11 accumulation.

To follow possible movements of CTs in response to DNA-damage large-scale patterns in cell nuclei were microirradiated and traced by visualization of Rad51 accumulating in these patterns up to several hours after irradiation.

The localization of Rad51 in undamaged cell nuclei with respect to the interchromatin compartment (IC) was observed by high-resolution confocal imaging of endogenous Rad51 and overexpressed GFP-Rad51 in combination with chromatin.

Observation of chromosome territory dynamics by laser photobleaching

Using a HeLa cell line, which expresses GFP-tagged histone H2B (Kanda *et al.* 1998) the large-scale chromosome territory dynamics in interphase cells and metaphase cells was investigated. To follow the movement of chromatin in interphase, criss-cross stripes of photo-bleached chromatin were produced in nuclei at different stages of interphase. As H2B-GFP incorporated into nucleosomes exchanges slowly (Kimura and Cook 2001), chromatin sites are marked by the bleached H2B-GFP. The stripes were followed till fluorescence recovered.

To analyze possible changes of chromosome arrangements during mitosis, chromatin in mother cell nuclei was partially bleached during G2, and the unbleached chromatin was followed from mother nuclei to their daughter nuclei (Walter *et al.* 2003b).

2 Materials and Protocols

2.1 Cell culture

2.1.1 Cell types and culture media

Cell type	Culture Medium	Source	Reference
293-T (human kidney cancer)	DMEM	kindly provided by Dr. Satoshi Tashiro Hiroshima University, Hiroshima, Japan	
CHO (Chinese Hamster Ovary)	RPMI	kindly provided by Lutz Fröhnicke University Kaiserslautern	
SV-40 transformed human fibroblasts	DMEM	kindly provided by Dr. Eberhard Fritz, GSF Munich	(Xia <i>et al.</i> 1996)
primary human fibroblasts, XX	DMEM	kindly provided by Dr. Eishin Morita, Dept. Dermatology, Hiroshima University School of Medicine Hiroshima, Japan	
HCT-116 (human colon cancer cells)	Mc Coy's 5A Medium	kindly provided by Prof. Kyoshi Miyagawa, Institute for Radiation Research, Hiroshima University, Hiroshima, Japan	
HPHB125 (HCT-116 cells with RAD54B triple knockout; there are three RAD54B loci in HCT-116)	Mc Coy's 5A Medium	kindly provided by Prof. Kyoshi Miyagawa, Institute for Radiation Research, Hiroshima University, Hiroshima, Japan	(Miyagawa <i>et al.</i> 2002)
HeLa cells with stably incorporated histone H2B-GFP	RPMI / HEPES	kindly provided by Kevin Sullivan, The Scripps Research Institute, La Jolla, California, USA	(Kanda <i>et al.</i> 1998)

Cell culture media

Culture Medium	Supplier / Catalog Number	Solution used for cell culture
FCS (Fetal Calf Serum)	Biochrom, Berlin S 0115	in medium
Penicillin/streptomycin	Biochrom, Berlin A 2213	in medium
DMEM (Dulbecco's Modified Eagle Medium)	Biochrom, Berlin F 0435	500 ml DMEM 50 ml FCS 5 ml Penicillin/Streptomycin
Mc Coy's 5A Medium Modified	Gibco BRL, Tokyo, Japan 16600-082	500 ml Mc Coy's 5A 50 ml FCS 5 ml Penicillin/Streptomycin
RPMI 1640 with stable glutamine	Biochrom, Berlin FG1215	500 ml RPMI 50 ml FCS 5 ml Penicillin/Streptomycin
RPMI 1640 with 25 mM Hepes and stable glutamine	Biochrom, Berlin FG1385	500 ml RPMI / HPEPS 50 ml FCS 5 ml Penicillin/Streptomycin

2.1.2 Starting a cell culture from frozen cells**Materials**

Reagent / Material	Supplier / Catalog Number	Stock Solution	Final Concentration
Frozen cells in cryo-tubes			
Cell culture medium for the respective cell type	(see 2.1.1)		
PBS (Phosphate buffered saline, sterile)	ingredients from Sigma, Deisenhofen / Merck, Darmstadt	20x PBS: 160 g NaCl 4 g KCl 36 g Na ₂ HPO ₄ ·2H ₂ O 4.8 g KH ₂ PO ₄ in 1 l dH ₂ O pH adjusted to 7.4 with 1N HCl	1x PBS

Material / Equipment	Type	Supplier
tissue culture flasks	50 ml and 250 ml	Falcon / Schubert & Weiss, Munich
Plastic pipets for cell culture	Falcon 2 ml and 5 ml	Becton Dickinson, Schubert & Weiss, Munich
Pipet-aid	accu-jet® BRAND	Schubert & Weiss, Munich
Waterbath at 37°C		

Material / Equipment	Type	Supplier
Cell culture incubator	B 5060 operated at 37°C 5% CO ₂ atmosphere 100% humidity	Heraeus, Hanau
Sterile workbench	Antares 48	Biohit, Cologne
Cell culture phase contrast microscope	(see 2.3.1)	(see 2.3.1)

Protocol

1. Warm the cell culture medium to 37°C in the waterbath.
2. Prepare a 50 ml flask with 5 ml warm cell culture medium for each tube of cells to thaw.
3. Get the tube from the liquid nitrogen tank and thaw it in the 37°C waterbath.
4. When the content of tube is thawed, carefully transfer it into the 50 ml bottle.
5. Keep the cells in the cell culture incubator until they grow adherently (depending on the cell type, approx. 1 h, check in the cell culture microscope).
6. To remove the remaining DMSO, remove the cell culture medium, wash the cells with PBS and add fresh medium.

2.1.3 Subcultivation of adherently growing cells

Materials

Reagent	Supplier / Catalog Number	Stock Solution	Final Concentration
Cells growing in a 250 ml (75 cm ² bottom) culture flask			
Cell culture medium for the respective cell type	(see 2.1.1)		
PBS (sterile)	(see 2.1.2)		1x PBS
Trypsin / EDTA in PBS	Seromed Biochrom, Berlin L-2153	10x (0.5%)	1x (0.05%)

Material / Equipment	Type	Supplier
Plastic pipets for cell culture	Falcon 2 ml and 10 ml	Becton Dickinson / Schubert & Weiss, Munich
Pipet-aid	(see 2.1.2)	(see 2.1.2)
Waterbath at 37°C		
Cell culture incubator	(see 2.1.2)	(see 2.1.2)
Sterile workbench	(see 2.1.2)	(see 2.1.2)
Cell culture phase contrast microscope	(see 2.3.1)	(see 2.3.1)

Protocol

1. Warm all solutions to 37°C.
2. Dispose old medium from the cell culture flask.
3. Wash the cells with 10 ml PBS. Dispose PBS.
4. Fill 2 ml trypsin / EDTA into the cell culture flask. Make sure that the cells are covered by the solution.
5. Leave cells for 3 min in the incubator.
6. Check in the microscope that the cells detached from the flask (round appearance, floating). If not, detach by clapping the flask against your hand.
7. Resuspend the cells in 8 ml cell culture medium. (total volume: 10 ml)
8. Transfer an appropriate amount of the suspension to a new cell culture flask or remove all of the suspension up to that amount from the old flask.
9. Add 12 ml cell culture medium.
10. Store cells for further growth in the cell culture incubator.

2.1.4 Seeding cells to coverslips at a defined ratio

Materials as in 2.1.3. Additionally:

Reagent	Supplier / Catalog Number	Stock Solution	Final Concentration
Ethanol	Merck, Darmstadt		100%

Material / Equipment	Type	Supplier
Paper tissues	Kimwipes Lite, lint free	Kimberly & Clark / Schubert & Weiss, Munich
Petri dishes	50 mm, Falcon Easy Grip	Becton Dickinson / Schubert & Weiss
Coverslips	various sizes	Assistent / Schubert & Weiss, Munich or Matsunami glass ind., Ltd, Hiroshima, Japan
Fine forceps	INOX straight, No. 5	Dumont, neolab, Heidelberg
Sterile workbench	(see 2.1.2)	(see 2.1.2)
Gas burner	Gasprofi 1	WLD Tec, Göttingen

Protocol

1. Clean and sterilize the coverslips
 - Wipe coverslips clean with ethanol.
 - If coverslips are used later, store in ethanol.
 - Flame coverslips with gas burner.
2. Place coverslips into petri dishes.
3. Calculate, how much of a 10 ml cell suspension (see protocol 2.1.3 step 7) is needed for each coverslip using the formula:

$$V_{\text{petri dish}} = r_{\text{split}} \times 10\text{ml} \times \frac{A_{\text{petri dish}}}{A_{\text{bottle}}}, \text{ where } V_{\text{petri dish}}: \text{ volume of suspension to}$$

put in to petri dish, r_{split} : splitting ratio. $A_{petri\ dish}$: area of the petri dish (20 cm² for a 5 cm dish). A_{bottle} : area of the bottle (75 cm² for a 250 ml bottle).

4. Follow steps 1-7 in protocol 2.1.3, "Subcultivation of adherently growing cells". During step 5 fill cell culture medium into each petri dish, so that after splitting there will be 5 ml medium in the dish.
5. Transfer $V_{petri\ dish}$ of the 10 ml suspension into each petri dish (e.g. for splitting at a ratio $\frac{1}{4}$ from a 250 ml bottle to a 5 cm round petri dish, use 0.7 ml of the 10 ml suspension).
6. Store cells for further growth in the cell culture incubator.

2.1.5 Synchronization of HeLa cells with aphidicolin

Materials

Reagent	Supplier / Catalog Number	Stock Solution	Final Concentration
Aphidicolin	Sigma, Deisenhofen A 0781	10 mg/ml in DMSO	0.15 µg/ml
Cell culture medium RPMI / Heps	(see 2.1.1)		

Material / Equipment	Type	
HeLa cells	With stably incorporated H2B-GFP	(see 2.1.1)

Protocol

1. Block cells by adding 0.15 µg/ml aphidicolin to the growth medium. The concentration for effective blocking and release from the block depends on the cell type.
2. Wait at least 14 h.
3. Release cells from the block by washing three times with fresh medium. If the cells are seeded on a coverslip, lift the coverslip to ensure that medium below the coverslip is washed away.
4. Cells that were not in S-Phase at the time of step 1 should continue their cell cycle from early S-Phase, now.

2.1.6 Lipofection of GFP-Rad51 plasmid and NLS-vimentin with Pfx-1 or Fugene 6

Materials

Reagent	Supplier / Catalog Number	Stock Solution	Final Concentration
Pfx1	Invitrogen no longer sold	as provided	4 µl/ml
Fugene 6	Roche, Basel, Switzerland 1814443		1.5 µl/ml

Reagent	Supplier / Catalog Number	Stock Solution	Final Concentration
Optimem serum free medium	Gibco-BRL / Invitrogen		
GFP-Rad51 plasmid	kindly provided by Dr. Ryushin Mizuta Science University of Tokyo, Tokyo, Japan		with Pfx-1: 0.67 µg/ml with Fugene 6: 0.5 µg/ml
Xenopus NLS-vimentin plasmid	kindly provided by Peter Lichter, DKFZ Heidelberg (Bridger <i>et al.</i> 1998)		with Pfx-1: 0.67 µg/ml
PBS (sterile)	(see 2.1.2)		1x PBS

Material / Equipment	Type	Supplier
small Petri dishes	35 mm, Falcon Easy Grip	Becton Dickinson / Schubert & Weiss
Coverslips	various sizes	Assistent / Schubert & Weiss, Munich or Matsunami glass ind., Ltd, Hiroshima, Japan

Protocol

Transfection with Pfx-1:

1. Grow cells on coverslips in small petri dishes, so that they are ~50% confluent for transfection.
2. Mix 1 µg of the plasmid with 6 µl Pfx-1 and 1.5 ml serum-free medium according to the product instructions.
3. Remove growth medium from the cells and wash with PBS
4. Add the lipid mixture to the cells and incubate for 4 h.
5. Remove the lipid mixture, wash with PBS and add normal growth medium.
6. Incubate for 24 h and fix / perform live cell observation.

Transfection with Fugene 6:

1. Grow cells on coverslips in small petri dishes in 2 ml medium, so that they are ~50% confluent for transfection.
2. Fill 100 µl of serum-free medium into a tube.
3. Add 3 µl of Fugene 6. Undiluted Fugene 6 must not touch any plastic surface except pipet tips. Gently tap to mix.
4. Add 1 µg of plasmid. Gently tap to mix.
5. Incubate for at least 15 min at room temperature.
6. Dropwise add the mixture to the petri dish with cells.
7. Incubate for 24 h and use cells (transfection mixture does not have to be removed).

2.2 Laser-UVA-microirradiation

2.2.1 Preparation of gridded coverslips

Gridded coverslips are needed to relocate microirradiated cells on the coverslip after fixation and staining. They are commercially available from Eppendorf, Hamburg and Bellco Glass, Vineland, USA. When gridded coverslips of a special size and shape were needed, the grid had to be applied manually (compare Figure 2.1). The (tedious) protocol is described below. Use of commercial gridded coverslips is highly recommended.

Materials

Reagent	Supplier / Catalog Number	Stock Solution	Final Concentration
Ethanol	Merck, Darmstadt		100%

Material / Equipment	Type	Supplier
Coverslips	any	Assistent / Schubert & Weiss
Tungsten-carbide marker		neoLab, Heidelberg
Slide glass	76x26 mm	R. Langenbrink / Schubert & Weiss
Black Transparency Marker	Staedtler Lumocolor F or S	Feucht, Munich
Paper tissues	lint free	(see 2.1.4)
Cell culture phase contrast microscope	(see 2.3.1)	(see 2.3.1)

Protocol

1. Place a slide glass on the microscope stage. Place a coverslip on top.
2. Use the microscope in darkfield mode: Use the 5x Objective and the Ph2 phase ring.
3. Focus the top of the coverslip.
4. Scratch the grid: The lines become most regular when scratched vertical from top to bottom. For scratching horizontal lines, turn the coverslip by 90° and scratch vertical lines.
5. Make the grid asymmetrical, e.g. by putting an oblique line on top.
6. Test, whether a line has been scratched too deeply: hold the coverslip at the edges with two fingers and press it in the middle. If it breaks, don't feel sorry. It might have broken at the end of a long experiment.
7. Wipe the coverslips clean with ethanol.
8. With the black marker draw a pattern on the side opposite to the grid to mark the orientation of the grid.

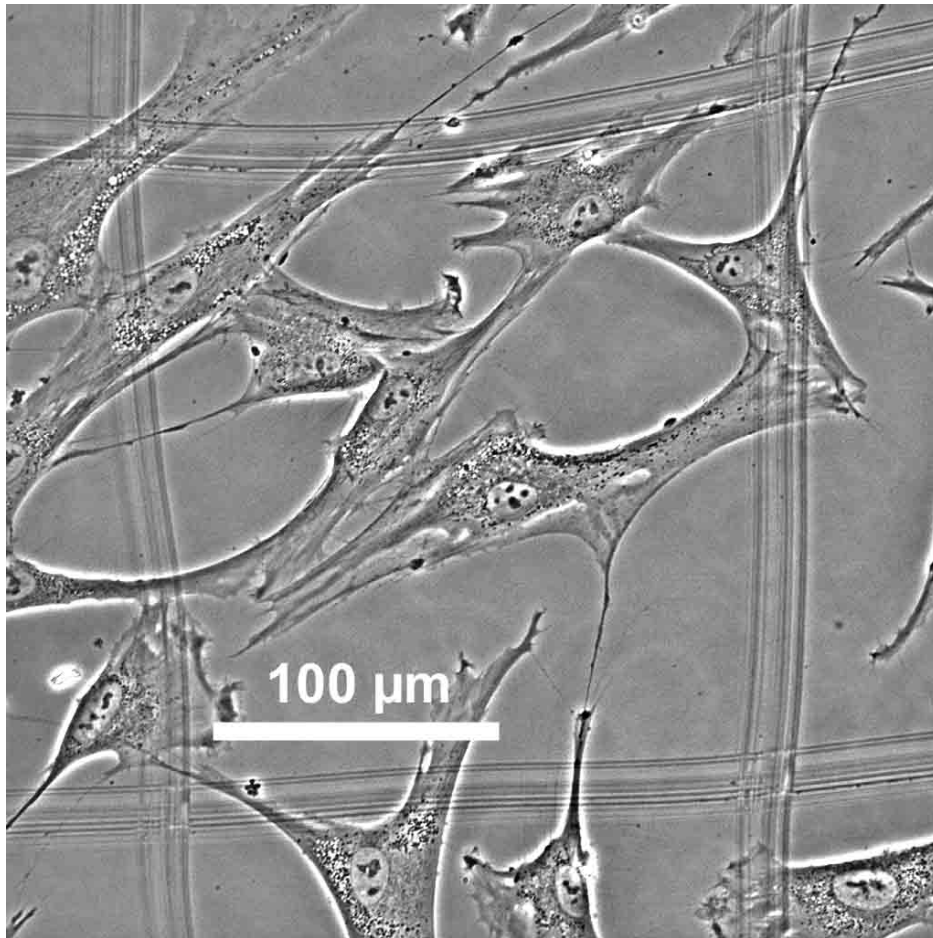


Figure 2.1: Live primary human fibroblasts growing on a coverslip with a manually scratched grid

One area of the grid is centered in the image, and the edges of the neighboring areas are visible.

2.2.2 Polylysine coating of coverslips

Coating coverslips with polylysine adds positive charges to the surface of coverslips and facilitates the adherence of cells to the coverslips. Polylysine can be used to keep floating cells adherent to coverslips when applied at 1 mg/ml (Solovei *et al.* 2002). In this work only adherent cells were used, and polylysine was generally not necessary. However with the coverslips used for the experiments in Hiroshima (Matsunami), cells regularly detached during washing and staining steps. Hence, polylysine coating (50 $\mu\text{g/ml}$) was used to prevent loss of cells.

Materials

Reagent	Supplier / Catalog Number	Stock Solution	Final Concentration
Poly-L-Lysine MW=150000-300000 D	Sigma, Deisenhofen P 1399	10 mg/ml in ddH ₂ O store at -20°C	50 $\mu\text{g/ml}$
ddH ₂ O			

Material / Equipment	Type	Supplier
Coverslips	any	
Petri dishes	50 mm, Falcon Easy Grip	(see 2.1.4)
Sterile workbench	(see 2.1.2)	(see 2.1.2)

Protocol

1. Dilute the stock solution 1:200 (to 50 µg/ml) in ddH₂O. For a round coverslip, 4 cm diameter make about 200 µl.
2. Put coverslips in petri dishes and pipet polylysine dilution on.
3. Wait 30 min.
4. Wash the remaining dilution off with ddH₂O.
5. Sterilize: flame the back of the coverslip and UV-irradiate the front.
6. Store in sterile petri dishes until seeding cells.

2.2.3 Preparation of cells for Laser-UVA-microirradiation

Laser-UVA-microirradiation was performed on cells sensitized to UVA light by replication labeling of chromosome DNA with BrdU alone (BrdU-UVA) or replication labeling with BrdU in combination with staining with the dye Hoechst 33258 (BrdU-Hoechst-UVA). The latter sensitization method, first published by Limoli and Ward (1993), leads to an induction of DNA single-strand breaks (SSBs) and double-strand breaks (DSBs) by UVA light at a ratio of approximately 100:1 (SSBs / DSBs).

Materials

Reagent	Supplier / Catalog Number	Stock Solution	Final Concentration
Cell culture medium for the respective cell type	(see 2.1.1)		
PBS (sterile)	(see 2.1.2)		1x PBS
BrdU	Sigma, Deisenhofen B 9285	0.3mM (MW = 307.1)	0.3µM
dThd	Sigma T 9250	2.5mM (MW = 242.2)	2.5µM
Hoechst 33258	Sigma B 2883	2µg/µl	2µg/ml

Material / Equipment	Type	Supplier
Cells		
Coverslips	round, diameter 40 mm for Bioptechs live cell chamber with grid (see 2.2.1) if necessary polylysine coated (see 2.2.2)	(see 2.1.4)
Petri dishes	Falcon Easy Grip 50 mm	(see 2.1.4)
Sterile workbench	(see 2.1.2)	(see 2.1.2)

Protocol

1. Seed cells to coverslips (ratio 1/5 for cell lines with doubling time ~20 h, see 2.1.4)
2. For irradiation with the BrdU-Hoechst system add 0.3 µM BrdU and 2.5 µM dThd (final concentration) to the growth medium of cells.
3. For irradiation with the BrdU system, add 10 µg/ml BrdU (final concentration) to the growth medium of cells.
4. Incubate cells for one cell cycle.
5. Wash off medium / BrdU with PBS.

6. Add fresh medium.
7. For irradiation with the BrdU-Hoechst system add 2 μ g/ml (final concentration) Hoechst 33258 and incubate for 10 min. Wash off the medium with PBS and add fresh medium. Cover the petri dishes with aluminum foil during and after incubation and protect from light.

2.2.4 Laser-UVA-microirradiation with the P.A.L.M. microdissection system

Materials

Material / Equipment	Type	Supplier
Cells prepared according to 2.2.3		
Calibration coverslip	even thickness 170 μ m covered with black marker mounted with spacers on a slide-glass	Coverslip: Assistent / Schubert & Weiss, Munich; Black Marker: Edding; Slide-glass: R. Langenbrink / Schubert & Weiss
Live cell microscopy chamber system	FCS2 living cell chamber / objective heater	Bioprotechs, Butler, USA
LSM 410 with Axiovert 100 stand and UV-laser microdissection system ($\lambda = 377$ nm)		Zeiss, Jena P.A.L.M., Bernried
Objective	Plan-Neofluar 63x/1.25 Ph3	Zeiss, Jena
Green bandpass filter	No. 467803	Zeiss, Jena

Protocol

1. Heat the objective to 37°C with the objective heater.
2. Calibrate the focus and the lateral position of the P.A.L.M. laser with respect to the phase contrast video-image seen in the P.A.L.M. software
 - Focus the calibration coverslip in the microscope and select an area, where the layer of black marker is thin.
 - Calibration of the laser-focus: starting from an energy setting of about 30 (~80 nJ/pulse in the back focal plane of the objective; ~8 nJ/pulse in the laser focus) ablate black marker with the laser. Turn the focus knob on the P.A.L.M. control until the point of ablated marker is small and sharp. If this is impossible, lower the laser energy and repeat.
 - Calibration of the lateral position: ablate black marker and set the marker for the focus point in the P.A.L.M. software to the position of the ablation spot.
 - The focus can also be defined with respect to the microscope eyepiece. Note that the image in the eyepiece and the image in the video camera usually are not focused at the same time.

3. Mount the coverslip with cells into the FCS2 chamber without the upper coverslip. The objective heater keeps the cells at 37°C.
4. View cells in phase contrast mode by visual / video observation. Use a filter to protect cells from UV-light emitted by the illuminating halogen lamp.
5. Irradiate cells. For positive control use one pulse with energy scale 60 (microdissection). For defined induction of DSBs and SSBs use not more than an energy setting of 30, corresponding to a pulse energy of 80 nJ before the objective or about 8 nJ in the laser focus.
6. Rad51 focus formation can be induced by 10 single pulses (~80 nJ) with BrdU-Hoechst sensitization or 120 pulses (4 s pulsing at the maximum pulse frequency of 30 Hz; 0.96 μ J) with BrdU sensitization.
7. Irradiate all cells in one field of the gridded coverslip with the same settings.
8. Fix and stain after an appropriate incubation time.

2.2.5 Laser-UVA-microirradiation at an LSM 510 with UV-laser

Materials

Material / Equipment	Type	Supplier
Cells prepared according to 2.2.3		
Calibration coverslip	even thickness 170 μ m, covered with black marker mounted with spacers on a slide-glass Mount the coverslip at low air-humidity. Otherwise laser ablation is not reproducible.	Coverslip and slide-glass: Matsunami glass ind., Ltd, Hiroshima, Japan Black marker: Makki, Zebra, Japan;
Live cell microscopy chamber system	FCS2 living cell chamber / objective heater	Bioptechs, Butler, USA
LSM 510 with UV-laser ($\lambda = 364$ nm)		Zeiss, Jena
Objective	Plan-Neofluar 40x/0.75, Ph 2	Zeiss, Jena
Green bandpass filter	No. 467803	Zeiss, Jena

Protocol

1. Start the microscope and the UV-laser. Load the database MI-settings.mdb. Open the one image in the database and press the "Reuse" button. This loads the standard settings for microirradiation.
2. Place a green filter into the beampath of the collimator for the halogen lamp. The filter suppresses UV-light when the cells are imaged in visual transmission.
3. Set the UV-laser tube current to 100%.
4. Image cells in phase contrast mode with the photomultiplier for transmission imaging.
5. Check the focus (collimator setting) of the UV-laser with respect to the phase contrast image.

- Focus the calibration coverslip in the microscope and select an area, where the layer of black marker is thin. Take an overview image.
 - Use the macro “CalColl”. The macro ablates the black marker with the UV-laser. It creates eleven columns of 3 ablation spots each, with the UV-collimator setting increasing from the left column to the right column in steps of one. The collimator setting of the middle column can be selected in the user interface.
 - Select a middle collimator setting of 17 and start the ablation. The correct collimator setting corresponds to the column where the ablation spot is clearest and sharpest. It is usually close to 17. A change of the collimator setting by three units corresponds to a focus shift of 1 μm .
6. Use the macro “SetColl” to set the UV-collimator to the value determined in the previous step.
 7. Check the lateral position of the UV-irradiation with respect to the phase contrast image.
 - Start the macro “Spotbleach”. This macro is also used for the irradiation of cells.
 - The starting values for constant and linear shift have been determined for the default irradiation setting (543 nm HeNe laser, image size: 1024x1024 pixels, pixel time 0.88 μs , zoom 0.7).
 - To check the settings, select several positions at all sides of the image and start laser ablation.
 - Take a phase contrast image. The ablated spots should appear in the image.
 - Using the cursor, check, if the position of the irradiated spots coincides with the selected positions.
 8. For irradiation mount the coverslip with cells into the FCS2 chamber. Connect the FCS2 temperature control to keep the cells at 37°C.
 9. Take an image of one field of the gridded coverslip. Select irradiation positions in all cells in this field.
 10. Start the irradiation. Rad51 focus formation can be induced e.g. with 82% UV-laser excitation and 10 irradiations per spot (~30 nJ).
 11. Save the image and the list of irradiation positions.
 12. Fix and stain after an appropriate incubation time.

2.2.6 Fixation and immunofluorescence staining of Rad51 and Mre11 after microirradiation

The immunofluorescence staining protocols for different proteins used in this work are generally similar, differing mostly in the type and concentration of the antibodies involved. As an example for the immunostainings performed in this work the protocol for the simultaneous staining of Rad51 and Mre11 after microirradiation is provided. The protocol differs from the “standard” in two ways: 1. The 4 cm round coverslips are cut before staining. 2. 0.1% SDS is added to the permeabilization solution, and the time for permeabilization is increased to 5 minutes to remove the background of unbound Mre11 protein from the nucleus.

Materials

Reagent	Supplier / Catalog Number	Stock Solution	Final Concentration
Formaldehyde prepared from paraformaldehyde powder	Merck cat. no.: 104005	powder	4%
PBS	(see 2.1.2)		1x PBS
BSA (Bovine serum albumin)		20% in PBS	1%
Triton-X-100		100%	0.5%
SDS (Sodium Dodecyl Sulfate)	Sigma L 4509	20% in PBS	0.1%
Rabbit- α -Rad51 antibody	Akira Shinohara (Tashiro <i>et al.</i> 1996)		1:1000
Mouse- α -Mre11 antibody	Genetex, San Antonio, USA MRE11-12D7	1 mg/ml	1:200
Goat- α -rabbit-FITC antibody	Tago / Biosource Solingen		1:1000
Sheep- α -mouse-Cy3 antibody	Jackson ImmunoResearch, West Grove, USA cat. no.: 515-165-062		1:200
Hoechst 33342 staining solution	Sigma B 2261		10 μ g/ml
VectaShield Antifade	Vector, Peterborough, UK		undiluted
Nailpolish	Sogo, Hiroshima, Japan		

Material / Equipment	Type	Supplier
Cells on 4 cm round coverslips		
Diamond glass cutter		e.g. neoLab, Heidelberg
Petri dishes	50 mm, Falcon Easy Grip	Becton Dickinson
Petri dish	20 cm diameter	Greiner
Slide glasses	76x26 mm	Matsunami glass ind., Ltd, Hiroshima, Japan
Quadri PERM® plus	for 4 slide glasses 76x26mm	Heraeus, Hanau
Parafilm TM		Merck, Darmstadt
Plastic box	opaque	neoLab, Heidelberg
Paper tissues	lint free	(see 2.1.4)
Fine forceps	(see 2.1.4)	(see 2.1.4)

Protocol

Fixation

1. Transfer the coverslip with cells to a petri dishes containing 4% Formaldehyde / PBS.
2. Incubate 10 minutes.
3. Discard the Formaldehyde solution and quickly replace by PBS.

Cutting of coverslips

1. Fill the lid of a 20 cm petri dish with PBS.
2. Transfer the coverslip with fixed cells to the lid with PBS.
3. Cut the coverslip down to an area of about 2x2.5 cm² by pressing the slide glass on the coverslip along the cutting lines and cutting with the diamond.
4. Cut off the upper right corner to make the coverslip asymmetrical.

Immunofluorescence staining

1. Wash coverslips 2x3 min in PBS.
2. Permeabilize in 0.5% Triton / 0.1% SDS for 5 min.
3. Wash 2x3 min in PBS.
4. In the meantime prepare the primary antibody solution (150-200 µl per coverslip):
 - 1% BSA in PBS
 - Rabbit- α -Rad51 1:1000
 - Mouse- α -Mre11 1:200
5. Spread a piece of parafilm on the bottom of the plastic box. Put a wet paper tissue into the box.
6. For each coverslip pipet the antibody solution onto the parafilm.
7. Carefully lower the coverslip onto the drop with the cell side down.
8. Incubate for 30 min at 37°C.
9. In the meantime prepare the secondary antibody solution (150-200 µl per coverslip):
 - 1% BSA in PBS
 - Goat- α -rabbit-FITC 1:1000
 - Sheep- α -mouse-Cy3 1:200
10. Wash 2x3 min in PBS.
11. Repeat steps 5-8 with the secondary antibody solution.
12. Wash 2x3 min in PBS.
13. Stain with Hoechst 33342 for 2 min.
14. Wash shortly in PBS.
15. Mount the coverslips on slide glasses with antifade medium.

2.2.7 Immunofluorescence staining of BrdU

For immunofluorescence staining of BrdU the bromine moiety of BrdU incorporated into DNA has to be made accessible for the antibody. The protocol described here achieves this by digestion with DNase I.

Materials

Reagent	Supplier / Catalog Number	Stock Solution	Final Concentration
PBS	(see 2.1.2)		1x PBS
BSA (Bovine serum albumin)		20% in PBS	1%

Reagent	Supplier / Catalog Number	Stock Solution	Final Concentration
Triton-X-100		100%	0.5%
SDS (Sodium Dodecyl Sulfate)	Sigma L 4509	20% in PBS	1%
“Solution 3” from Roche Kit	Roche or mixed from components	66mM Tris-Cl (pH 8) 0.66mM MgCl ₂ 1mM 2-mercaptoethanol	1:2
DNase I grade II	Roche (Boehringer Mannheim) 104159	1 mg (2000 U) in 0.5 ml glycerol and 0.5 ml 0.3 M NaCl in ddH ₂ O	10µg/ml ~ 2 U/ml
M-α-BrdU	Roche (Boehringer Mannheim) 1170376		1:200
S-α-M-Cy3	Jackson ImmunoResearch, West Grove, USA 515-165-062		1:200
Hoechst 33342 staining solution	Sigma B 2261		10 µg/ml
VectaShield Antifade	Vector, Peterborough, UK		undiluted

Protocol

1. Fix cells in 4% formaldehyde (see section 2.2.6).
2. Wash 2x3 min in PBS.
3. Permeabilize / denature with 1% SDS / 0.5% Triton-X-100 for 10 min.
4. Wash 2x3 min in PBS.
5. First antibody staining (30 min at 37°C):
 - 0.5% BSA / 0.5x PBS / 33 mM Tris-HCl / 0.66 mM MgCl₂ / 0.5 mM 2-mercaptoethanol (i.e. a 1:1 mixture of 1% BSA/PBS and “Solution 3”)
 - M-α-BrdU 1:200
 - DNase I 1:100 (2 U/ml)
6. Wash 2x3 min in PBS.
7. Second antibody staining (30 min at 37°C)
 - 1% BSA/PBS
 - S-α-M-Cy3 1:200
8. Wash 2x3 min in PBS
9. Stain with Hoechst 33342 for 2 min.
10. Wash shortly in PBS.
11. Mount the coverslips on slide glasses with antifade medium.

2.2.8 Antibodies used in this work

Primary antibodies

Antigen	Raised in	Detected with secondary antibody	Provider	Working dilution
BrdU	mouse	sheep- α -mouse-Cy3	Roche (Boehringer Mannheim) 1170376	1:200
γ -H2AX	rabbit	goat- α -rabbit-FITC	Dr. Junya Kobayashi, Dept. Radiation Biology, Hiroshima University, Hiroshima, Japan	1:200
human Ku70/80 heterodimer	mouse	sheep- α -mouse-Cy3	Pharmingen, San Diego, CA, USA	1:200
Mre11	mouse	sheep- α -mouse-Cy3	Genetex, San Antonio, USA MRE11-12D7	1:200
NC2	rat monoclonal	goat- α -rat-Rhodamine	Dr. Michael Meisterernst, Genzentrum, München	1:2
PML	mouse	sheep- α -mouse-Cy3	Santa Cruz, sc-966	1:200
Rad51	rabbit	standard detection: goat- α -rabbit-FITC if noted in results with: goat- α -rabbit-biotin and avidin-Cy5	Dr. Akira Shinohara, Dept. Radiation and Cellular Oncology, University of Chicago, Chicago, IL, USA (Tashiro <i>et al.</i> 1996)	1:1000
RNA-Pol II carboxyterminal domain	mouse	sheep- α -mouse-Cy3	Dr. Dirk Eick, GSF, München	1:50
RPA (p70 subunit)	mouse	sheep- α -mouse-Cy3	Oncogene Research Products, San Diego, CA, USA, Cat # NA13	1:200
SC35	mouse	sheep- α -mouse-Cy3	Sigma S 4045	1:1000
vimentin XL-VIM-14.13	mouse	sheep α mouse-Cy3	Progen, Heidelberg	undiluted

Secondary and tertiary antibodies

Antibody / avidin	Provider	Common working dilution
avidin-Cy5	Jackson ImmunoResearch, West Grove, USA 003-170-083	1:1000
goat- α -rabbit-Biotin	Camon, Wiesbaden BA-1000	1:1000
goat- α -rabbit-FITC	Tago / Biosource, Solingen	1:1000
goat- α -rat-Rhodamine	Jackson ImmunoResearch, West Grove, USA 515-165-062	1:100
sheep- α -mouse-Cy3	Jackson ImmunoResearch, West Grove, USA 515-165-062	1:200

2.2.9 Staining of nuclear DNA with Propidium Iodide (PI)

PI is a dye, which stains nucleic acids. It can be used as a nuclear counterstain. For confocal microscopy it has the advantage not to require UV-excitation. It stains DNA as well as RNA. To remove the strong RNA staining in the nucleoli, cells are treated with RNase before staining.

Reagent	Supplier / Catalog Number	Stock Solution	Final Concentration
PBS	(see 2.1.2)		1x PBS
RNase A	Roche (Boehringer Mannheim) 109169	1% (500 U/ml) in 10 mM Tris-HCl pH 7.5	20 U/ml
Propidium Iodide	Sigma P 4170	5 μ g/ml in PBS	5 μ g/ml

Protocol

1. Incubate cells in 20 U/ml RNase A (stock solution 1:25) 25 min at 37°C.
2. Wash shortly in PBS.
3. Incubate 5 min in 5 μ g/ml PI.

2.3 Microscopy**2.3.1 Transmitted light microscopy**

Transmitted light microscopy was used for four purposes:

1. alone, for checking the status of cultured cells in phase contrast mode
2. alone, for preparing gridded coverslips
3. alone, for selecting microirradiation positions in the nucleus in phase contrast mode
4. in combination with fluorescence microscopy (epifluorescence with widefield excitation and laser-scanning microscopy).

When transmitted light microscopy was used in combination with laser-scanning microscopy, this was often done without a special contrast mode (phase contrast or

DIC). In this way, the intensity of illumination light was minimized and sufficient contrast could be achieved by electronic contrast enhancement.

Transmitted light microscopy delivers valuable information about the state of cells and about the location of cellular structures even without a specific fluorescence staining. It requires only low light excitation and therefore in general is not prone to inducing photodamage. When used on cells sensitized for laser-UVA microirradiation, however, the UV part of the excitation light has to be filtered out.

As the processes involved in the image formation of transmitted light microscopy are more difficult to model than the fluorescence process and the resulting images are structurally more complex, images from transmitted light microscopy are usually “only” evaluated visually, not quantitatively. There are, however, attempts to relate transmission images to simple quantities like the local refractive index (Arnison *et al.* 2000).

Microscope used for cell culture

Microscope / parts	Type	Supplier
Cell culture phase contrast microscope	Zeiss Axiovert 25 C	Carl Zeiss, Jena
Objectives	CP Achromat x5 / 0,12 CP Achromat x10 / 0,25 Ph1 LD Achrostatigmat x20 / 0,3 Ph1 LD Achrostatigmat x40 / 0,55 Ph2	

2.3.2 Epifluorescence microscopy with widefield excitation

Epifluorescence microscopy with widefield excitation was mainly performed for visual checking of the staining quality of preparations. In some cases digital images of microirradiated and stained cells were recorded this way. In spite of its strong curvature of field, the Fluar 40x/1.3 Ph3 objective was particularly useful in this case, because it allowed imaging of cells and gridded coverslips in phase contrast mode.

Microscope / parts	Type	Supplier
Epifluorescence microscope	Axiophot 2	Zeiss, Jena
Objectives	Plan-Neofluar 16x / 0,5 multi Plan-Neofluar 40x / 1,3 oil Plan-Apochromat 63x / 1,4 oil Plan-Neofluar 100x / 1,3 oil Fluar 40x / 1.3 Ph3 oil	

Microscope / parts	Type	Supplier
Fluorescence filters	DAPI (BP 353 - 377 nm, FT 395 nm, LP 397 nm) FITC (BP 450 - 490 nm, FT 497 nm, LP 502-542 nm) Cy3 (BP 534 - 558 nm, FT 560 nm, BP 575 - 640 nm) Cy5 (BP 575 - 625 nm, FT 645 nm, BP 660-710 nm) Triple-Filter (TBP 400/495/570, FT 410/505/585, TBP460/530/610)	
Video zoom		
CCD-camera	Coolview CCD Camera System	Applied Imaging, Newcastle Upon Tyne, UK
Software	Cytovision	Applied Imaging, Newcastle Upon Tyne, UK

2.3.3 Laser-scanning microscopy

Laser-scanning microscopy was performed with two intentions:

1. Recording of stacks of fluorescence images with a limited depth of focus (*confocal* laser-scanning microscopy) for the 3D analysis of nuclear structures.
2. Recording of widefield fluorescence images. The almost complete automation of common laser-scanning microscopes greatly facilitates the recording of large numbers of images. Fully automated epifluorescence microscopes with widefield excitation are still uncommon and were not accessible for this work.

Microscope / parts	Type	Supplier
Confocal laser-scanning microscope	Zeiss LSM410 location: Munich, Institute for crystallography, LMU	Zeiss, Jena
Objectives	Plan-Neofluar 63x / 1.25 oil Ph3 Plan-Apochromat 63x / 1,4 oil	

Microscope / parts	Type	Supplier
Lasers	Ar ⁺ -laser 488 nm, 15 mW HeNe-laser 543 nm, 0.5 mW HeNe-laser 633 nm, 5 mW N ₂ -laser, pulsed, 337 nm, 20 ns, 0 - 65 µJ per pulse, for laser microdissection, not scanned	
Dichroic mirror	FT 488 / 543	
Emission filters	FITC (BP 502 - 542) Cy3 (BP 575 - 640) Cy5 (LP 650)	
Software	LSM 410 software version 3.95	
Confocal laser-scanning microscope	Zeiss LSM 510 location: Hiroshima, Institute for radiation biology, University of Hiroshima	Zeiss, Jena
Objectives	Plan-Neofluar 40x/0.75, Ph 2 C-Apochromat 40x/1.2 Plan-Apochromat 63x/1.4	
Lasers	Ar ⁺ -laser 351 / 364 nm Ar ⁺ -laser 457 / 488 / 514 nm HeNe-laser 543 nm HeNe-laser 633 nm	
Dichroic mirror	HFT UV/488/543/633	
Emission Filters	BP 505 - 530 nm LP 560 nm	
Software	LSM 5 version 2.02	
Confocal laser-scanning microscope	Leica TCS SP location: Munich, zoological institute, LMU	Leica, Heidelberg
Objective	Plan-Apochromat 100x / 1.4 oil	
Lasers	Ar ⁺ -laser 457 / 488 / 514 nm HeNe-laser 633 nm	
Dichroic mirrors	RSP 525 TD 488 / 568 / 647	

Microscope / parts	Type	Supplier
Emission filters	Spectrally adjustable detection system. Adjustment: GFP (490-540 nm), PI (590-680 nm), Cy5 (650-750 nm)	
Software	TCS-SP software	

2.3.4 Measurement of the chromatic shift

Materials

Material / Equipment	Type	Supplier
Coverslips	even thickness 0.17 mm	(see 2.1.4)
Slide glass	76x26 mm	R. Langenbrink / Schubert & Weiss
Multispectral fluorescent beads	Tetra Speck 500 T-7281	Molecular Probes
Mounting medium	as used for biological specimen	
Nail polish		
Microscope		
Computer with ImageJ and Sync Measure 3D plugin		

Preparation of coverslip with multispectral fluorescent beads

1. Clean dust from coverslip.
2. Shake the tube containing the beads to make a homogeneous suspension.
3. Drop 5 μ l of bead suspension onto the center of the coverslip.
4. Spread the suspension over the coverslip with the pipette tip as far as the surface tension permits.
5. Cover the coverslip to protect the beads from light and dust and let it dry (approx. 1 h).
6. Mount in the appropriate mounting medium on glass slides.
7. Seal with nail polish.

Recording of image stacks and evaluation

1. On the microscope find a region on the slide, where the beads are dense enough so that several beads fit into one image at the image parameters also used for biological specimens. The beads should still be separated from each other by at least two bead diameters.
2. Record image stacks of the color channels of interest with the settings used for biological specimens. In particular, the zoom region within the field of view of the objective should be the same (preferentially in the middle of the field). Collect at least 15 beads altogether.
3. Load the image stacks of the recorded color channels as a separate grayscale images into ImageJ.
4. Start the plugin Sync Measure 3D. Select all color channels and press "Start Measurements".
5. For each channel select an appropriate threshold with the respective threshold slider to isolate the beads.

6. Measure the position of each bead:
 - Draw a region of interest, which contains one bead in all color channels, but excludes all other beads.
 - Click into the region of interest, while keeping the “Alt” key pressed. The “Sync Measurements” window is opened and the intensity gravity center in all color channels and other parameters are displayed.
 - Move the region of interest to the next bead. Proceed with all other beads as with the first bead.
7. When the positions of all beads are measured, press the “Stop Measurements” button. The averaged shift of each color channel with respect to the first color channel is calculated and displayed in the last two lines of the “Sync Measurements” window.

2.3.5 Preparation of cells for live cell microscopy

Live cell microscopy of mammalian cells over several hours requires that the cells be kept at a temperature of 37°C on the microscope stage. The pH has to be kept constant at 7.4, which requires a CO₂ atmosphere, an airtight assembly or the use of cell culture medium without carbonate buffer. These requirements led to the development of dedicated commercially available live cell microscopy systems. To protect cells against photodamage, 100 - 500 µM Trolox, a water soluble vitamin E derivative, which acts as a scavenger of free radicals, was added to the growth medium the day before observation.

Materials

Reagent	Supplier / Catalog Number	Stock Solution	Final Concentration
Cell culture medium for the respective cell type	(see 2.1.1)		
Trolox ((+)- 6-Hydroxy-2,5,7,8-tetramethyl-chroman-2-carbon-acid)	Fluka 56510 or Aldrich 23,881-3	100 mM in ddH ₂ O (5 g / 200 ml) store at RT or +4°C	100 - 500 µM
Ethanol	Merck, Darmstadt		100%

Material / Equipment	Type	Supplier
Cells		
Coverslips	round, diameter 40 mm for Bioptechs live cell chamber	(see 2.1.4)
Fine forceps	(see 2.1.4)	(see 2.1.4)
Live cell microscopy chamber system	FCS2 living cell chamber / objective heater	Bioptechs, Butler, USA
Flexible-tube pump	flow rate 0.03-8.2 ml/min cat. no.: 3-1920	neoLab, Heidelberg
Tygon tubing	2275, ID 1/16" (1.6 mm)	Fisher Scientific, Schwerte
2 Tube connectors	Luer Lock for ID 1.6mm, female, cat. no.: 2-1886	neoLab, Heidelberg

Material / Equipment	Type	Supplier
1 Tube connector	Luer Lock for ID 1.6mm, male, cat. no.: 2-1880	neoLab, Heidelberg
Sterile filter	0.45µm yellow, cat. no.:26 71 19001	Sartorius / Schubert & Weiss, Munich
Plastic syringe	20ml with Luer lock (not cone) cat. no.: 500 933	Braun Melsungen / Schubert & Weiss
Plastic tubes	Falcon 50 ml	Becton Dickinson / Schubert & Weiss, Munich
Rack	for tubes 50 ml	Schubert & Weiss
Petri dishes	Falcon Easy Grip 50 mm	(see 2.1.4)
Cell culture incubator	(see 2.1.2)	(see 2.1.2)
Sterile workbench	(see 2.1.2)	(see 2.1.2)
Autoclave	Varioklav 400	H+P Labortechnik GmbH, Oberschleißheim

Protocol

1. The day before the experiment split cells on coverslips (see 2.1.4) and add 100 µM trolox to the growth medium. If necessary, synchronize cells (see 2.1.5).
2. Put 30 ml of fresh medium in a falcon tube. Add 100µM trolox. Put tube into the cell culture incubator. Leave the lid partially unscrewed to allow gas exchange. Incubate overnight for CO₂ equilibration.
3. Prepare tubing and rinse it with ddH₂O. Assemble tubing in 3 pieces:
 - a. Tubing from syringe through pump to filter consisting of:
 - female luer connector
 - 25 cm tube
 - flexible tube of the pump (11,45 cm, with connectors)
 - 50 cm tube (from pump to microscope stage)
 - male luer connector
 - b. Tubing from filter to chamber:
 - female luer to tube connector
 - 5 cm tube
 - c. Tube ~70 cm from chamber to waste
4. Autoclave FCS2 white support, gaskets and tubing at 115°C.
5. Sterilize the microacqueduct slide in a petri dish with 100% Ethanol (not too long, otherwise the contacts come off).
6. Prepare a petri dish with medium for washing.
7. Have an empty petri dish ready (for waste medium).
8. Assemble the supply tube. The order is:
 - part a (from above)
 - sterile filter
 - part b (from above)
9. Suck 15 ml of equilibrated medium into a 20 ml syringe.
10. Connect the syringe to the supply tube (at part a) and press medium all the way through. Take care to avoid air bubbles, particularly in the filter.
11. Place the white support in front of you, the side that will hold the temperature control pointing towards you.

12. Wash the gasket with holes in medium and place it onto the the FCS2 white support.
13. Place the microacqueduct slide on top of the gasket.
14. Wash the second gasket (1 mm) and place it onto the microacqueduct slide.
15. Level off the white support by putting forceps underneath on the far end.
16. Wash the chamber with 1 ml medium.
17. Pipet 1 ml medium into the chamber.
18. Place slide with cells onto the chamber.
19. Put metal body on and tighten.
20. Turn the chamber over taking care that no medium leaks out. (keeping the metal tubes horizontal). The attachment for the temperature control is now pointing away from you.
21. Connect the supply tubing (with syringe) to the left metal tube. And the waste tube to the right metal tube.
22. Wipe off any excess medium outside the chamber. Take care that the contacts of the microacqueduct slide are dry.
23. Place a tiny drop of immersion oil on the temperature sensor of the temperature control and screw the control to the chamber.

2.3.6 Laser-photo-bleaching and live cell microscopy at the LSM 410

Materials

Material / Equipment	Type	Supplier
Cells mounted in live cell chamber (see 2.3.5)	HeLa with stably incorporated H2B-GFP	(see 2.1.1)
Plastic tubes	Falcon 50 ml	(see 2.3.5)
Rack	for tubes 50 ml	(see 2.3.5)
Flexible-tube pump	flow rate 0.03 - 8.2 ml/min	(see 2.3.5)
Solid-state relay, cables and connectors	SSR: ordering number 18 62 79-88	Conrad Elektronik, München
Confocal laser-scanning microscope	Zeiss LSM 410	Zeiss, Jena
Objective	Plan-Apochromat 63x / 1,4 oil	
Laser	Ar ⁺ -laser 488 nm, 15 mW, run at 30%	
Dichroic mirror	FT 488 / 543 nm	
Emission filter	BP 505-535 nm	
Software	LSM 410 software	Zeiss, Jena
	macro for 4D-imaging (3D + time)	own programming

Protocol

1. Warm the live cell chamber and the objective to 37°C with the objective heater.
2. Attach the live cell chamber at the microscope and the supply tube at the pump. The pump is connected to the LSM 410 PC via the solid-state relay (see Figure 3.29).
3. Image the cells in simultaneous fluorescence and transmission mode with a laser attenuation of 0.003, and select an appropriate field of view.
4. In the macro, select the position for each cell, which is to be imaged. Select one position as an overview image at Zoom 1. Select the imaging parameters.
5. Adjust the parameters for the coverslip search. The coverslip search is performed before each image stack is recorded. It compensates for focal drift.
6. Record an image stack for each selected position.
7. Bleach the cells:
 - For each cell change to the “tune img” mode.
 - Image the cell at highest zoom.
 - Select the ROI (region of interest) that is to be bleached. The ROI constrains the bleached region in the vertical direction only. In the horizontal scan direction the whole field is bleached.
 - Image the ROI 2-4 times at different axial positions without attenuation. The ROI is bleached.
 - Set the laser attenuation and the image parameters back to the previous values and leave the “tune img” mode.
 - Record an image stack of the cell.
8. After bleaching all cells, start the 3D-time series. Select the pump time so that the pump runs for one minute each hour. With this setting 1 ml medium is pumped into the chamber in three hours at lowest pump speed.

2.4 Evaluation

2.4.1 Software

Images were Gauss or Median filtered and contrast corrected for display in Amira, ImageJ, the LSM 410 dummy software, the LSM 5 Image Browser or Photoshop, whatever was most convenient for the next processing steps. Maximum intensity projections were performed in ImageJ or the LSM 410 dummy software. 3D surface and volume renderings were performed with Amira. When brightfield images were recorded in laser-scanning transmission mode at low zoom, shading, i.e. uneven illumination, was a common problem. This shading was corrected with a plugin (“FFT-Filter”) written for ImageJ.

Visual inspection of 4D live cell data was performed with a macro (“DISPT”) written for the LSM 410 dummy software or with the LSM 5 Image Browser. Protein accumulations after laser-UV-microirradiation were scored using ImageJ and Microsoft Access.

Curve fitting to numerical data was done with Gnuplot. Diagrams were prepared with Microsoft Excel.

This thesis was written with Microsoft Word 2000.

Image processing software	Manufacturer
Amira (versions 2.0 - 2.3)	TGS, Merignac, France http://www.amiravis.com
Gnuplot (version 3.7.1)	http://www.gnuplot.info/
Illustrator (version 9)	Adobe Systems, Inc., San Jose, USA
ImageJ (versions 1.20 - 1.30)	(Rasband 1997-2003)
LSM 410 dummy software (version 3.98)	Carl Zeiss, Jena
LSM 5 Image Browser (versions 2.8 - 3.1)	Carl Zeiss, Jena
Office (versions 97 - 2000)	Microsoft, Redmond, USA
Photoshop (versions 4 - 6)	Adobe Systems, Inc., San Jose, USA
SPSS 11.0	SPSS Inc. Chicago, Illinois, USA

2.4.2 The fourfold-point correlation

To test, whether the fractions of cells with Rad51 accumulations and cells with Mre11 accumulations after microirradiation are dependent (section 3.1.3), the fourfold-point correlation (Zöfel 2001) was calculated for each time interval as

$$r = \frac{n_{-} \cdot n_{++} - n_{+-} \cdot n_{+}}{\sqrt{(n_{-} + n_{+-}) \cdot (n_{+-} + n_{++}) \cdot (n_{-} + n_{+}) \cdot (n_{+-} + n_{++})}}$$

, where

r : the fourfold-point correlation

n_{-} : number of cells without Rad51 foci accumulations or Mre11 accumulations

n_{+-} : number of cells without Rad51 accumulations but with Mre11 accumulations

n_{+} : number of cells with Rad51 accumulations but without Mre11 accumulations

n_{++} : number of cells with both Rad51 accumulations and Mre11 accumulations.

The fourfold-point correlation can be calculated in the case that two variables are compared, which can assume only two values. It is equivalent to Pearson's correlation but easier to calculate.

The expression

$$\chi^2 = n \cdot r^2 \quad \text{with } n = n_{-} + n_{+-} + n_{+} + n_{++}$$

is χ^2 distributed with one degree of freedom, and was used to calculate the significance of the correlations.

3 Results

3.1 Localization and dynamics of DNA-repair proteins studied by laser-UVA-microirradiation

3.1.1 Setup of the microirradiation systems

The principle of laser-UVA-microirradiation is to illuminate a volume which is small compared to the cell nucleus with UVA light, and to induce DNA damage in this volume (Figure 3.1). For selecting the position of the microbeam with respect to the cell, in principle two methods can be used: moving the target, while keeping the laser beam fixed at one position, and moving the laser beam, while keeping the target at rest. In this work, the first option was used with a laser microdissection system (P.A.L.M., Bernried). The second option was used for microirradiation with a laser-scanning microscope equipped with a UVA-laser for imaging of UVA-excitabile fluorochromes (LSM 510; Zeiss, Jena), which was adapted for microirradiation.

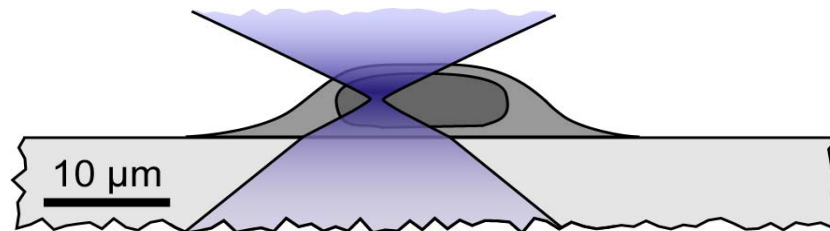


Figure 3.1: Scheme depicting a microirradiation beam hitting a fibroblast cell nucleus. The fibroblast cell is growing on a glass coverslip. The scheme is drawn approximately to scale.

3.1.1.1 The P.A.L.M. microdissection system

The P.A.L.M. microdissection system is coupled into a Zeiss LSM 410 laser-scanning microscope. This setup was established to allow for high-resolution three-dimensional fluorescence imaging starting within seconds after irradiation. This option was not used for this work, however.

The system works with a pulsed N_2 -laser ($\lambda=337$ nm) with a pulse-length of 20 ns and a maximal pulse frequency of 31 Hz. The pulse energy can be tuned with a rotatable absorption filter, whose absorption varies exponentially with the angle of rotation. The rotation angle is measured in arbitrary units (a.u.) ranging from 0 to 100. The pulse energy was measured before passing through the objective with a power meter. For microirradiation the laser was operated at a power slightly lower than the sensitivity of the power meter (rotation angle 30 a.u.). The pulse energy for this setting was extrapolated from the energies measured for higher settings (Figure 3.2) to 0.08 μ J. Irradiation was performed with a 63x/1.25 Plan-Neofluar oil-immersion objective. As the transmission of this objective is specified to 10% at 337 nm, the energy delivered to the target was estimated to 8 nJ per pulse. This is only a rough estimate, as it is not known, if and how much the back focal plane of the objective is overfilled by the UV-laser beam. Furthermore, it is unclear, how much light is lost at the boundary between coverslip and cell. For a more precise determination of the energy delivered to the target, an in-situ measurement of the power behind the objective and a coverslip in an aqueous medium would be necessary.

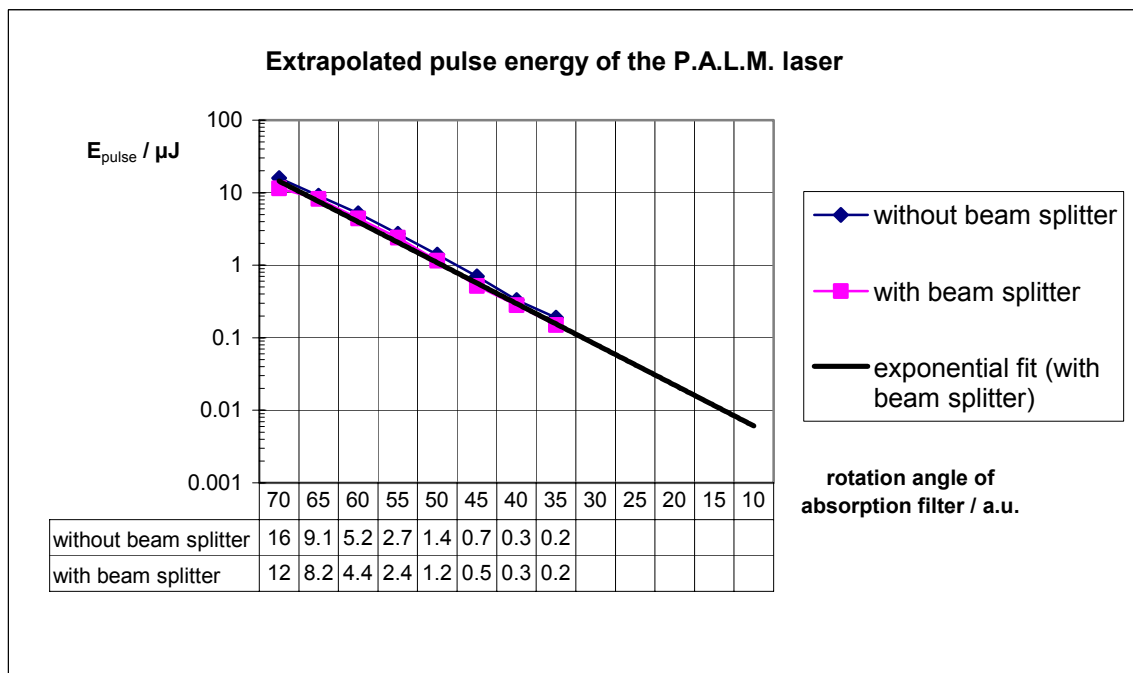


Figure 3.2: Measurements and extrapolation of the UV pulse energy of the P.A.L.M. laser

The beam splitter designed for this microscope setup maximally transmits in the UV and IR and transmits 50% in the visual range. Energy measurements were performed with and without the beam splitter. Extrapolation was performed for the values taken in the presence of the beam splitter.

The curve goes into saturation above an energy scale of 70. Only the part of the curve, where the pulse energy varies exponentially with the scale has been displayed and used for the fit, here. In this part, the energy approximately doubles every five a.u.

Calibration of the laser focus position was performed as described in protocol 2.2.4. Cells were kept on the microscope stage in a FCS2 live cell chamber (Bioprotech, Butler, USA) operated as an open chamber.

3.1.1.2 Adaption of a Zeiss LSM 510 for microirradiation

The Zeiss LSM 510, which I used during my stay at the institute for Radiation Biology in Hiroshima, is equipped with an Argon-ion laser emitting UVA-light (351 and 364 nm) for imaging UVA-excitable fluorochromes. The beam of this laser can be pointed at arbitrary positions all over the field of view with the scanning mirrors. The power of the 364 nm line can be adjusted via an acousto-optical filter (AOTF) from 10 to 300 μW as measured with a power-meter behind the focus of a 40x/0.75 Air Plan-Neofluar Ph2 objective, the objective used for microirradiation in this work.

In the experiments with the P.A.L.M. system UVA-doses in the range of 10 - 100 nJ were required to induce Rad51 accumulations at irradiated spots in cell nuclei sensitized with the BrdU/Hoechst method (see 3.1.2). To keep the irradiated cells viable and to minimize additional unspecific damage, the UVA-dose should be kept within this range. As the time for opening and closing the mechanical laser shutter of the LSM 510 is in the order of 1 second, the minimal UV-dose produced by switching the laser beam with this shutter (10 - 300 μJ) is at least 250 times larger than the required energy. Hence the AOTF was employed that allows switching the laser within microseconds.

The easiest way to irradiate a selected nuclear site would be to aim the laser at this site using the scanning mirrors and then turn the laser beam on for the desired time. However, due to limitations either in the hardware or in the software (LSM 510 software version 2.02) this procedure could not be implemented. Instead, the "Bleach

ROI" function of the LSM 510 software was used to control the laser energy. This function allows the illumination of an arbitrarily shaped region of interest (ROI) within a given zoom region. When ROI-bleaching is performed, the laser is scanned over the full width of the zoom region, but laser light is transmitted by the AOTF only at those pixels that are located within the user defined ROI. For microirradiation a square ROI of 3x3 pixels in the centre of a zoom region of 512x512 pixels at highest zoom (pixel spacing 50 nm) was chosen (Figure 3.3).

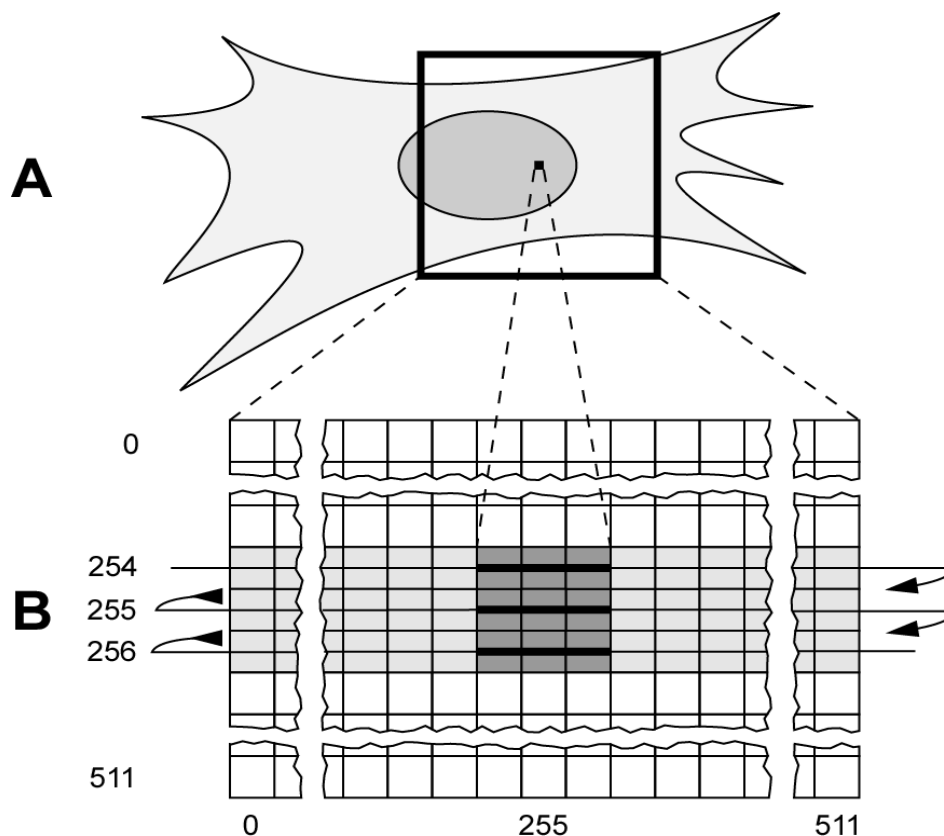


Figure 3.3: Scheme of Laser-UV-microirradiation with the "Bleach ROI" function

(A) Selection of a nuclear region for microirradiation is achieved as follows. The scanfield is zoomed up maximally (black outline), and the middle of the scanfield (black spot) is moved to coincide with the irradiation position.

(B) Enlarged scheme of the scanfield of 512x512 pixels with each square representing one pixel. When irradiation is performed, the scanning mirrors move the UVA-laser focus over the whole width of the scanfield (grey pixels), but the AOTF only transmits UVA-light when the focus passes over the middle three pixels of the scanfield (dark grey pixels).

Microirradiation was performed with the laser-scanner working at a pixel time of 1.76 μs . Therefore; the actual microirradiation was performed with a sequence of three pulses of 5.28 μs each. At maximal laser power (300 μW) this amounts to a total energy of 4.8 nJ. However, since the rise time of the AOTF was specified to be 2 μs , and the energy, which is transmitted during this time, was not known, the energy actually transmitted during a microirradiation pulse possibly differed largely from the estimated value. Because of this and to overcome uncertainties in the efficiency of the sensitization of cells to UVA light, cells were irradiated with a range of the estimated energies (1 - 500 nJ). The energy used for further experiments was calibrated by the biological response, i.e. Rad51 accumulation, of the cells to the microirradiation (see section 3.1.2 page 48). The energy was varied by repeating the irradiation several times or by attenuating the laser.

The size of the laser spot was determined by measuring the point spread function (PSF) of the microscope with an open confocal pinhole. The PSF of a confocal microscope is the product of the PSF of its excitation path and the PSF of its detection path. The former is identical to the intensity distribution of the exciting laser, whereas the latter is determined by the detection pinhole. As the intensity distribution of the exciting laser was at question here, this pinhole was maximally opened, leading to a uniform PSF of the detection path. The PSF was measured by imaging subresolution sized fluorescent latex beads (PS-Speck; Molecular Probes, Eugene, OR, USA) with the UVA-laser ($\lambda = 364$ nm) in laser-scanning mode. As the objective was operated with a Wollaston prism for differential interference contrast, two images of each bead appeared with a distance of 500 nm at an angle of 45° . This made it impossible to measure a meaningful full width at half maximum (FWHM) of the PSF. After background subtraction it was found that 90% of the total intensity in the focal plane were contained within a circle of 1.8 μm diameter. This size is two and a half times the diameter of the Airy disk of a laser beam with $\lambda = 364$ nm focused through an objective with a numerical aperture of 0.75 (as used here). This broadening can be attributed to three reasons: First, the Wollaston prism broadened the PSF by 500 nm. Second, the refractive index (R.I.) of the immersion medium of the objective used here (air, R.I. = 1), was not matched to the aqueous embedding medium (R.I. ~ 1.33) of the target (cells or beads), leading to spherical aberration. Third, the objective was not well corrected for focusing a UV wavelength of 364 nm. The diameter of the laser spot at 3 μm axial distance from the focus (corresponding to the upper or lower edge of a cell nucleus 6 μm high, which is irradiated in the center) was measured to be approximately 4 μm . This finding is in agreement with the numerical aperture of 0.75, which in aqueous medium corresponds to a half opening angle of the beam of 34° .

The lateral position of the irradiated spot could be chosen by varying the offset of the scanning region. It was calibrated using a test preparation, which consisted of a coverslip painted with black marker (see protocol 2.2.5). To allow a fast selection of the irradiation positions in the nucleus of living cells, the positions were marked in a phase contrast image recorded at the lowest possible zoom setting with the fastest possible scan speed (0.88 $\mu\text{s}/\text{pixel}$). At these settings a strong shift between the irradiation position as specified by the offset parameter and the measured irradiation position was found. The shift had a constant component and a component varying linearly with the position within the scan field. The linear component was largest in the direction of the fast scanning axis. For two positions, which were 100 μm apart in this direction, the shift differed by 5 μm . This could well have the effect that an irradiation aimed to be within the cell nucleus actually hits a position outside the nucleus and therefore has no effect. Hence both constant and linear component of the shift had to be corrected.

Nuclear positions were interactively selected for microirradiation using a macro written by me in the VBA macro language for the LSM 510 software. This macro controlled the microirradiation procedure setting the irradiation energy and correcting the positions for constant and linear shift. With this macro up to 140 positions could be selected and microirradiated within 5 minutes. The positions can be stored to disk, and can be displayed for evaluation with a plugin written for ImageJ.

3.1.2 Rad51 accumulates at irradiated nuclear sites in human fibroblasts

To study the localization of Rad51 with respect to the site of damage during DNA repair the human SV-40 transformed fibroblast cell line GM02063 (Xia *et al.* 1996) was used. A fraction of nuclei in growing cell cultures showed scattered Rad51 foci after immunofluorescence staining for Rad51 (Figure 3.4). To test whether cells showing these foci were in S phase, cultures were pulse-labeled with BrdU for 30 min and double stained for Rad51 and BrdU. 42% of the cells (n=200) showed focally concentrated signals of Rad51 scattered throughout the nuclei. 93% of these Rad51 foci-positive cells also showed incorporation of BrdU, indicating that most cells with Rad51 foci were indeed in S phase as reported previously for other human cells (Tashiro *et al.* 1996; Scully *et al.* 1997b).

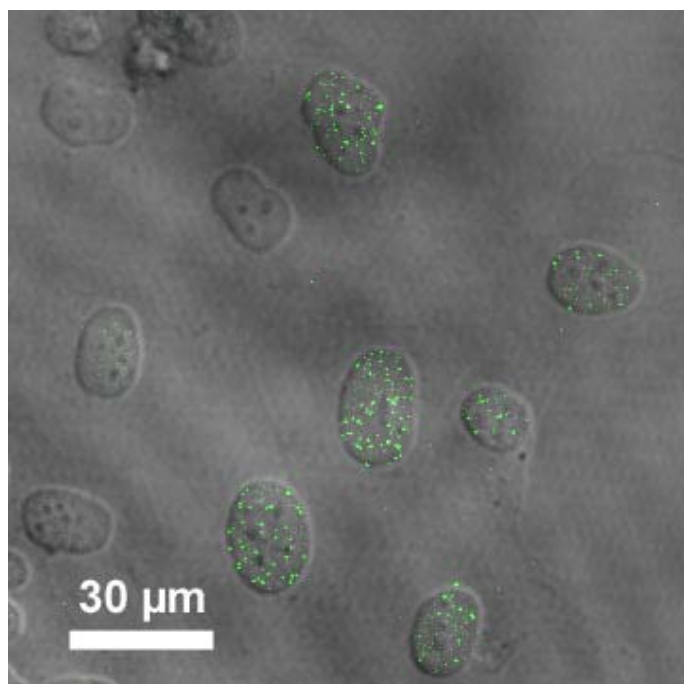


Figure 3.4: Rad51 immunostaining in non-irradiated GM02063 cells.
Mid-nuclear optical section. green: Rad51 immunofluorescence staining, gray: transmission image

For the microirradiation experiments, cells were seeded on gridded coverslips and sensitized to UVA-light by labeling of nuclear DNA with BrdU. Incorporation of BrdU was achieved by addition of 10 $\mu\text{g/ml}$ BrdU to the growth medium for 20 h (see section 2.2.3). Cells from labeled and unlabeled cultures were microirradiated at a single nuclear site with the P.A.L.M. microdissection system (estimated energy: 1200 nJ per site, 8 nJ per single pulse). Approximately 30 min later microirradiated and nonirradiated cells on the same slide were fixed and subjected to immunostaining for Rad51. Light optical nuclear sections were obtained with a confocal laser-scanning microscope. In addition to Rad51 S-Phase foci microirradiated cells contained single larger and more intense Rad51 immunostaining signals (Figure 3.5). To distinguish these signals from the smaller Rad51 foci, which are not induced by the irradiation, they are subsequently called “Rad51 accumulations”.

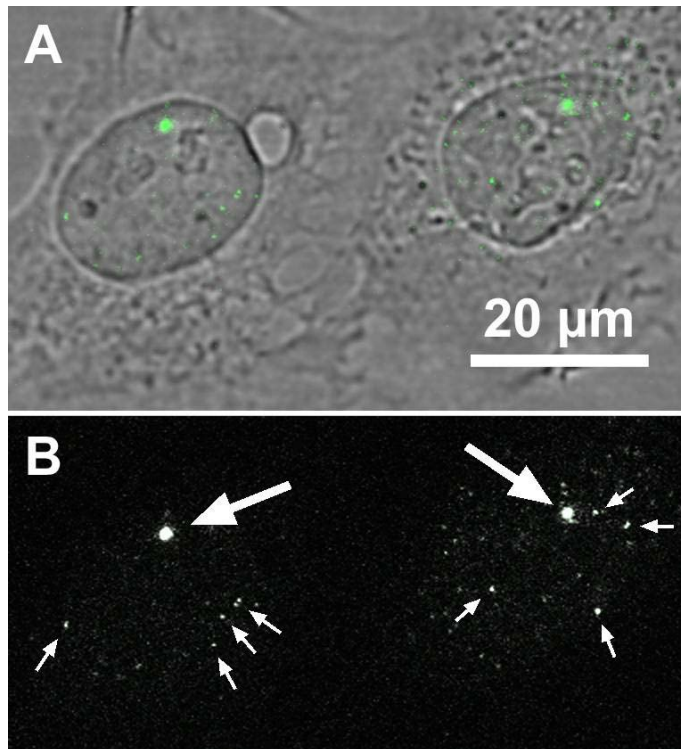


Figure 3.5: GM02063 cells after laser-UVA-microirradiation at a single nuclear site

The image shows best focus optical sections.

(A) Two microirradiated cells after immunostaining for Rad51. Green: immunofluorescence staining for Rad51, gray: transmission image

(B) Grayscale of the Rad51 immunostaining of the same cells. The Rad51 accumulations are marked by large arrows. Some Rad51 foci are marked by small arrows.

Accumulations of Rad51 were noted in 38% ($n = 52$) of the microirradiated nuclei from BrdU-labeled cultures. These accumulations were never observed in non-irradiated cells on the same slides or in cells from non-labeled cultures microirradiated with the energy employed in this experiment. Hence, the formation of Rad51 accumulations requires both BrdU labeling and microirradiation.

Rad51 accumulations were also observed when unlabelled cells were irradiated with single pulses of much higher energies (1 pulse of 440 nJ). This effect can be attributed to the high temperature, which is produced in a single short laser pulse of high energy as compared to repetitive illumination with low energy pulses. The effect is utilized for laser-microdissection (Greulich and Leitz 1994) and was applied here as a positive control to verify the functioning of the microirradiation system.

62% of the microirradiated cells did not show any Rad51 accumulation at the microirradiated nuclear site. 78% of these cells did not have any Rad51 staining above the background at all. 22% (13% of all irradiated cells), however, had nuclear Rad51 foci. This means that in 25% of all irradiated cells containing Rad51 the protein did not accumulate at the irradiated site. As after 20 h of incubation with BrdU 11% of GM02063 cells do not show BrdU incorporation this finding can partially be explained by the assumption that irradiated cells with Rad51 foci but without accumulations were not sensitized to UVA light. After subtraction of this fraction still 14% of all irradiated cells containing Rad51 were sensitized to UVA light, but did not contain Rad51 accumulations. The cause for this is presently not clear. Possibly, these cells undergo a different repair mechanism (NHEJ or SSA) in spite of their ability to perform gene conversion.

To clarify unequivocally if sites of Rad51 accumulation are identical with microirradiated nuclear sites, cells were microirradiated at two nuclear sites (estimated energy: 1200 nJ per site, 8 nJ per single pulse). The two irradiated sites were selected to be located close together (distance less than 4 μm) in one area of the gridded coverslip, whereas in a second area they were selected on opposing poles of the nucleus (more than 10 μm apart). As expected, nuclei with two closely adjacent microirradiation sites also showed two closely adjacent accumulations of

Rad51 (Figure 3.6 A,C), whereas two distant microirradiation sites resulted in two distant sites of Rad51 accumulations (Figure 3.6 B,D). In two of the nuclei, which had been irradiated at two nuclear sites, only one accumulation was found. Possible reasons for this are that the two irradiated sites were very close together so that they appeared as one site or that the irradiation was accidentally performed on a nucleolus.

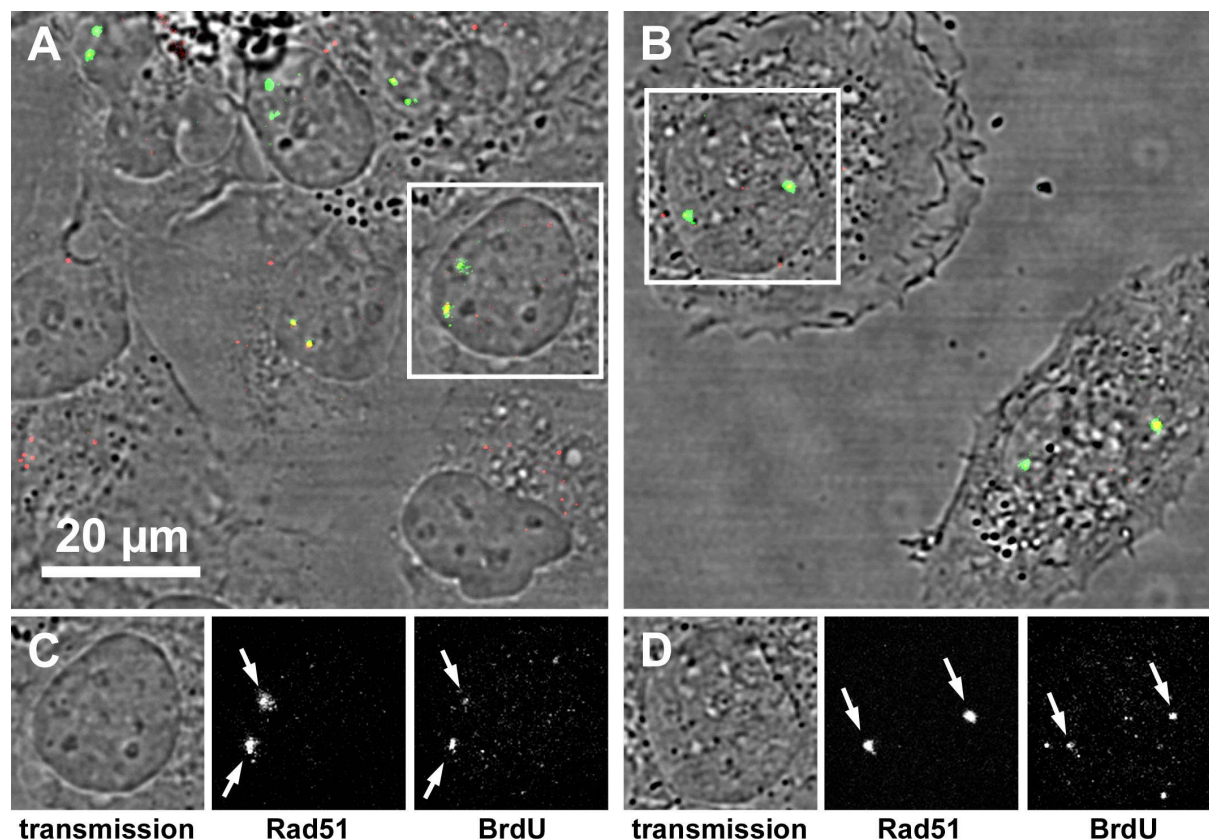


Figure 3.6: GM02063 cells after laser-UVA-microirradiation at two nuclear sites

The image shows best focus optical sections. green: immunofluorescence staining for Rad51, red: immunofluorescent staining for BrdU without a denaturation step, gray: transmission image (A) An area with cells irradiated at two closely adjacent sites (B) An area with cells irradiated at two distant nuclear sites (C), (D) separated color channels of the nuclei outlined in (A) and (B) the colocalization of Rad51 accumulations with sites of BrdU staining (indicating ssDNA) is clearly visible.

In addition to immunostaining of Rad51, BrdU was detected at microirradiated nuclear sites without a DNA denaturing step. With this protocol single-stranded DNA (ssDNA) is detected in BrdU-labeled cells, since anti-BrdU antibodies recognize incorporated BrdU only in ssDNA (Raderschall *et al.* 1999). 72% of the Rad51 accumulations seen in BrdU-labeled cells ($n = 25$) after microirradiation showed colocalization with ssDNA regions (Figure 3.6, C and D).

In a time series, where BrdU-labeled cells were microirradiated at a single site and fixed 10 - 60 min later, accumulation of Rad51 was detected in nuclei as early as 10 - 20 min after microirradiation. This recruitment to the microirradiated nuclear site was more rapid than the increase of the percentage of cells with Rad51 foci noted after whole cell UVC or γ -irradiation (Haaf *et al.* 1995; Raderschall *et al.* 1999), which was first observed 60 min after the induction of DNA damage (see 3.1.5 for more detailed results).

In an experiment, where BrdU-labeled cells were microirradiated with different energies per microirradiation site and fixed 30 - 90 min later, accumulation of Rad51 was detected in nuclei irradiated with an energy of 480 nJ or higher (Table 3.1). It must be noted, however, that in this experiment the applied energies are not well known, as the rotation angles of the absorption filter regulating the beam power, differed by ten or more a.u. from the last value, for which a measurement of the pulse energy had been obtained (cf. Figure 3.2). It is not clear, if the exponential variation of the pulse energy can be extrapolated to these values.

Energy scale	20	25	20	20	25	25
Number of pulses per site	30	30	120	240	120	240
Estimated energy per site / nJ	60	120	240	480	480	960
Rad51 accumulations	no	unclear	no	unclear	yes	yes

Table 3.1: Accumulation of Rad51 in BrdU sensitized GM02063 cells after laser-UVA-microirradiation with different energies of the P.A.L.M. laser ($\lambda = 337$ nm)

Results, where possible Rad51 accumulations could not be clearly distinguished from Rad51 foci as they appear in S-Phase are marked as "unclear".

Rad51 accumulations after laser-UVA-microirradiation with the P.A.L.M. system were found also in GM02063 cells sensitized by the incorporation of BrdU (0.3 μ M together with 2.5 μ M dThd, 20 h) and staining with Hoechst 33258 (see 2.2.3). The accumulations were induced by irradiation with estimated energies of 40 nJ per site or higher. When cells were treated only with BrdU or Hoechst 33258, higher energies (960 nJ, 80 nJ, respectively) were needed to induce Rad51 accumulations. The low increase in energy (only a factor of 2) to induce Rad51 accumulations with Hoechst 33258 staining alone indicates that the dye is a particularly potent sensitizer.

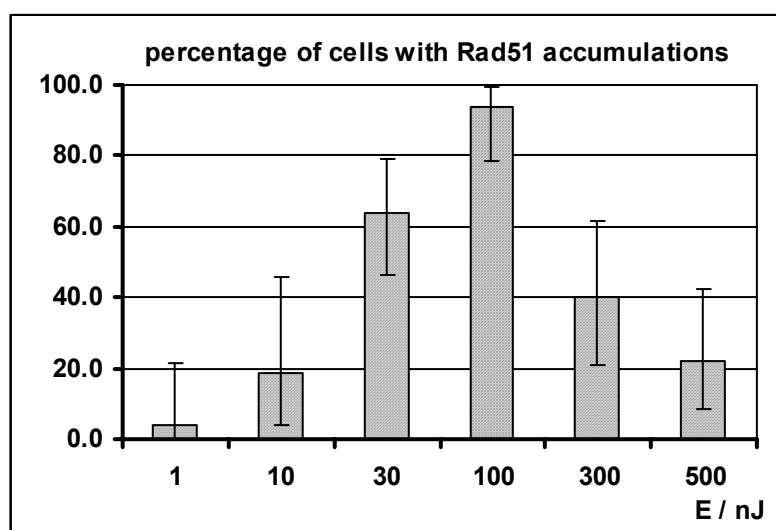


Figure 3.7: Dose dependence of Rad51 accumulation after microirradiation

Percentage of GM02063 cells showing Rad51 accumulations 30-40 min after microirradiation at two sites with different energies of UVA light ($\lambda = 364$ nm). Abscissa: estimated irradiation energy per irradiated spot. Ordinate: percentage of cells with a Rad51 accumulation. The error bars denote 95% confidence intervals. $n = 16$ for 10 nJ. All other data points: $n \geq 24$.

Rad51 accumulations were also found in GM02063 cells, primary fibroblasts and cells of the human colon cancer cell line HCT116 after sensitization with the BrdU/Hoechst treatment and microirradiation with the LSM 510 in Hiroshima ($\lambda = 364$ nm). The dependence of the fraction of GM02063 cells with Rad51

accumulations on the irradiation energy was measured. Sensitized nuclei were microirradiated at two nuclear sites with estimated energies ranging from 1 nJ to 500 nJ. The cells were fixed 30 - 40 min after irradiation, immunostained for Rad51, and the fraction of cells with at least one Rad51 accumulation was counted (see Figure 3.7). At an estimated energy of 1 nJ, only 4% of the irradiated cells showed Rad51 accumulations. For higher energies the fraction of cells with Rad51 accumulations increased. At 100 nJ 94% of the irradiated cells contained Rad51 accumulations. When the energy was increased even further to 500 nJ, the fraction of cells with Rad51 accumulations decreased to 22%. This decrease could indicate that highly damaged cells switch to other repair mechanisms than gene conversion or initiate apoptosis.

To further demonstrate the identity of the sites of Rad51 accumulation with the microirradiated nuclear sites, multiple nuclear sites, which together formed a letter-like pattern, were selected in single cell nuclei. These sites were microirradiated with an energy of 30 nJ each and stored for later retrieval (Figure 3.8 A). Cells were fixed 30 to 90 minutes after microirradiation, and immunostained for Rad51. As expected, in cells, which expressed Rad51, the letter-like microirradiation patterns yielded letter-like Rad51 accumulations (Figure 3.8 B). During the incubation time after irradiation, cells had moved and rotated on the coverslip. To correct these movements, the images were aligned using the nucleoli as reference points (Figure 3.8 A, C). Comparison of the positions of Rad51 accumulations (Fig. 2B) with the irradiation positions (Figure 3.8 A, black crosses) stored at the time of irradiation showed a precise matching.

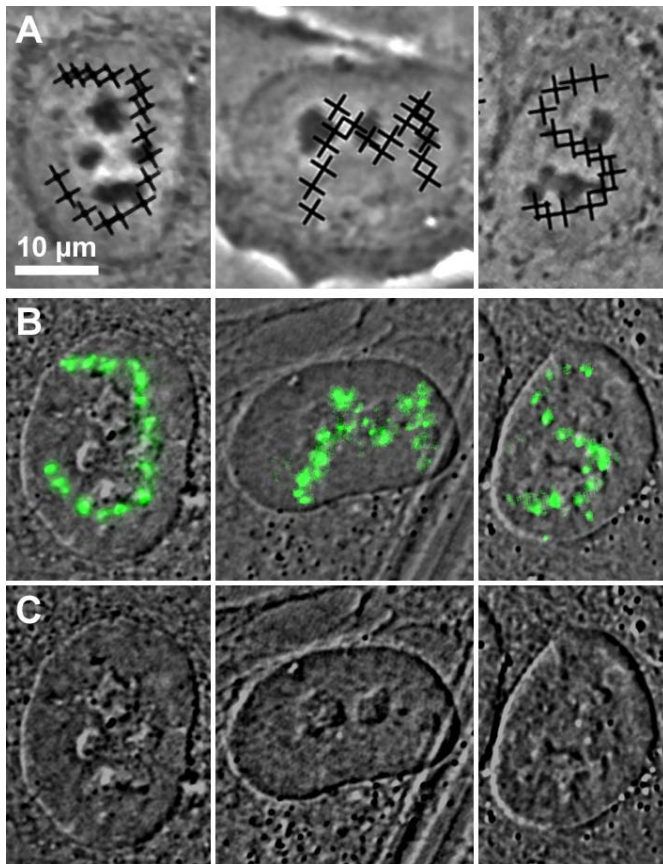


Figure 3.8: Letter-like patterns irradiated in GM02063 cell nuclei

(A) Phase contrast images of three nuclei recorded prior to microirradiation. The positions selected for microirradiation are marked with black crosses.

(B) Widefield fluorescence images from the same cell nuclei fixed 30 - 90 min after microirradiation show immunocytochemically detected Rad51 (green). Transmission images (grey) are overlaid to show nuclear borders.

(C) Without overlay of fluorescence images nucleoli are clearly visible in the transmission images as structures with dark and light outlines (compare A).

Images (B) and (C) are rotated to the same orientation as the images in (A).

from (Walter et al. 2003a)

3.1.3 Rad51 accumulation at irradiated sites is a specific reaction to DNA damage

To exclude the possibility that the Rad51 accumulations at microirradiated sites are caused by unspecific effects different from the DNA damage induced by microirradiation, a series of control experiments was performed. Such unspecific effects could be for example a chemical modification of the microirradiated site, which binds the primary or secondary antibody without a protein accumulation. Another effect could be a modification of the microirradiated site, which leads to a trapping of all nuclear proteins, which diffuse through the site, irrespective of their function resulting in the accumulation of all kinds of nuclear proteins. To exclude these possibilities GM02063 cells microirradiated after sensitization with the BrdU/Hoechst system were immunostained for Rad51 and other proteins, which are involved in transcription and splicing. It was reasoned that damaged sites are not transcribed, and hence an accumulation of one of these proteins at microirradiated sites would indicate an unspecific trapping of the factors at those sites.

GM02063 cells were microirradiated with the P.A.L.M. system at two distant nuclear sites and fixed at various times after microirradiation. Double immunofluorescence staining was performed with the polyclonal antibody against Rad51 used throughout this work and a second monoclonal antibody against the tested protein. The tested proteins were RNA Polymerase II (RNA Pol II), negative cofactor 2 (NC2), an inhibitor of RNA Pol II (Meisterernst and Roeder 1991) and the pre-mRNA splicing factor SC35 (Spector 1996).

In untreated cells RNA Pol II and NC2 are distributed in small foci throughout the whole nucleus excluding the nucleoli (see Figure 3.9 and von Mikecz (2000) for RNA Pol II and Figure 3.11 A and B for NC2). SC35 locates in a speckled nuclear distribution pattern excluding the nucleoli (Spector 1996). Similar staining patterns were found in microirradiated cells (Figure 3.10, Figure 3.11 C-F, Figure 3.12). In particular cells, which had Rad51 accumulations (marking the irradiated sites) did not have accumulations of RNA Pol II, NC2, or SC35 at the sites of Rad51 accumulations. Occasionally, small foci of transcription or splicing factors were observed in the regions of the Rad51 accumulations (Figure 3.10 C, Figure 3.12 B). The sizes and intensities of these foci, however, did not exceed those of other foci in the staining pattern. From these results it can be concluded that proteins not involved in DNA repair do not accumulate at microirradiated sites, and that Rad51 accumulation at microirradiated sites is a specific reaction to DNA damage.

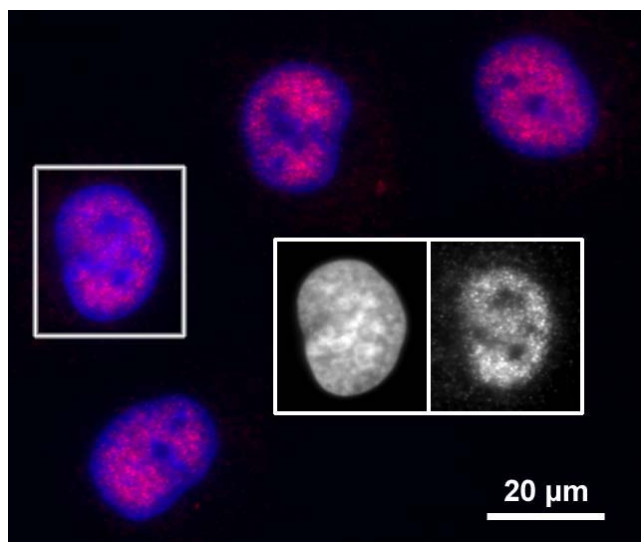


Figure 3.9: RNA-Pol II immunostaining of unirradiated GM02063 cells

Widefield fluorescence image. blue: DAPI nuclear counterstain, red: RNA Pol II. The gray insets show separate color channels of the marked cell (left: DAPI, right: RNA Pol II).

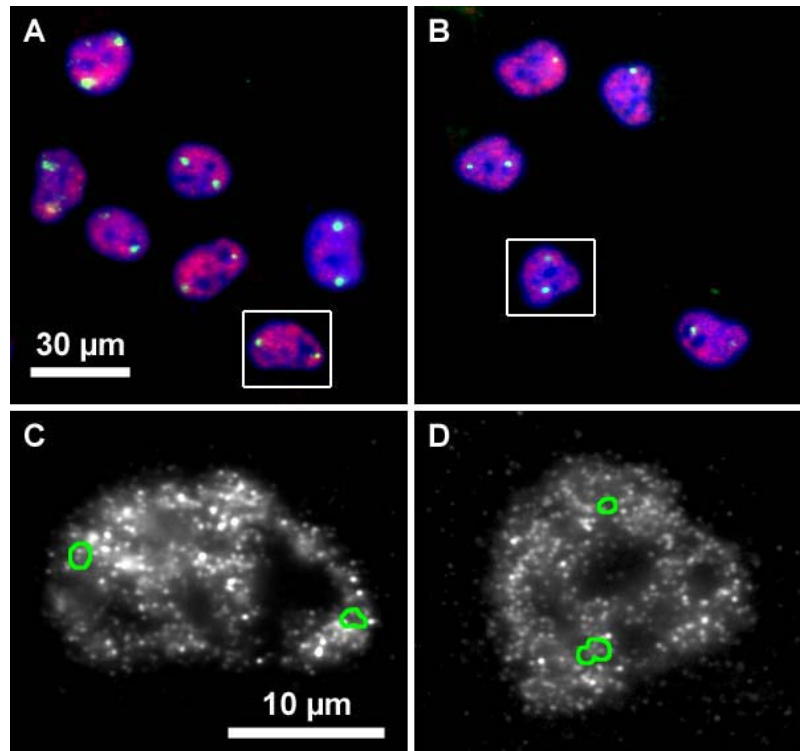


Figure 3.10: Rad51 and RNA-Pol II immunostaining of microirradiated GM02063 cells

Widefield fluorescence images.

(A) Cells fixed 1h after irradiation

(B) Cells fixed 4h after irradiation

blue: DAPI nuclear counterstain, green: Rad51, red: RNA Pol II

(C) and (D) contain enlarged images of the RNA Pol II signals of the cells marked in A and B, respectively. The positions of the Rad51 accumulations are shown by the green outlines.

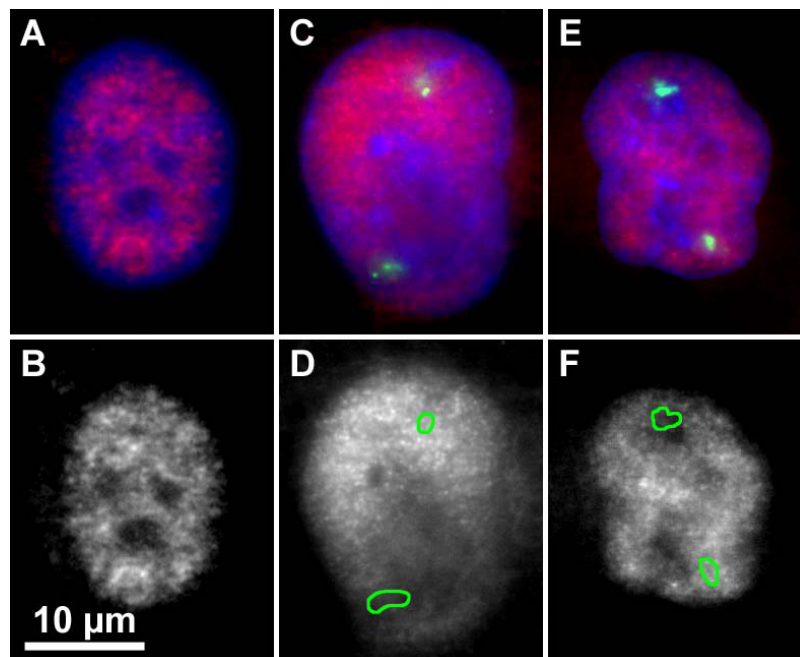


Figure 3.11: Rad51 and NC2 immunostaining of unirradiated and microirradiated GM02063 cells

Widefield fluorescence images.

(A), (B) unirradiated cell (NC2 staining only)

(C), (D) Cell fixed 1h after irradiation

(E), (F) Cell fixed 4h after irradiation

(A), (C), (E): blue: DAPI, green: Rad51, red NC2

(B), (D), (F): NC2 immunostaining. Rad51 accumulations are indicated by the green outlines.

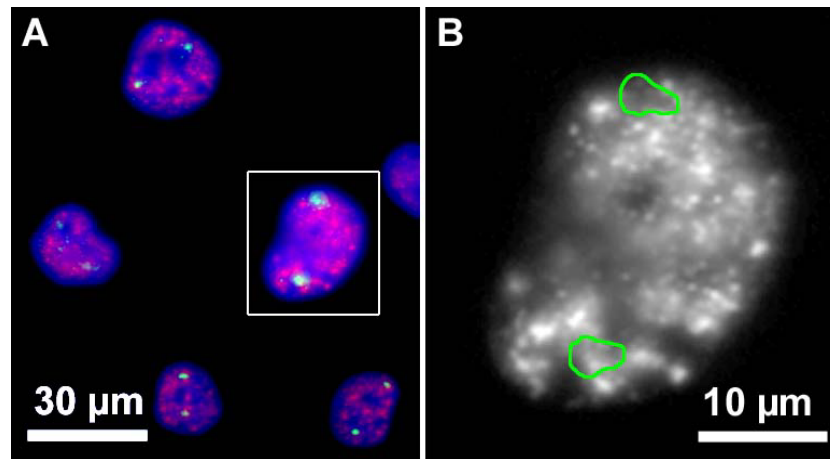


Figure 3.12: Rad51 and SC35 immunostaining of microirradiated GM02063 cells
Widefield fluorescence images.

(A) Overview image of cells fixed approximately 40 minutes after microirradiation. blue: DAPI, green: Rad51, red: SC35

(B) Enlarged image of the SC35 signal of the cell marked in (A). Rad51 accumulations are indicated by the green outlines.

3.1.4 Mre11 accumulates at laser-UVA-microirradiated nuclear sites and colocalizes with Rad51 accumulations

Mre11 is a member of a protein complex (MRN-complex), which in mammalian cells comprises the proteins Mre11, Rad50 and NBS1 (Carney *et al.* 1998; Varon *et al.* 1998). Mre11 acts in DSB-repair by both NHEJ and HRR in yeast cells, and is believed to play a similar role in mammalian cells (Haber 1998). The protein forms nuclear foci in mammalian cells after the induction of DSBs (Maser *et al.* 1997). Paull *et al.* (2000) found that Rad50 and NBS1, the other components of the MRN-complex, accumulated at laser-UVA-microirradiated sites in nuclei of human breast tumor cells. Another study (Nelms *et al.* 1998) reported that after partial volume irradiation with ultrasoft X-rays Mre11 located to the irradiated sites in human fibroblasts, but did not find distinct Rad51 signals at these sites.

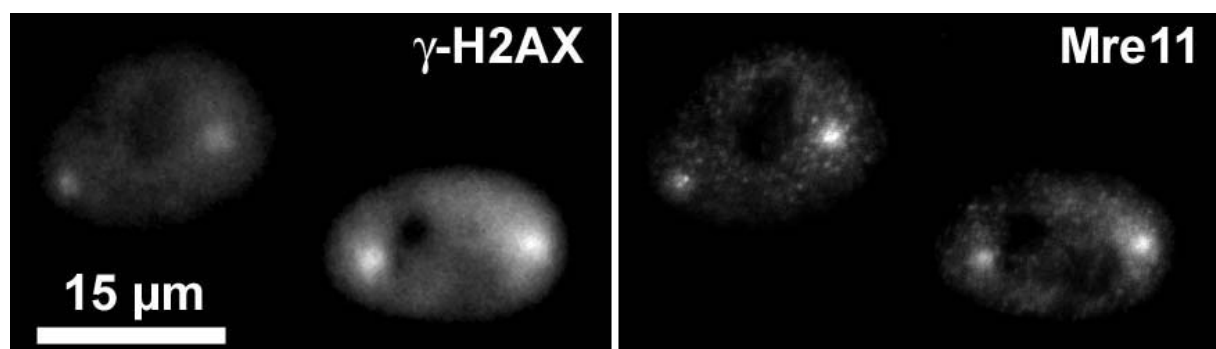


Figure 3.13: γ -H2AX and Mre11 immunostaining of microirradiated primary human fibroblasts 2.5 to 5 min after irradiation

To verify that the accumulation of Mre11 at sites of DNA damage is reproducible with the laser-UVA-microirradiation system, primary fibroblasts were sensitized with the BrdU/Hoechst system, irradiated with 30 nJ per site ($\lambda = 364$ nm, 2 sites per cell) and fixed 0 to 15 minutes after irradiation. Unbound nucleoplasmic Mre11 was removed

by an extended detergent treatment (protocol 2.2.6, Figure 3.13), and the cells were immunostained for Mre11 and phosphorylated histone H2AX (γ -H2AX). Histone H2AX is phosphorylated in megabase chromatin domains at sites of DSBs as early as three minutes after irradiation (Rogakou *et al.* 1999), and was used as a marker for the sites of irradiation. In these experiments spots of γ -H2AX were found in all microirradiated cells. Nuclear accumulations of Mre11 were seen in the cells already in the time interval from 0 to 2.5 min after irradiation, and the accumulations colocalized with areas of γ -H2AX (Figure 3.13). The accumulations were present in the majority of the irradiated cells ($n = 55$) and persisted over the entire observed time range.

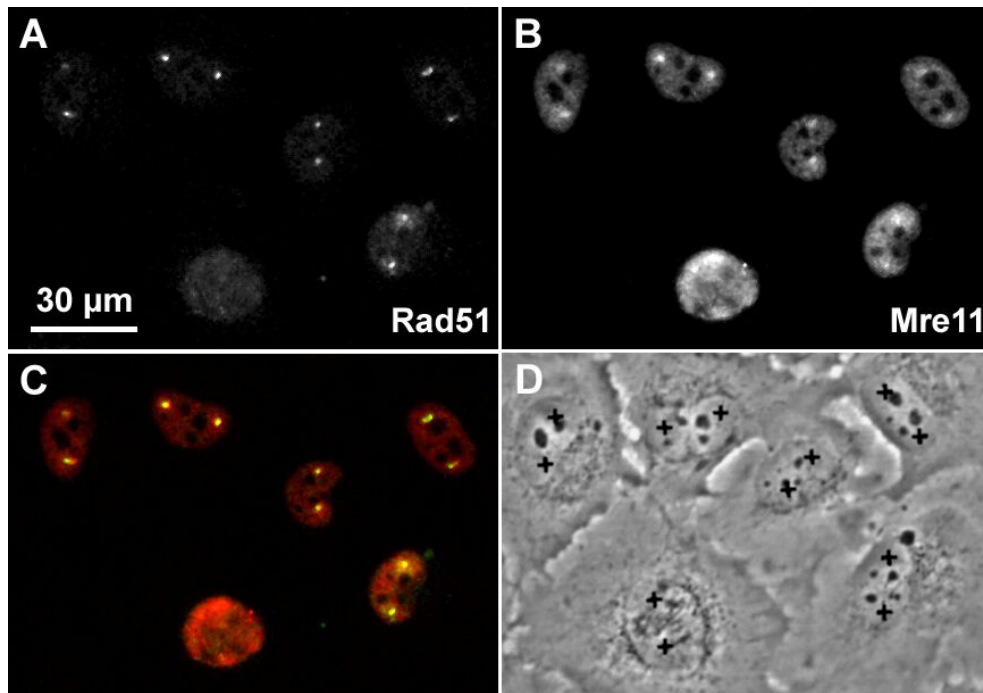


Figure 3.14: Rad51 and Mre11 immunostaining of microirradiated GM02063 cells fixed 30-40 min after irradiation

(A) Widefield fluorescence image of the Rad51 staining

(B) Widefield fluorescence image of the Mre11 staining

(C) Overlay of (A) and (B) with Rad51 false colored green and Mre11 colored red. The yellow spots are sites, where a Rad51 accumulation and an Mre11 accumulation colocalize.

(D) Phase contrast image recorded shortly before microirradiation. The black crosses denote sites marked for microirradiation. As the cells moved over the coverslip after microirradiation, the locations of individual cells differ slightly from the locations in (A)-(C).

As described in section 3.1.2, in contrast to the result of Nelms *et al.* (1998) Rad51 accumulates at laser-UVA-microirradiated nuclear sites in human primary fibroblasts and human cell lines. To test the spatial relation of Mre11 and Rad51 and to examine the relative dynamics of the two proteins, GM02063 cells and primary fibroblasts were microirradiated, fixed 0 - 40 min after irradiation and immunostained for Rad51 and Mre11 (the experiment was described in section 3.1.3). Widefield fluorescence images (Figure 3.14) were evaluated for the presence of Rad51 accumulations and Mre11 accumulations in microirradiated cells (Figure 3.15, Figure 3.16). For both cell types a large and constant fraction of 70% - 90% of the irradiated cells contained Mre11 accumulations over the entire observation period, with the exception of the first time point (0 - 5 min) for GM02063 cells, where the fraction of cells with Mre11 accumulations is lower. However, the error of this value is very large. The fraction of cells containing Rad51 accumulations has a major increase 10 -

20 min after irradiation in GM02063 cells and thereafter increases slightly to a final value of 70%. In primary fibroblasts the fraction of cells with Rad51 accumulations increases from 10% after 0 - 5 min to 40% after 20 - 30 min. In both cell types a considerable fraction of the irradiated cells contained Rad51 accumulations and Mre11 accumulations, which colocalized at the irradiated sites.

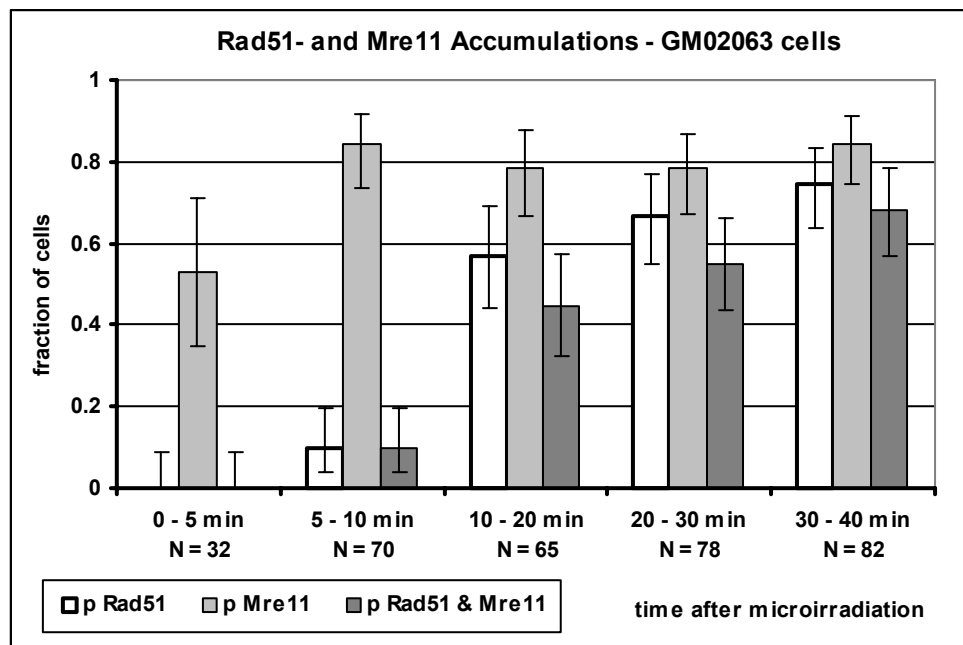


Figure 3.15: Bar plot of the fractions of GM02063 cell nuclei containing Rad51 accumulations and Mre11 accumulations after microirradiation

Bars in white, light gray and dark gray represent the fractions of all cells which contain Rad51 accumulations (p Rad51), all cells which contain Mre11 accumulations (p Mre11), and cells with Rad51 accumulations and Mre11 accumulations (p Rad51 & Mre11), respectively. Each column contains data from cells treated with BrdU/Hoechst, irradiated and fixed at the indicated time after irradiation. For each column the number of counted cells is displayed. Error bars show the 95% binomial confidence intervals.

Already 0 - 5 min after microirradiation 50% of the irradiated cell nuclei contain Mre11 accumulations. 5 - 10 min after microirradiation 80% of the irradiated nuclei contain Mre11 accumulations. This fraction remains constant over the entire observation period. In contrast, no Rad51 accumulations are present in nuclei 0 - 5 min after irradiation, and only 10% of the irradiated nuclei contain Rad51 accumulations 5 - 10 min after irradiation. This fraction jumps to almost 60% 10 - 20 min after irradiation and increases slightly thereafter. However, the confidence intervals are overlapping beginning from 10 min after irradiation. The fraction of cells containing Rad51 accumulations and Mre11 accumulations increases along with the fraction of cells containing Rad51 accumulations.

As Mre11 plays a role in DNA-DSB repair by both HRR and NHEJ, it was expected, that the appearance of Mre11 accumulations and the appearance of Rad51 accumulations in irradiated cells are independent. To test this, the fourfold-point correlation of the two fractions was calculated (see section 2.4.2). Values of the fourfold-point correlation function for each time interval and the significances of these values are displayed in Table 3.2 for GM02063 cells and Table 3.3 for primary fibroblasts. For both cell types the fourfold-point correlation is not significantly different from zero with the exception of the time-interval from 30 - 40 min after irradiation of GM02063 cells, where the correlation is significant ($p = 0.0012$). It is not clear, whether this value indicates a trend towards a higher correlation at later times after irradiation or whether it is simply a statistical outlier.

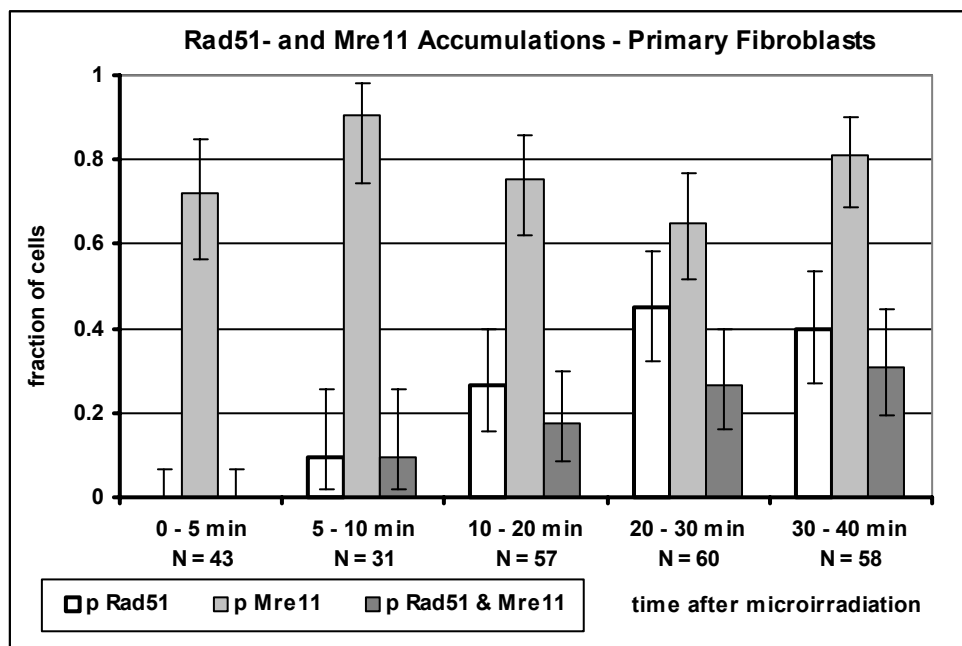


Figure 3.16: Bar plot of the fractions of primary fibroblast cell nuclei containing Rad51 accumulations and Mre11 accumulations after microirradiation

For explanation of the data and the error bars see the legend of Figure 3.15. 0 - 5 min after microirradiation 70% of the irradiated cell nuclei contain Mre11 accumulations. This fraction remains constant over the entire observation period, as all fluctuations lie within the 95% confidence intervals. No Rad51 accumulations are present in nuclei 0 - 5 min after irradiation, and only 10% of the irradiated nuclei contain Rad51 accumulations 5 - 10 min after irradiation. This fraction rises to 30% 10 - 20 min after irradiation and later increases to 40%. However, the confidence intervals are overlapping beginning from 10 min after irradiation. The fraction of cells containing Rad51 accumulations and Mre11 accumulations increases along with the fraction of cells containing Rad51 accumulations.

time after irradiation	0 - 5 min	5 - 10 min	10 - 20 min	20 - 30 min	30 - 40 min
Fourfold-point correlation	-	0.144	-0.002	0.154	0.357
p	-	0.23	0.99	0.17	0.0012

Table 3.2: Fourfold-point correlation of Rad51 accumulation and Mre11 accumulation in microirradiated GM02063 cell nuclei

The fourfold-point correlation cannot be calculated for the time from 0 to 5 minutes after microirradiation, as no cell nuclei contain Rad51 accumulations at this time. For the time from 5 to 30 minutes after microirradiation there is no significant correlation between Rad51 accumulations and Mre11 accumulations in irradiated nuclei ($p > 0.05$). In the time interval 30 - 40 minutes after irradiation the correlation is significant.

time after irradiation	0 - 5 min	5 - 10 min	10 - 20 min	20 - 30 min	30 - 40 min
Fourfold-point correlation	-	0.107	-0.122	-0.109	-0.057
p	-	0.55	0.36	0.40	0.66

Table 3.3: Fourfold-point correlation of Rad51 accumulation and Mre11 accumulation in microirradiated primary fibroblast cell nuclei

The fourfold-point correlation cannot be calculated for the time from 0 to 5 minutes after microirradiation, as no cell nuclei contain Rad51 accumulations at this time. For the time from 5 to 40 minutes after microirradiation there is no significant correlation between Rad51 accumulations and Mre11 accumulations in irradiated nuclei ($p > 0.05$).

3.1.5 Accumulation of other DNA-repair related proteins after laser-UVA-microirradiation

The laser-UVA-microirradiation method was used to test, whether other DNA-repair proteins accumulate at microirradiated sites. To mark the microirradiated sites immunostaining for the tested proteins were combined with immunostaining for Rad51 or γ -H2AX.

The DNA dependent protein kinase (DNA-PK) plays a crucial role in the repair of DSBs by NHEJ. It consists of the DNA-PK catalytic subunit (DNA-PKcs) and a heterodimer formed by the proteins Ku70 and Ku80. As the NHEJ pathway is a major pathway for DSB repair in mammalian cells, it could be expected, that the Ku proteins accumulate at microirradiated sites in a large fraction of microirradiated cells. Primary fibroblasts were sensitized with BrdU/Hoechst, microirradiated with 30 nJ or 100 nJ per site ($\lambda = 364$ nm, 2 sites per cell) and fixed after 0 to 40 min. Cells were immunostained for γ -H2AX and the Ku70/80 heterodimer. In fluorescence images only 15 of 146 irradiated cells contained nuclear accumulations of Ku70/80 (Figure 3.17). Most of the accumulations were faint. It can, however be excluded that the identified accumulations resulted from a bleedthrough of the γ -H2AX-signal to the fluorescence channel of the Ku70/80 staining, because other cells with equally bright γ -H2AX accumulations did not show any Ku70/80 accumulations at all.

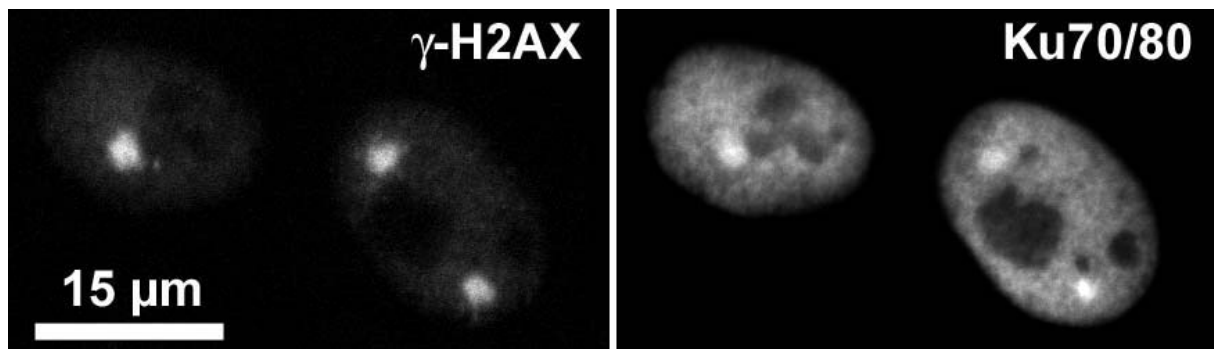


Figure 3.17: γ -H2AX and Ku70/80 immunostaining of microirradiated primary human fibroblasts 10 to 15 min after irradiation

The result that only few Ku70/80 accumulations were found at microirradiated sites is consistent with the report of Mirzoeva and Petrini (2001), who did not find a notable colocalization of Mre11 and Ku70 after gamma irradiation. There is, however, the possibility that more Ku70/80 accumulations are present, but are hidden in the strong background of nucleoplasmic Ku70/80.

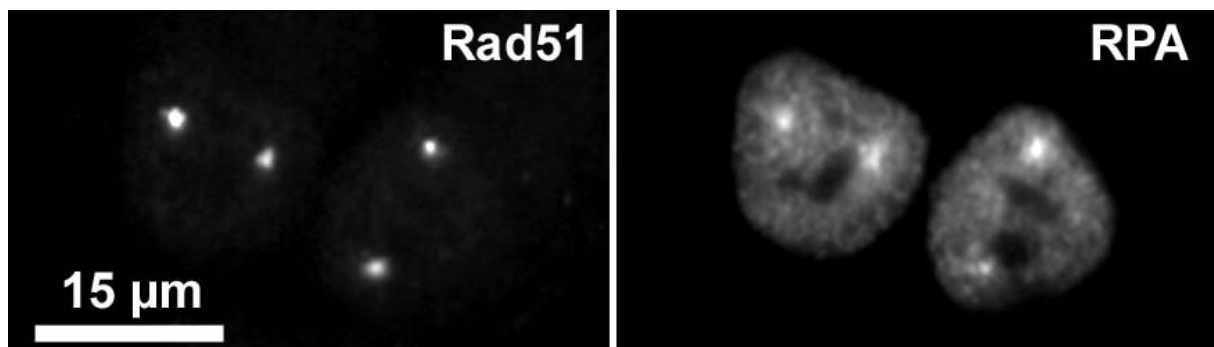


Figure 3.18: Rad51 and RPA immunostaining of microirradiated GM02063 cells 30 min after irradiation

RPA stimulates Rad51-mediated homologous strand exchange. RPA and Rad51 interact and the two proteins colocalize in gamma-irradiated mammalian cells (Golub *et al.* 1998). Therefore a colocalization of RPA and Rad51 after microirradiation was expected. In a test experiment BrdU/Hoechst sensitized cells were microirradiated with 8 to 960 nJ per site ($\lambda = 337$ nm, 2 sites per cell) and fixed 0 to 50 min after irradiation. Surprisingly, only cells irradiated with 960 nJ per site showed nuclear RPA accumulations, which colocalize with Rad51 accumulations (Figure 3.18), although Rad51 accumulations were clearly seen after irradiation with 40 nJ per site.

3.1.6 The nuclear distribution of PML after microirradiation

PML is crucial for multiple apoptotic pathways that lead to cell death after DNA damage (Wang *et al.* 1998; Guo *et al.* 2000), and PML overexpression induces apoptosis in mammalian cells (Quignon *et al.* 1998). Therefore, it was assumed that the induction of DNA damage could provoke changes in the nuclear distribution of PML with respect to DNA-repair proteins. To test this assumption GM02063 cells were sensitized with BrdU/Hoechst, microirradiated with 80 nJ per site ($\lambda = 337$ nm, 2 sites per cell), fixed after 1 h, 4 h, 8 h, 24 h and 48 h and immunostained for Rad51 and PML. Widefield fluorescence images of the irradiated regions were scored for the colocalization of Rad51 accumulations with PML bodies. Only 0 to 1 colocalization was found after 1 to 8 hours. However, after 24 hours five of the 20 Rad51 accumulations colocalized with a PML body (Table 3.4, Figure 3.19).

The result indicates that PML bodies associate with damaged sites one day after irradiation, but is not significant due to the low number of counted cells. Further experiments are indicated to follow this track.

time after microirradiation	1 h	4 h	8 h	24 h	48 h
number of Rad51 accumulations	42	30	29	20	6
number of Rad51 accumulations colocalizing with PML bodies	1	1	0	5	1
%age of Rad51 accumulations colocalizing with PML bodies	2%	3%	0%	25%	17%

Table 3.4: Time dependent degree of colocalization of Rad51 accumulations with PML bodies after microirradiation

After 24 hours the degree of colocalization between Rad51 accumulations and PML bodies increases.

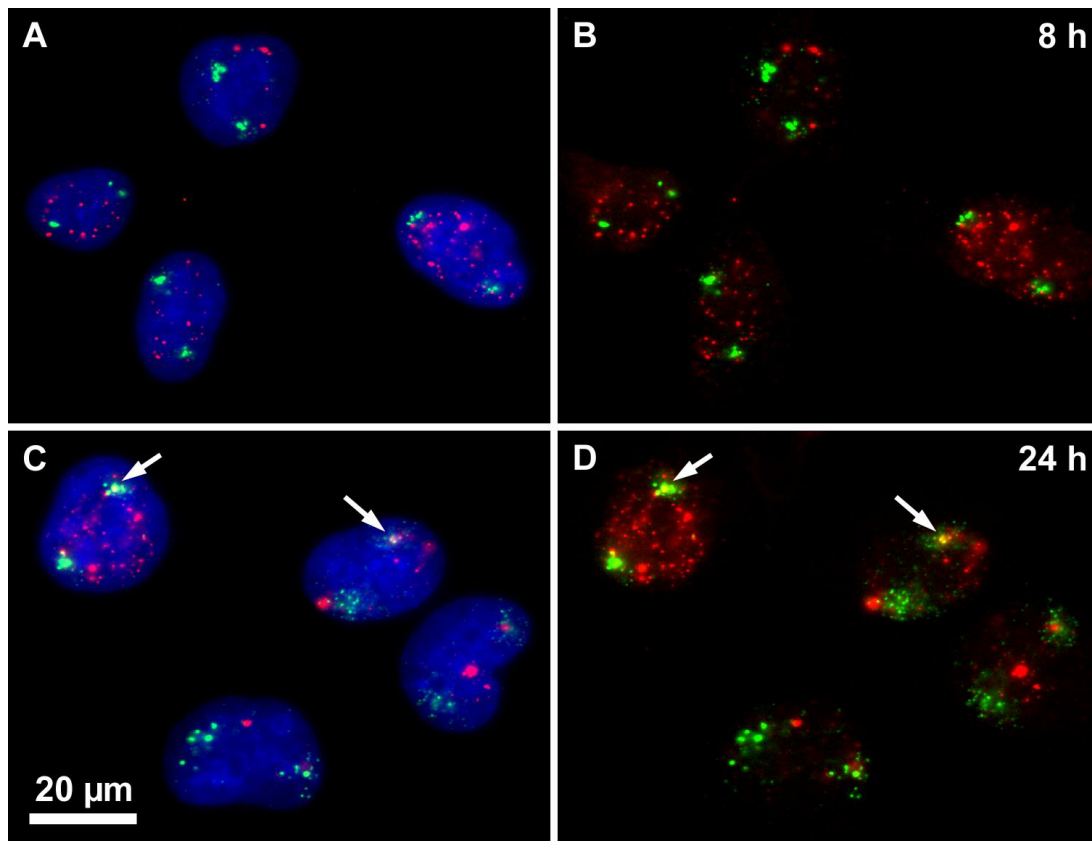


Figure 3.19: Localization of Rad51 and PML 8 and 24 hours after microirradiation

(A), (B): Cells fixed 8 hours after microirradiation

(C), (D): Cells fixed 24 hours after microirradiation

(A) and (C) show DAPI nuclear counterstain (blue), Rad51 immunostaining (green) and PML immunostaining (red). (B) and (D) show only the immunostaining signals

8 hours after microirradiation PML bodies are still separate from Rad51 accumulations. 24 hours after microirradiation two Rad51 accumulations (arrows) colocalize with PML bodies.

3.1.7 The fraction of cells with focal Rad51 nuclear staining remains unchanged after microirradiation with 30 nJ

The significance of the Rad51 foci in S-Phase cells (Figure 3.4) is not clear at present. It is possible that these foci serve as storage sites, and that upon DNA-damage Rad51 relocates from these sites to sites of ongoing homologous recombination repair. In this case it could be expected that the fraction of cells containing Rad51 foci decreases after microirradiation along with an increase of the fraction of cells with Rad51 accumulations. Alternatively, the number or the intensity of Rad51 foci in individual irradiated cells could decrease. These parameters are more difficult to test than the fraction of cells containing Rad51 accumulations and ultimately require live cell experiments.

To test the assumption that the fraction of cells containing Rad51 foci decreases after microirradiation, time series experiments were performed, in which GM02063 cells or primary fibroblasts were sensitized with the BrdU/Hoechst system, microirradiated at two nuclear sites with the LSM 510 ($\lambda = 364$ nm, estimated energy 30 nJ per site) and fixed 0 to 40 minutes after microirradiation. Control cells were not sensitized and not irradiated. The cells were immunostained for Rad51 and Mre11, and the fractions of cell nuclei containing Rad51 foci, Rad51 accumulations, both Rad51 foci and Rad51 accumulations or no Rad51 staining were counted. (The

Mre11-staining was performed to compare the dynamics of the accumulation of Rad51 and Mre11 at microirradiated sites. This comparison was presented in section 3.1.3.) The experiment was performed twice for each cell type. The combined results from both experiments are displayed in Figure 3.20 and Figure 3.21.

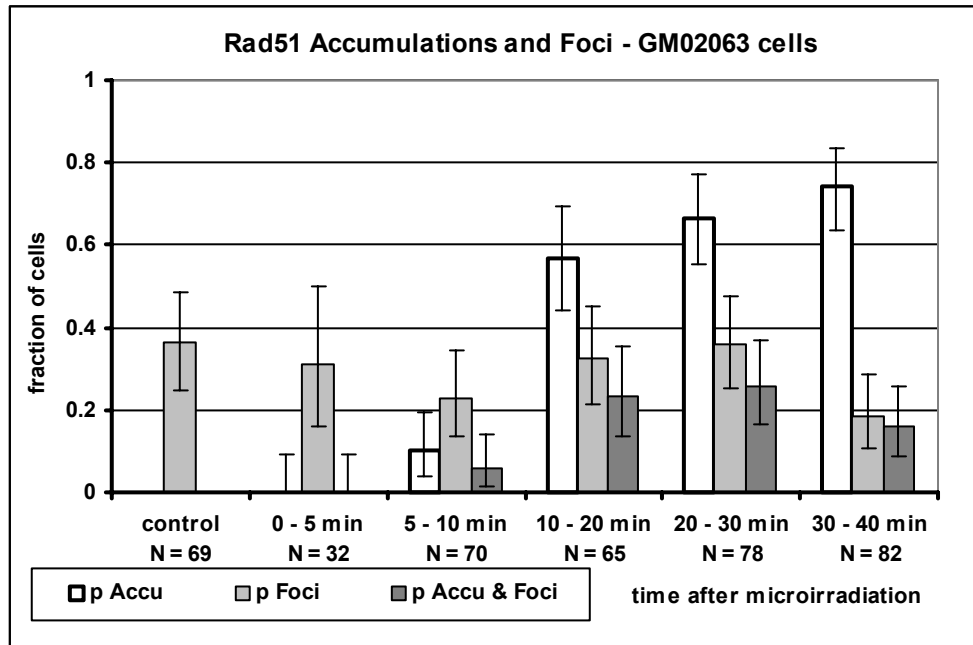


Figure 3.20: Bar plot of the fractions of GM02063 cell nuclei containing Rad51 accumulations and Rad51 foci after microirradiation

Bars in white, light gray and dark gray represent the fractions of all cells which contain Rad51 accumulations (p Accu), all cells which contain Rad51 foci (p Foci), and cells with Rad51 foci and Rad51 accumulations (p Accu & Foci), respectively. The data in the first column is taken from control cells, which were not treated with BrdU/Hoechst and not irradiated. All other columns contain data from cells treated with BrdU/Hoechst, irradiated and fixed at the indicated time after irradiation. For each column the number of counted cells is displayed. Error bars show the 95% binomial confidence intervals.

The fraction of cells containing Rad51 accumulations rises to more than 70% at 30 - 40 min after microirradiation. However, the fraction of cells with Rad51 foci remains constant, as can be seen from the fact that the respective 95% confidence intervals for all data points overlap. 10 - 40 minutes after microirradiation most nuclei with Rad51 foci also contain Rad51 accumulations at microirradiated sites.

For both cell types the fraction of irradiated cell nuclei with Rad51 accumulations increased starting from 5 - 10 minutes after microirradiation. At the same time, the fraction of nuclei with Rad51 foci remained constant, i.e. the 95% confidence intervals of all data points were overlapping for each cell type. This result argues against a complete redistribution of Rad51 from nuclear foci to damaged sites. In fact, when the fraction of nuclei with Rad51 accumulations became significant 10 minutes after microirradiation and later, most nuclei with Rad51 foci also contained Rad51 accumulations.

Note that in both GM02063 cells and primary fibroblasts, which were fixed at least 20 minutes after microirradiation, the fraction of nuclei containing Rad51 accumulations exceeded the fraction of control nuclei, which contained Rad51 foci. This indicates that Rad51 accumulations did not only appear in nuclei which contained Rad51 foci at the time of irradiation but also in nuclei which did not contain Rad51 foci. One reason for this could be that in those nuclei Rad51 was distributed diffusely over the nucleus, e.g. G2 nuclei. Such a distribution would be difficult to

detect by immunofluorescence. Alternatively, Rad51 could be newly synthesized in nuclei previously void of Rad51.

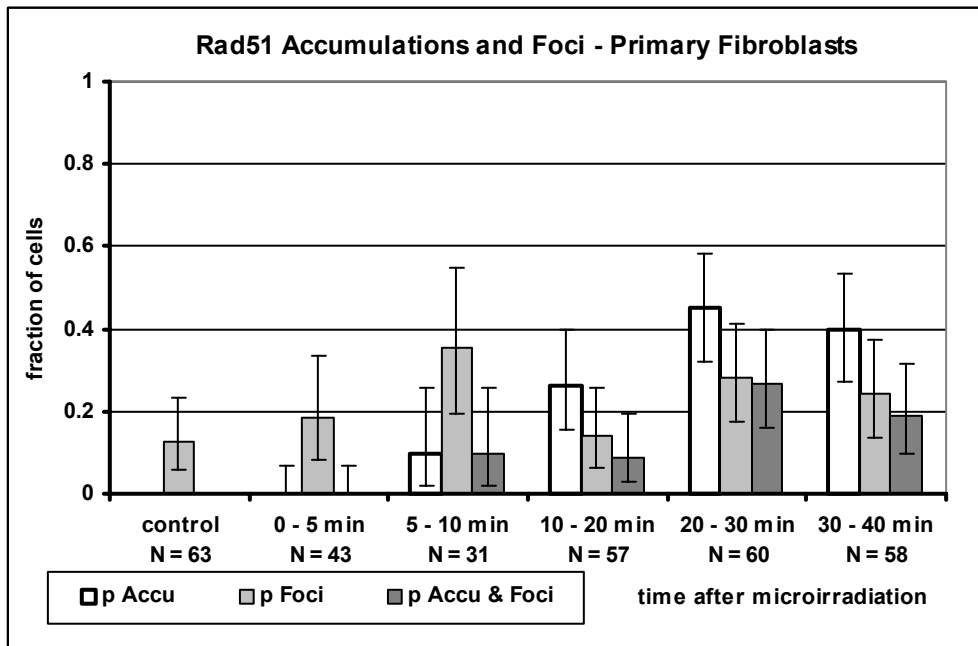


Figure 3.21: Bar plot of the fractions of primary fibroblast cell nuclei containing Rad51 accumulations and Rad51 foci after microirradiation

For explanation of the data and the error bars see the legend of Figure 3.20. The fraction of cell nuclei with Rad51 accumulations rises from 0 to 40%, whereas the fraction of nuclei with Rad51 foci remains constant, as the 95% confidence intervals for all data points overlap. 10-40 minutes after microirradiation most nuclei with Rad51 foci also contain Rad51 accumulations at microirradiated sites.

3.1.8 Chromosome territory arrangements during DSB repair

Repair of DNA double-strand breaks (DSBs) by gene conversion requires the formation of recombination repair complexes containing a joint molecule between a damaged and a homologous intact DNA strand. In cases where DSBs are produced within a single copy DNA segment, the intact, homologous segment for this complex must be provided by the homologous parental chromosome or by a sister chromatid. Homologous CTs are typically separated in nuclei of cultured mammalian cells by chromatin from non-homologous CTs. Large scale, postirradiation chromatin movements are therefore necessary to establish spatial proximity between a broken DNA strand and the intact homologous counterpart of the parental homologue. To test this possibility, GM02063 cells were sensitized with the BrdU/Hoechst system and laser-UVA-microirradiated. With multiple microirradiation exposures letter-like patterns of damaged chromatin were produced in single nuclei ($\lambda = 337$ nm, total estimated energy for the whole pattern: 1200 nJ), and the cells were fixed after 1 to 48 hours. The patterns were visualized by immunostaining for Rad51, which is recruited to damaged sites undergoing DSB repair by gene conversion (section 3.1.2). In nuclei fixed after postirradiation periods of up to 8 hours the letter-like patterns remained “readable” (Figure 2.1). This finding excludes large-scale rearrangements of CTs in the observed cells.

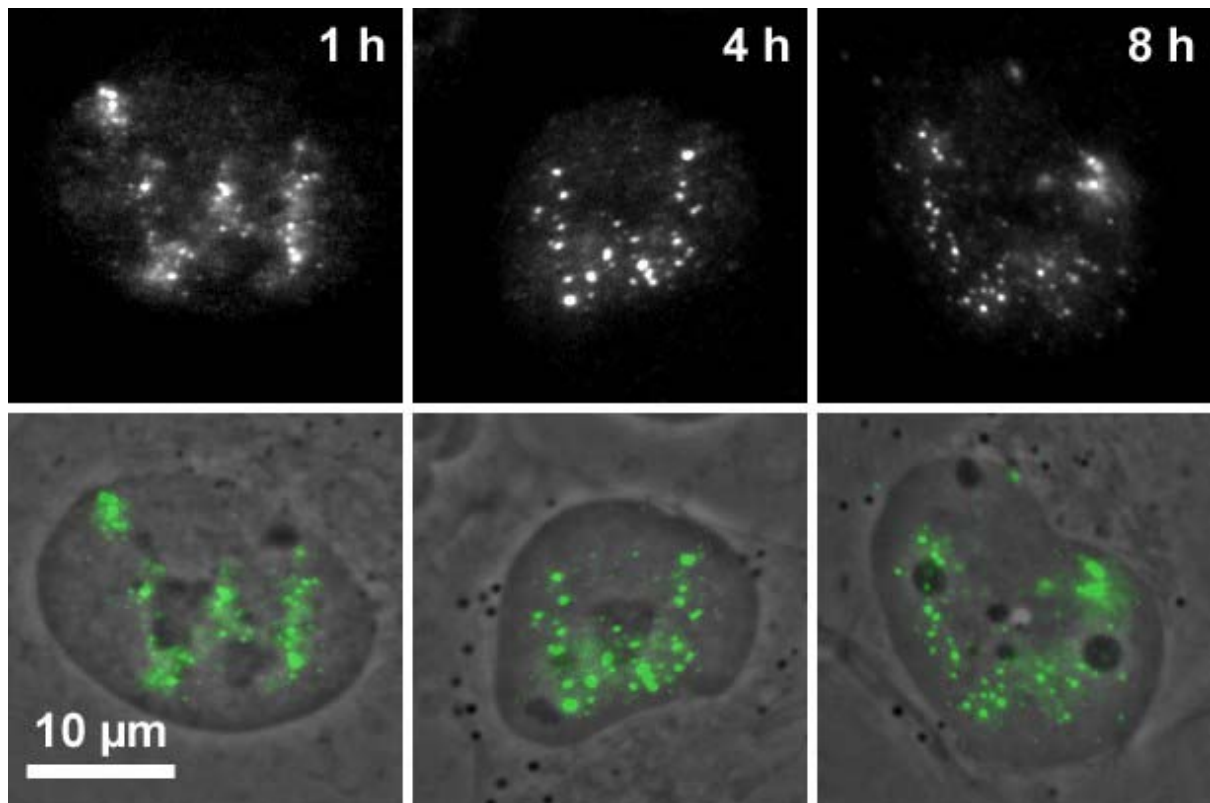


Figure 3.22: Stability of CT organization in interphase GM02063 cell nuclei during recombination repair of DSBs

The W-shaped patterns of Rad51 recruitment persist over 8 hours and show only local deformations.

3.1.9 Localization of Rad51 in unirradiated nuclei

The significance of the Rad51 foci which are present in undamaged cells during S-Phase (section 3.1.2, Figure 3.4) is not clear at present. To investigate, whether they are located in the interchromatin compartment (Cremer and Cremer 2001), staining of Rad51 and the nuclear DNA was examined by confocal microscopy.

3.1.9.1 Endogenous Rad51 foci

To visualize endogenous Rad51 in combination with nuclear DNA two preliminary experiments were performed. In one experiment GM02063 cells were immunostained for Rad51, and DNA was stained with propidium iodide (PI). As PI strongly stains RNA, PI staining was preceded by an RNase treatment to remove RNA. Staining with the DNA-dye DAPI, which only stains DNA and not RNA, was not possible, as DAPI-fluorescence is excited by wavelengths between 320 and 420 nm. These wavelengths were not available for examination by confocal microscopy in this experiment. Mid-nuclear light-optical sections show that Rad51 foci are located in areas of low PI staining, i.e. areas of low DNA density (Figure 3.23).

In a second experiment, HeLa cells stably expressing GFP tagged histone H2B (H2B-GFP) (Kanda *et al.* 1998) were fixed and immunostained for Rad51. As H2B-GFP is incorporated into nucleosomes like endogenous H2B, it serves as a nuclear counterstain. Rad51 was detected with the fluorochrome Cyanine 5 to avoid spectral overlap of the H2B-GFP and Rad51 immunostaining. Light-optical sections show Rad51-foci located at sites of low GFP intensity (Figure 3.24).

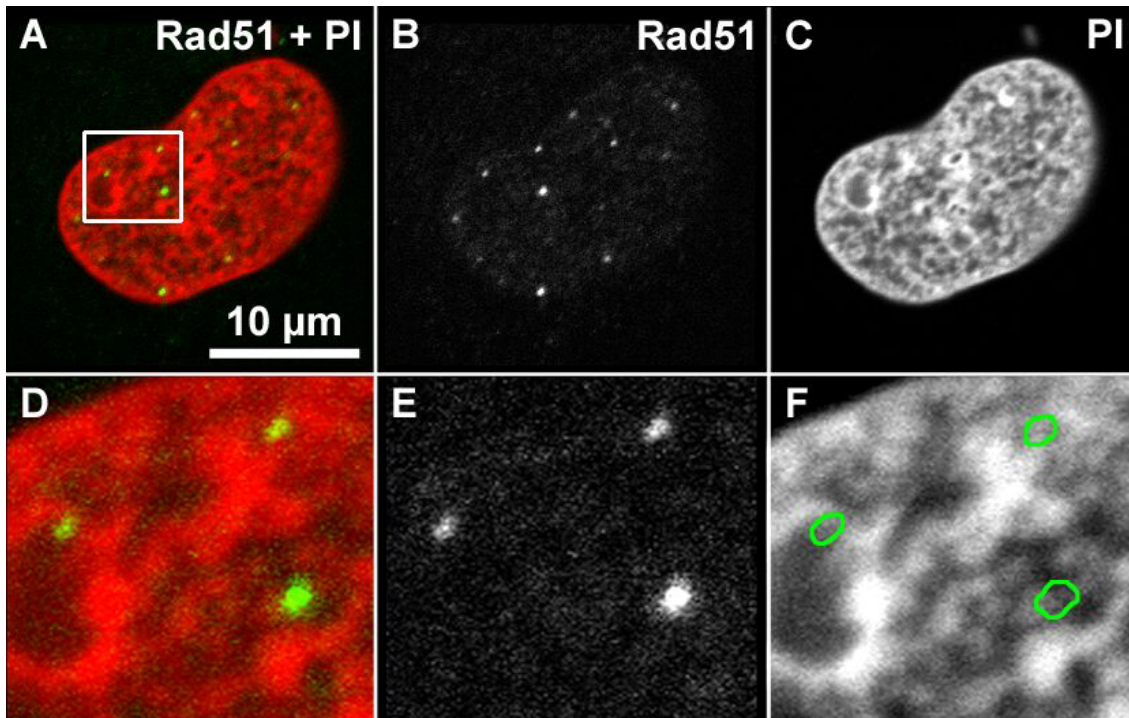


Figure 3.23: Light-optical section of a GM02063 cell showing Rad51 (green) and nuclear DNA (PI, red)

(D), (E) and (F) show an enlargement of the area outlined in (A). The position of the three Rad51 foci seen in (D) and (E) is indicated by the green outline in the PI image (F). The Rad51 foci are located in areas where PI staining is of low intensity.

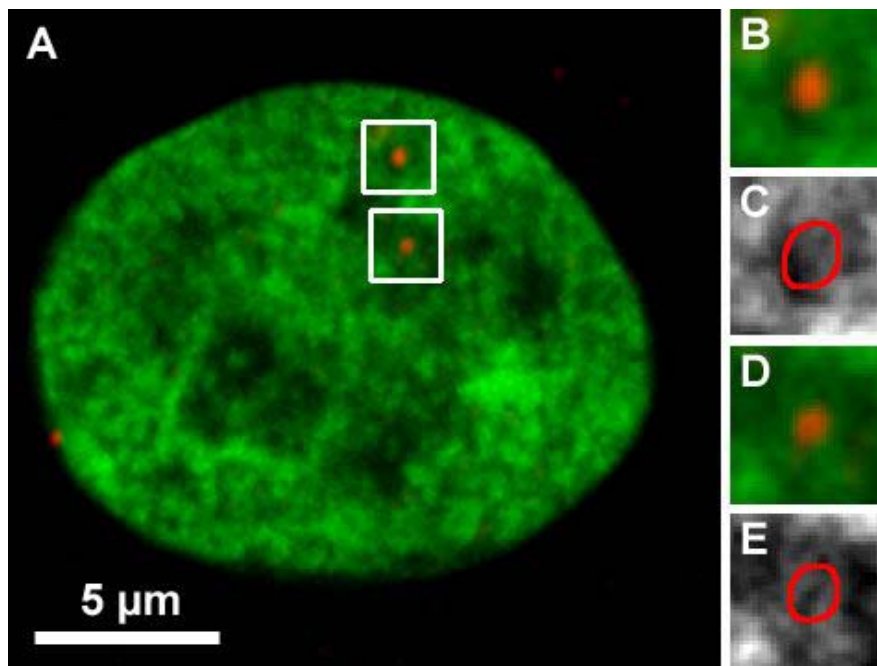


Figure 3.24: Light-optical section of a HeLa cell showing Rad51 foci (red) and nuclear DNA (H2B-GFP, green)

(B) - (E) show enlargements of the outlined areas in (A). The red outlines in (C) and (E) indicate the Rad51 foci in (B) and (D).

3.1.9.2 GFP-Rad51 filaments

To observe the localization and dynamics of Rad51 in living cells, GM02063 cells were transfected with the plasmid for a GFP-Rad51 construct kindly provided by Dr. Ryushin Mizuta (see protocol 2.1.6). The expressed GFP-Rad51 protein formed extended “filamental” nuclear structures similar to structures reported by Raderschall *et al.* (2002a) for overexpressed wildtype Rad51, which were substantially different from the distribution of endogenous Rad51. GFP-Rad51 therefore was not useable for *in-vivo* observation of the assembly of Rad51-accumulations after microirradiation.

Another network of filaments, namely filaments of *Xenopus* vimentin engineered to contain a nuclear localization signal (NLS-vimentin), had been described to mark an interchromatin compartment containing nuclear RNA, coiled bodies and PML bodies (Bridger *et al.* 1998; Reichenzeller *et al.* 2000). To test, whether GFP-Rad51 filaments marked the same compartment, GM02063 cells were transfected with GFP-Rad51. Four hours later the cells were transfected with NLS-vimentin. Cells were kept at 28°C, the optimal temperature for the assembly of the vimentin-filaments, fixed two hours later and immunostained for vimentin. Light-optical sections show the colocalization of GFP-Rad51 and NLS-vimentin (Figure 3.25).

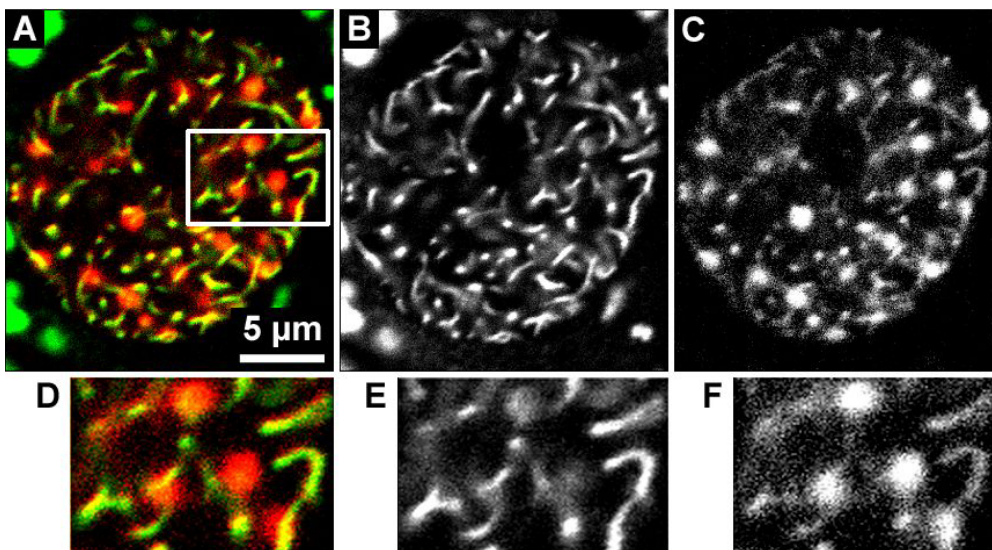


Figure 3.25: Light optical section of a GM02063 cell showing GFP-Rad51 filaments (green) and NLS-vimentin filaments (red).

(A): Combination of GFP-Rad51 and immunostaining for NLS-vimentin. (B) and (C) show only the GFP-Rad51 and NLS-vimentin signal, respectively. (D), (E), (F) show an enlarged view of the area outlined in (A). GFP-Rad51 filaments and NLS-vimentin filaments colocalize.

As a further test, whether GFP-Rad51 filaments mark an interchromatin compartment, GM02063 cells were transfected with GFP-Rad51, incubated for 24 hours and fixed. Nuclear DNA was stained with PI after removal of RNA by RNase treatment. In light optical sections Rad51 filaments were found in regions of low PI staining (Figure 3.26).

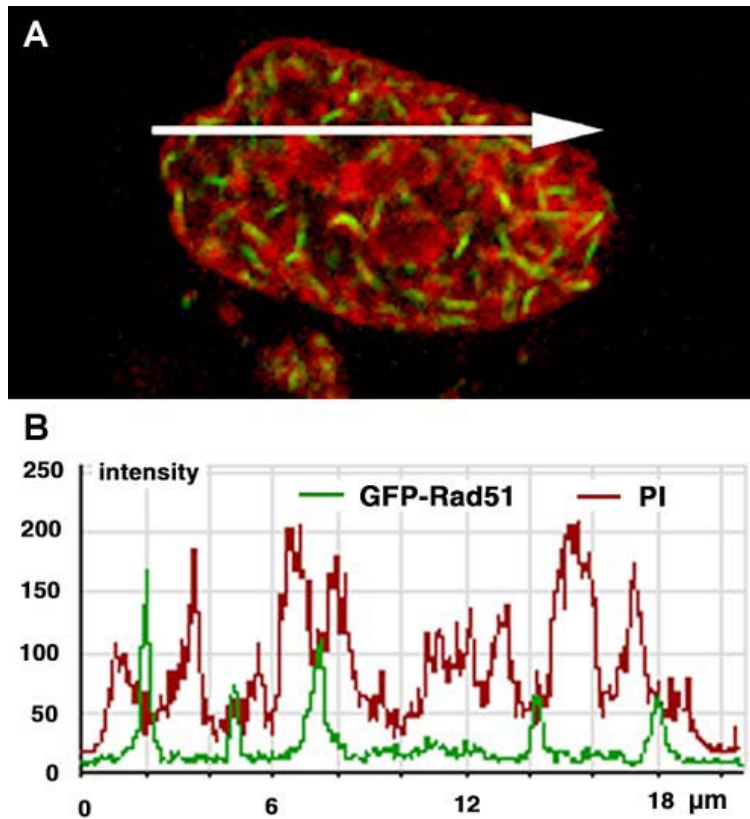


Figure 3.26: GFP-Rad51 filaments (green) and PI (red) in a GM02063 cell.

(A): Mid-nuclear light optical section. (B): Profile plots of the intensities of GFP-Rad51 and PI along the white arrow in (A). Peaks of the GFP-Rad51 signal (standing for points where the arrow crosses a filament) are located in valleys of the PI signal.

For the interpretation of the interchromatin compartment marked by GFP-Rad51 filaments it is important to know whether the GFP-Rad51 molecules are stably integrated into the filaments or whether they are rapidly diffusing. A diffusion of GFP-Rad51 molecules at a rate comparable with that of other nuclear proteins would indicate that the filaments reflect an intrinsic property of the nucleus. This property could either be a network of attachment sites for transient binding of proteins (Misteli 2001) or an exclusion of proteins from dense chromatin due to geometrical constraints. In case of a stable assembly of GFP-Rad51 molecules in filaments there would still be the possibility that the filaments enforce changes onto the nucleus by their own structural stability.

The dynamics of GFP-Rad51 was examined by fluorescence recovery after photobleaching (FRAP). 293T cells were transfected with GFP-Rad51. 24 hours later they were transferred to a living cell chamber and kept at 37°C on the stage of a confocal microscope (LSM 510). Subregions of nuclei with GFP-Rad51 filaments were bleached with the unattenuated 488 nm laser line of the microscope. The cells were observed up to 70 s after bleaching. No notable recovery of the GFP fluorescence was seen in the bleached area during this time (Figure 3.27 A), showing that no significant number of unbleached GFP-Rad51 molecules diffused into the space of bleached GFP-Rad51. When cytoplasmic GFP-Rad51 was bleached, the fluorescence largely recovered after 4.6 seconds (Figure 3.27 B), which is a time scale comparable to the recovery time of other nuclear proteins (Phair and Misteli 2000). This result shows that GFP-Rad51 filaments are comparably stable structures.

Another evidence for the stability of the GFP-Rad51 filaments was the observation of pairs of cell nuclei, whose networks of GFP-Rad51 filaments were connected, two days after the transfection of GFP-Rad51 to GM02063 cells (Figure 3.28). The connection of the filament networks in the two nuclei of a pair indicates that the nuclei resulted from the same mother nucleus and that the filaments were stably maintained throughout mitosis.

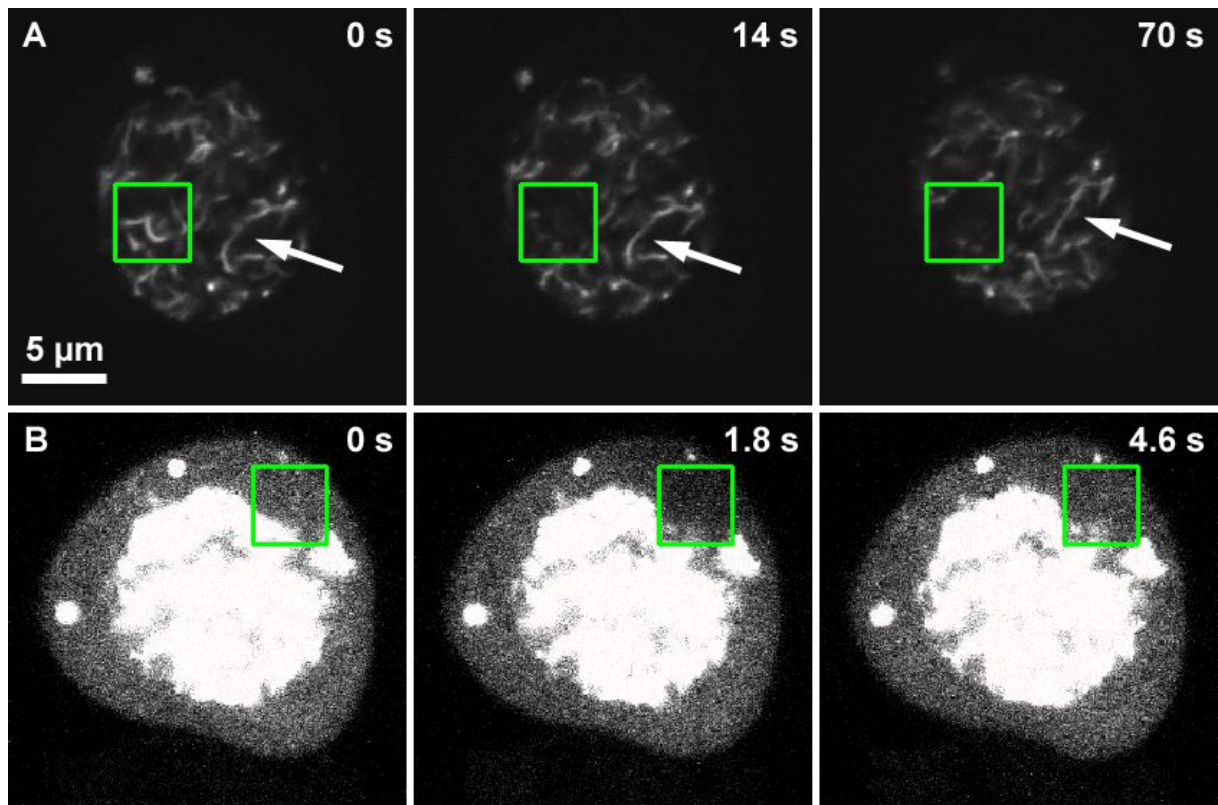


Figure 3.27: FRAP of nuclear GFP-Rad51 filaments.

(A): GFP fluorescence in a subregion (square) of a 293T cell nucleus containing GFP-Rad51 filaments is bleached and light optical sections are recorded every 14 seconds. GFP fluorescence in the bleached region is not recovered 70 seconds after bleaching. From the timepoint 14 s after bleaching to 70 s after bleaching the shape of some filaments (arrows) changes, arguing for deformations of the nucleus happening at this time scale. The appearance of fluorescing signals in the bleached regions is due to these deformations. (B): GFP fluorescence of bleached cytoplasmic GFP-Rad51 largely recovers 4.6 seconds after bleaching. Nuclear GFP-Rad51 filaments are strongly overexposed in these images. Their fluorescence is not recovered after 4.6 s in agreement with (A).

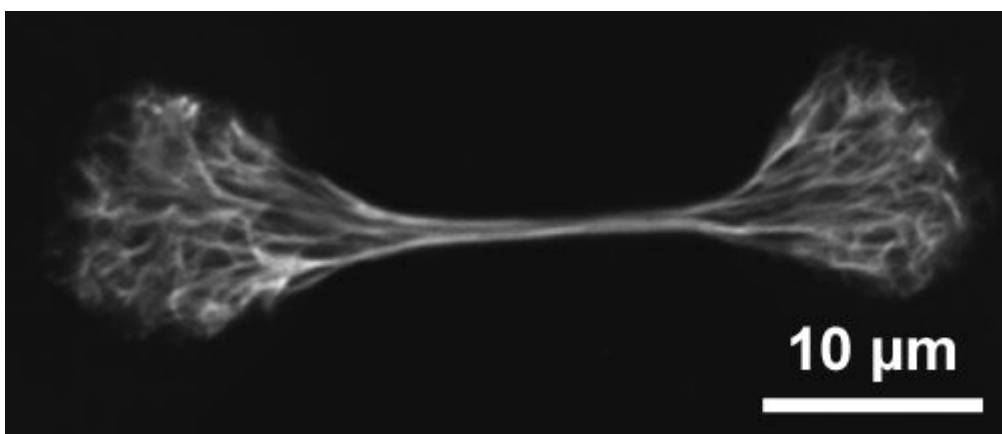


Figure 3.28: Light optical section of two GM02063 cell nuclei connected by GFP-Rad51 filaments two days after transfection of GFP-Rad51

3.2 Chromosome territory dynamics studied in living cells by photobleaching of GFP-tagged chromatin (H2B-GFP)

The long term immobility of Rad51 foci recruited to damaged nuclear sites (section 3.1.7) suggested that chromosome territory (CT) arrangements in damaged cells do not change at least during a period of 8 hours post microirradiation time. This raises the question, whether undamaged cells retain their large-scale CT arrangements during interphase, and if so, whether this results in the preservation of CT arrangements in subsequent cell cycles. To examine the dynamics of CTs in living cells, a HeLa cell line, which stably expresses histone H2B-GFP was used (Kanda *et al.* 1998). In these cells GFP plays the role of a counterstain (see Figure 3.24). Employing laser-photobleaching (488 nm) of GFP, the unbleached chromatin remained as selectively marked region. Unbleached regions could be followed by confocal microscopy up to several hours in accordance with the observation that the exchange between bleached and unbleached H2B-GFP occurs with $t_{1/2} \sim 130$ min for about 40% and with $t_{1/2} > 510$ min for about 53% of H2B-GFP (Kimura and Cook 2001).

3.2.1 Setup of a 4D live cell imaging system at an LSM 410

For 4D-imaging (3D + time) of living mammalian cells over extended times both the demands for cell viability and for microscopy have to be met. The cells should be kept on the microscope stage under sterile conditions at a temperature of 37°C and at a pH of 7.4. They have to be supplied with fresh cell culture medium. The microscope should allow to automatically record time series of 3D image stacks with stable imaging conditions.

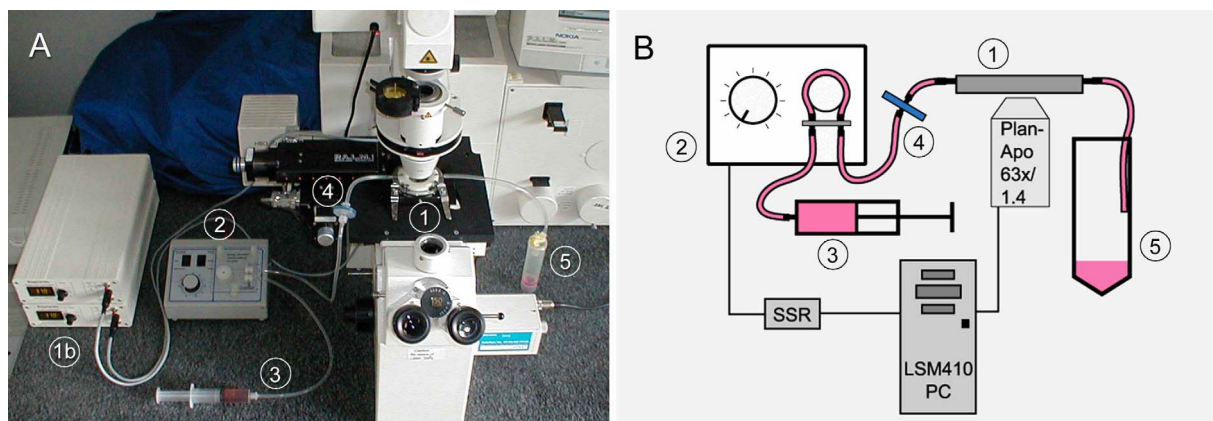


Figure 3.29: Experimental setup (A) and scheme (B) of the live cell imaging system.

The system consists of a Biopetechs FCS2 live cell chamber (1), temperature control units for chamber and objective-heater (1b), flexible tube pump (2) connected to the control PC via a solid state relay (SSR), syringe for supply of fresh medium (3), disposable syringe filter (4), waste container (5).

A system, which meets these conditions, was established at the Zeiss LSM 410 confocal microscope in Munich (Figure 3.29). The cells were kept in a temperature controlled closed live cell chamber (Biopetechs FCS2), and were imaged with a 63x/1.4 Plan-Apochromat oil immersion objective. As the immersion oil has considerable heat conductivity, the objective acts as a heat sink, if not warmed to 37°C. Hence, the objective was operated with an objective heater, which kept the objective collar at 37°C. The chamber was perfused with medium through a metal

tube on one side of the chamber, and waste medium was disposed through an identical tube on the opposite side. To keep the pH stable the cells were kept in medium with carbonate buffer and HEPES buffer. The carbonate buffer needs an atmosphere with 5% CO₂. As this could not be supplied on the microscope stage, the medium was CO₂-adapted in a gas permeable container in a cell culture incubator for at least half an hour. The medium was then filled into a syringe, which was connected to the chamber by plastic tubes via a flexible tube pump and a sterile filter. On the other side of the chamber a plastic tube led the waste medium to a waste container. The whole assembly was airtight to prevent the loss of CO₂ from the medium. The flexible tube pump was switched on and off by a solid-state relay, which was connected to the parallel port of the PC. The relay could be switched on or off by setting bit 0 of the register at the base address of the parallel port (0x378) to either 1 or 0 with the “OutPort” command of the LSM 410 macro language. The pump was run at minimal speed for 1 minute each hour. At this setting approximately 1 ml medium was perfused every three hours.

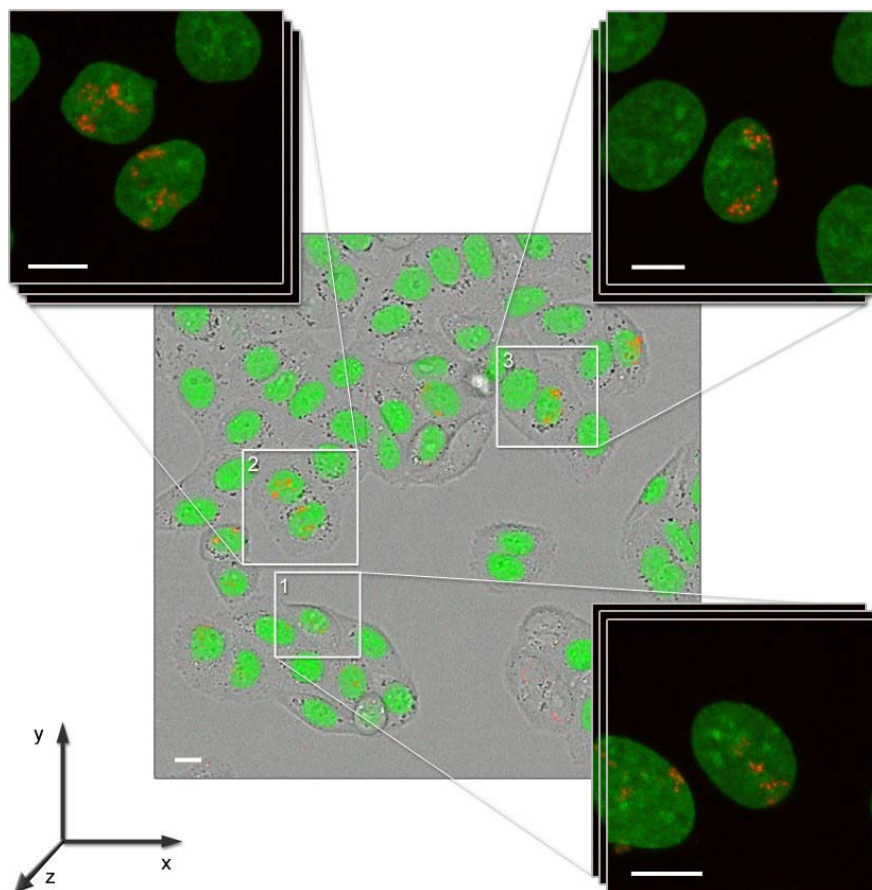


Figure 3.30: Macro for live cell confocal microscopy at the LSM 410.

The 4D-imaging macro records an overview image of the whole field of view and high-resolution z-stacks of selected ROIs at regular time intervals. Imaging parameters can be adjusted for each ROI individually. Bars: 10 μ m

The control software of the LSM 410 allows recording focus series (“3D image stacks”) and time series of light optical sections. Its capabilities were extended for live cell confocal microscopy by a macro written in the proprietary macro language of the LSM 410 control software. The macro can record time series of 3D image stacks in multiple regions of interest (ROIs) at high zoom within a common field of view (Figure 3.30). It compensates for z-axis drift, a common problem in live cell microscopy, by imaging the interface between the coverslip and the cell culture

medium in reflection contrast before each image stack is recorded. The reflected light intensity has a sharp maximum at one z-position, which is used as reference position. The macro also switches the perfusion pump. To avoid distortions in the imaging process induced by vibrations of the pump or the pressure of the pumped medium, the pump is switched on in the interval between two successive time points of imaging for a selectable duration. For the various demands of the users of this microscope versions of the macro have been created, which record image stacks for one, two and three fluorescence channels. For this work, only one fluorescence channel was needed. This version of the macro ("TimePr1") also records a transmission image produced by the transmitted excitation light at every z-position simultaneously with the fluorescence image. For the fast and easy visualization of the recorded time series a macro ("Dispt") for the dummy version of the LSM 410 software was created, which allows to scroll through the z-slices and time points of the 4D series. With this live cell observation system cells could be followed for several days on the microscope stage until they grew confluent.

To perform laser-photobleaching of GFP with this system, the Ar⁺ laser of the LSM 410 was used (488 nm, 15 mW, operated at 30% power with an attenuation filter). An image of the cell was recorded at high resolution (512x512 pixels, Zoom 8). For bleaching of stripes a line in this image was selected with the "Line Scan" function, and 2 - 5 line scans were performed without attenuation filter. For bleaching of larger areas a rectangular region of interest (ROI) was defined, and 2 - 4 images of this ROI were recorded without attenuation filter. The ROI-function of the LSM 410 only displays pixels within the selected ROI, but scans the laser along the fast scanning axis over the full width of the image. Therefore the height of the bleached region is defined by the selected ROI, but its width is defined by the image width, i.e. by the zoom factor.

3.2.2 Calibration of the detector response

In live cell microscopy it is crucial to minimize the light exposure of the observed cells as far as possible, because photodamage interferes with cell viability. For a comparison of different imaging systems it is necessary to compare the image quality of a given sample, which can be achieved with a fixed amount of fluorescence excitation power in the respective systems. In this work an absolute calibration of the laser excitation energy was not possible due to the lack of a laser power meter. However, the photomultiplier response was calibrated, i.e. the number of photons, which produce a particular gray level for a fixed set of acquisition parameters, was determined. This quantity directly corresponds with the signal to noise ratio and yields a measure for the image quality.

The first photomultiplier (PMT1) of the LSM 410, which was used for recording live cell data, was calibrated following the method described in (Heintzmann 1999), section 8.1, with small modifications. The photomultiplier was illuminated with the halogen lamp of the LSM 410 normally used for transmitted light imaging in visual mode. For a given set of image acquisition parameters images were recorded with several values of the illumination power. For each power the mean gray level in the recorded images and the variance of the gray levels was determined. To avoid an artificial increase of the variance due to a possible uneven illumination, two images were recorded for each illumination power and the variance of the difference image divided by two was plotted. The resulting quantity has the same value as the variance of a single image, but is more stable with respect to variations caused by uneven illumination.

The measured gray level (G) was assumed to have a linear dependence on the number of detected photons (n)

$$n = a \cdot G + b.$$

The parameters a and b had to be determined. As the number of detected photons follows the Poisson-statistics, the mean value $\langle n \rangle$ and variance $Var(n)$ of n are related by

$$Var(n) = n$$

a short calculation yields

$$Var(G) = \frac{\langle G \rangle}{a} + \frac{b}{a^2}.$$

$\langle G \rangle$ being the mean value of the gray level G and $Var(G)$ the variance of the gray level. For a range of contrast settings plots of $Var(G)$ versus $\langle G \rangle$ verified the linear dependence, and straight line fits to the data points yielded the values for a and b (Figure 3.31).

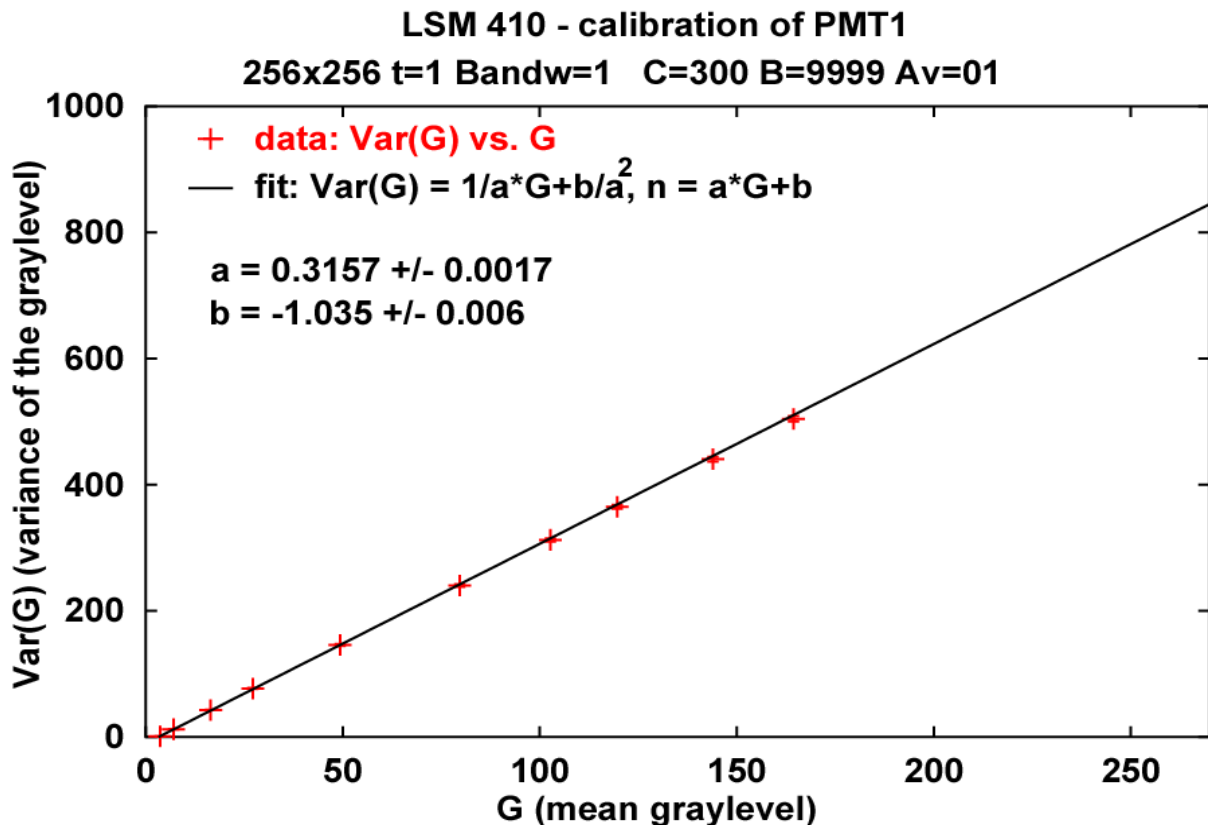


Figure 3.31: Calibration of the photomultiplier PMT1 of the LSM 410: fit of the variance versus graylevel.

All data points were recorded with the same image acquisition settings: 256x256 pixels, time parameter 1 (0.547 s per image), amplifier bandwidth parameter 1, contrast 300, brightness 9999, no averaging. Each data point (crosses) contains the combined average and variance (see text) of two images recorded with the same illumination power. Error bars for the variance are displayed but invisible because of the small measurement error. The fitted straight-line curve is in very good agreement with the data. This shows the linearity of the PMT response.

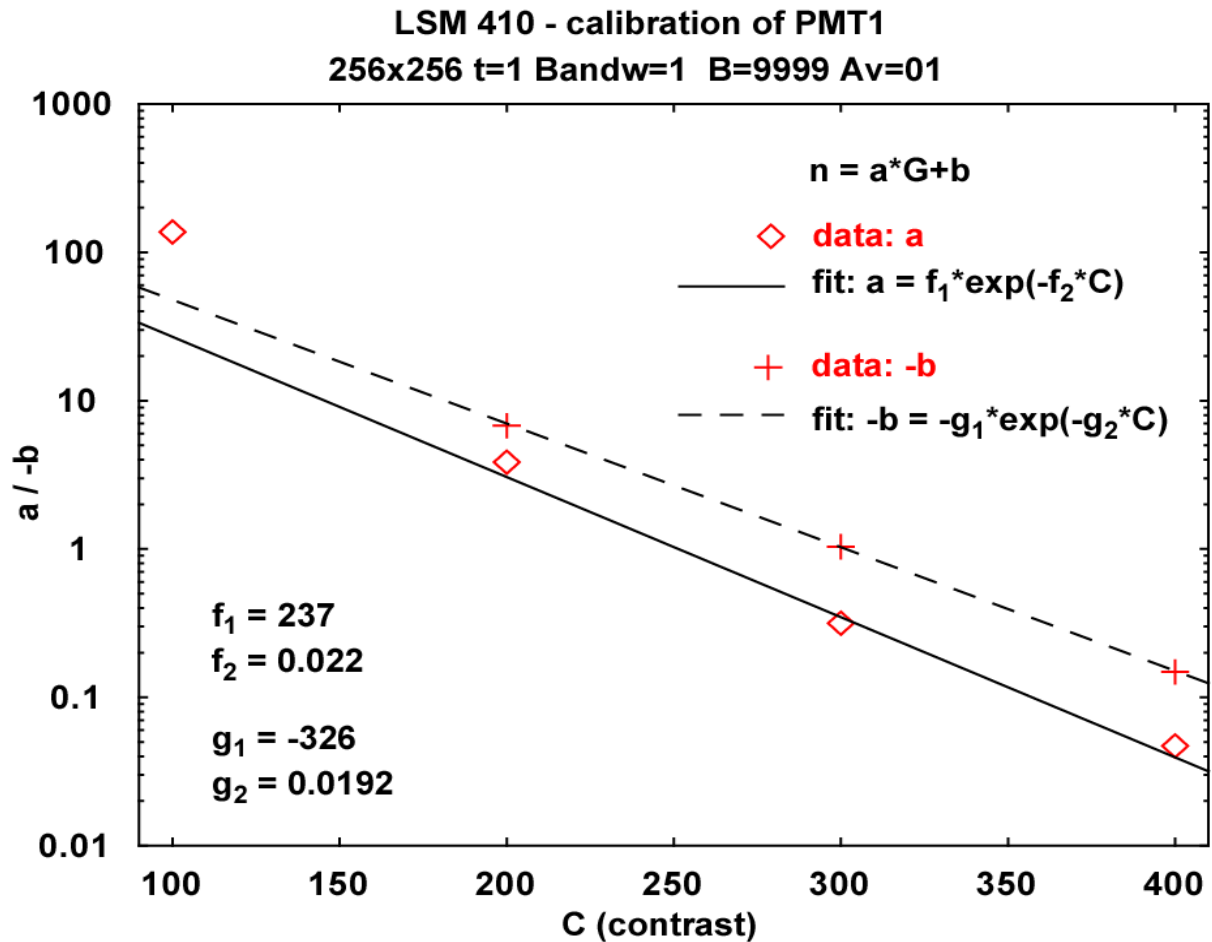


Figure 3.32: Calibration of the photomultiplier PMT1 of the LSM 410: parameters for different contrast settings

The values of the a and b parameter are plotted versus the contrast setting in the LSM 410 software (C). The parameter b is negative, and $-b$ is plotted except for $C=100$, where b is positive. For contrast settings between 200 and 400 the parameters approximately vary exponentially with contrast. The curves are fitted for this range and the resulting fit parameters are shown.

a and b were determined for contrast settings from 100 to 400 all other acquisition parameters unchanged. A logarithmic plot revealed the approximately exponential dependence of a and b on the contrast setting for contrast settings between 200 and 400 (Figure 3.32). The functions

$$a = f_1 \cdot \exp(-f_2 \cdot C) \text{ and } b = g_1 \cdot \exp(-g_2 \cdot C)$$

were fitted to the data points (Figure 3.32), and the coefficients were determined for image sizes of 256x256 and 512x512 pixels (Table 3.5). The time parameter t , the Bandwidth parameter, and the Brightness parameter B were kept constant with $t = 1$, $\text{Bandw} = 1$ and $B = 9999$. These were the parameters commonly used for confocal imaging in the experiments described here. The measurements were performed without averaging.

The number of photons corresponding to a measured gray level in an image recorded with $t = 1$, $\text{Bandw} = 1$ and $B = 9999$ can now be calculated as follows:

1. a is calculated as $a = f_1 \cdot \exp(-f_2 \cdot C)$ with C being the contrast setting in the LSM 410 software, and f_1 and f_2 taken from Table 3.5 for the appropriate image size (256x256 or 512x512 pixels).
2. b is calculated as $b = g_1 \cdot \exp(-g_2 \cdot C)$ with g_1 and g_2 taken from Table 3.5.

3. The number of photons is calculated as $n = a \cdot G + b$, where n : number of photons, and G : measured gray level.
4. If averaging is used, the photon number calculated in point 3. is multiplied by the number of averages used in recording the image.

For the experiments, which are described in the following sections, the contrast setting was usually chosen around 250, and the images were recorded with 2x averaging. For images with 256x256 pixels this results in $a=1$ and $b=-2.7$. The brightest pixel in the image usually had a gray level of about 150 for unbleached nuclei and 50 for the unbleached patches in partially bleached nuclei corresponding to photon numbers of 295 and 95, respectively. Average gray levels were about 90 for unbleached nuclei and 30 for the unbleached patches in partially bleached nuclei corresponding to photon numbers of 175 and 55, respectively.

Image size (pixels)	256 x 256	512 x 512
f_1	237	72
f_2	0.022	0.020
g_1	-326	-197
g_2	0.0192	0.020

Table 3.5: Coefficients for calculating the parameters a and b of the photomultiplier response. The coefficients were determined for the contrast range from 200 to 400 for two different image sizes: 256x256 and 512x512 pixels. The other acquisition parameters were: time parameter $t=1$ (0.547 s per image), amplifier bandwidth parameter: 1, brightness 9999, no averaging.

3.2.3 Stability of CT arrangements in interphase nuclei visualized by stripes of photobleached H2B-GFP

In order to detect major chromatin movements that could result in large-scale changes of chromatin order during interphase, stripes of photo-bleached chromatin were produced in HeLa cell nuclei with H2B-GFP at different stages of interphase. The bleached chromatin stripes could be followed for one to two hours. Due to the slow exchange of H2B-GFP from unbleached chromatin into the bleached chromatin stripes and the continued synthesis of GFP tagged histone H2B, the stripes became increasingly blurred during this period (Figure 3.33 a). Large-scale chromatin reordering during the observation period should have resulted in more or less disrupted patterns of partial stripes (see Figure 3.33 b, c).

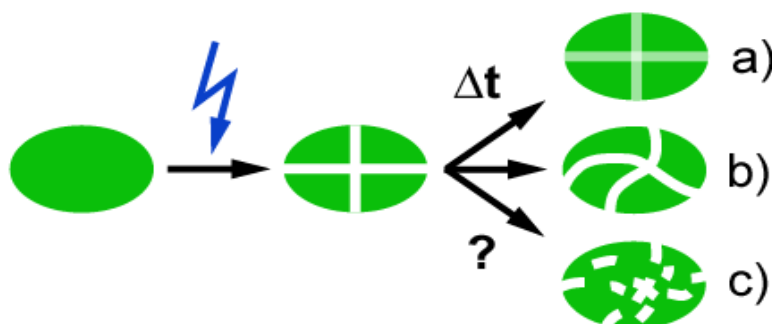


Figure 3.33: Possible results of live cell observations of photobleached stripes in H2B-GFP labeled nuclei

A cross-striped pattern is photobleached into an H2B-GFP labeled nucleus. If the location and orientation of CTs within the nucleus is stable, the pattern retains its shape, but decreases in contrast due to the exchange of H2B-GFP (a). A change in CT location and orientation would result in deformation (b) or disruption (c) of the stripe pattern.

Patterns b and c, however, were never observed. Instead, nuclei retained their original pattern during the whole possible observation period (Figure 3.34), even when these nuclei showed translational and rotational movements (see for example Figure 3.34 C). The conservation of the bleached stripe pattern provides evidence for the stability of large-scale CT arrangements in HeLa cell nuclei for time windows of at least 1 hour, independent of the interphase stage, at which bleaching was performed. This finding does not rule out the possibility that CT reordering in interphase nuclei may occur during more extended time periods.

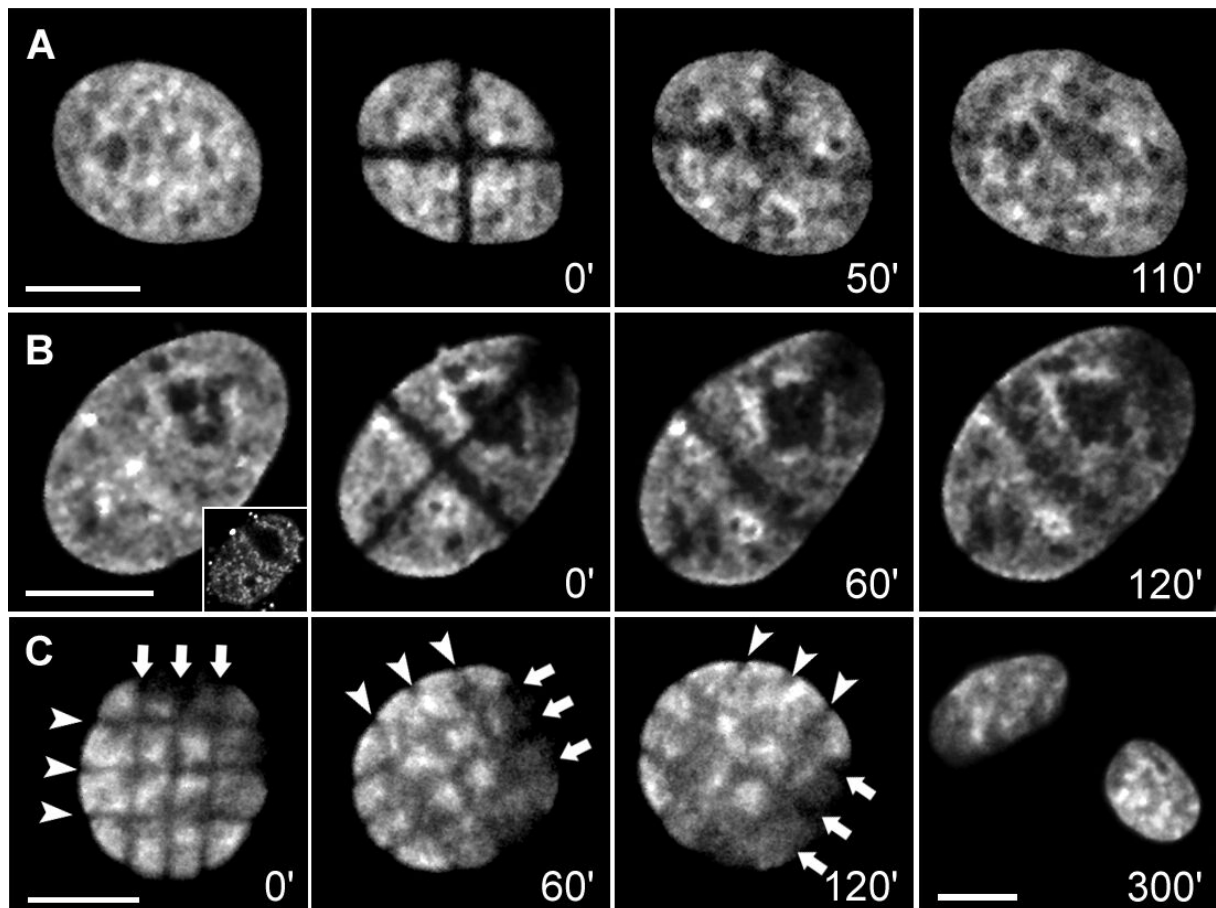


Figure 3.34: Nuclear stripe photobleaching experiments indicate stability of large scale chromosome territory arrangements during interphase of HeLa cells.

Cross-stripe (A, B) or mesh-like (C) geometrical patterns bleached into HeLa cell nuclei with GFP-tagged H2B at different stages of the cell cycle. The stripes are visible for up to two hours before recovery of GFP-fluorescence. Their patterns are maintained in all nuclei during the whole observation period.

(A) Nucleus bleached in G1 (2 hours and 20 minutes after prophase of the mother nucleus). The cross-stripe pattern is clearly visible during the first 50 min, but only faintly after 110 min, presumably due to entry into S-phase.

(B) S-phase nucleus. The nucleus was labeled with Cy5-dUTP (Schermelleh *et al.* 2001) and shows a labeling pattern typical for early S-Phase (inset). Stripe bleaching was performed two hours later, ensuring that the cell was in middle S-Phase at that time.

(C) Late S/G2 nucleus. The cell entered mitosis 3 hours after stripe bleaching. Note that the mesh-like pattern is stably maintained (arrows), while the nucleus rotates. All images show best focus light-optical sections. Bars: 10 μ m.

3.2.4 Changes of CT arrangements in mitosis visualized by unbleached H2B-GFP tagged chromatin

To test whether higher order chromatin arrangements change from one cell cycle to the next, HeLa cells were synchronized in early S-Phase (see section 2.1.5). 5-6 h after release from the block, the major part of the nuclear area was bleached leaving a single, contiguous zone of unbleached chromatin at one nuclear pole (Figure 3.35 A-C, column II). Live cell observation was started immediately after bleaching. Till the onset of prophase the area of unbleached nuclear chromatin retained its location and shape without exception. At prophase a number of unbleached chromosomal segments became visible (Figure 3.35 C, column III). 60 mother cells that were bleached completed mitosis during the observation time. In 26 cases the daughter cells showed insufficient contrast between bleached and unbleached chromatin areas or had left the area of observation. Of the cells, which were suitable for evaluation 10 mother cells were excluded from further consideration, since one or both of the resulting daughter cells showed nuclei with morphological abnormalities. The remaining 24 mother cells resulted in 48 daughter cells showing nuclei with both apparently normal morphology and sufficient contrast. These cells were studied in detail.

In approximately half of the metaphases the unbleached chromosome segments appeared clustered in one restricted area (Figure 3.35 A, column IV), whereas in the other plates patches of unbleached chromosome segments were also seen at remote sites (Figure 3.35 B, C, column IV). Accordingly, a variable degree of clustering of unbleached chromatin patches was noted in the resulting pairs of daughter nuclei (Figure 3.35, column V and VI). These patches reflect decondensed chromosomal segments. The degree of clustering was scored on maximum intensity projections. Of 48 daughter cell nuclei 20 contained a single cluster of unbleached chromatin patches within a nuclear subregion, termed pattern 1 (Figure 3.35 A, column V and VI and Figure 3.36). In 15 daughter cells most of the unbleached chromatin patches were clustered, but individual patches could be located in a remote nuclear area ("pattern 2", Figure 3.35 B, column V and VI and Figure 3.37). In 13 nuclei patches of unbleached chromatin appeared at different locations distributed over the major part of the nucleus ("pattern 3", Figure 3.35 C, column VI and Figure 3.38).

The coherent region of unbleached chromatin present in the mother nucleus was never exactly reestablished in daughter nuclei. Even in cases with the best restoration of CT order (exemplified by Figure 3.35 A, column V and VI) closely adjacent patches of unbleached chromatin appeared separated by bleached chromatin zones suggesting that chromosome segments with bleached chromatin had moved between unbleached chromosome segments.

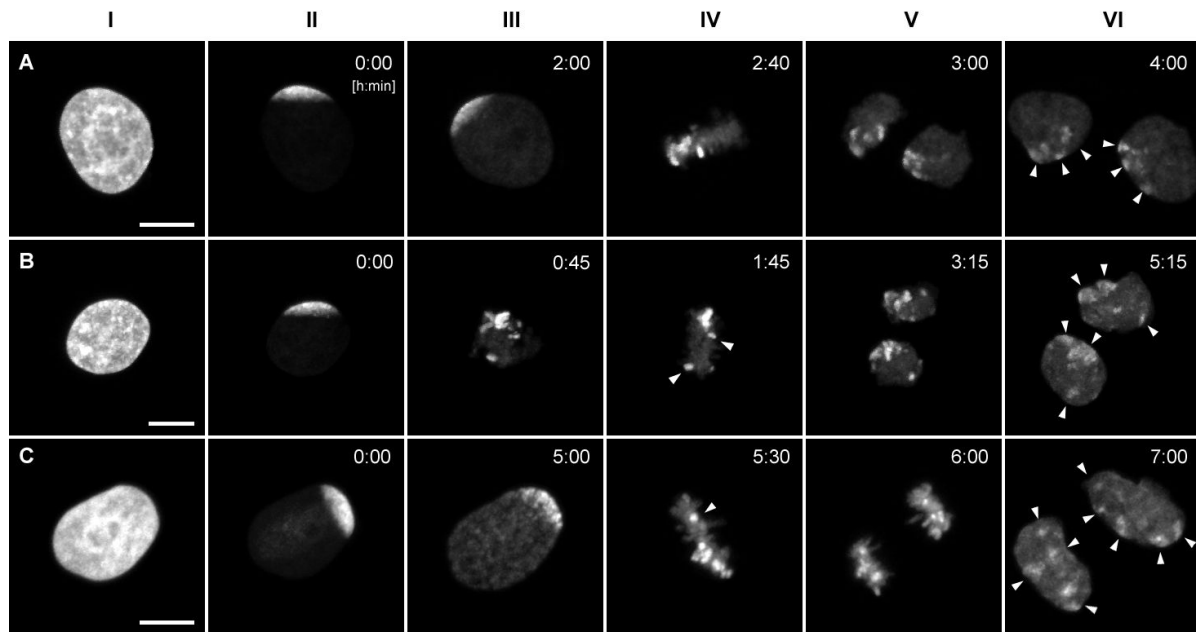


Figure 3.35: Large scale chromosome territory arrangements in HeLa cell nuclei change from one cell cycle to the next.

Rows A to C show examples of live cell confocal image series from three HeLa cells. After bleaching of GFP labeled chromatin except for a contiguous unbleached region at one nuclear pole in G2, cells were followed through mitosis till the formation of daughter nuclei. All images are maximum intensity projections of confocal image stacks. The degree of the redistribution of unbleached chromatin patches in G1 daughter cells (column VI, arrowheads) can vary from “clustered” (row A) to “partially clustered” (row B) to “scattered” (row C). Column I: GFP pattern of HeLa nuclei before bleaching; Column II: respective nuclei after partial bleaching; Column III: last frame recorded prior to the formation of the metaphase plate; Column IV: metaphase plate, arrowheads in B and C point to unbleached chromosomal fragments that are remote from the bulk of unbleached chromatin. Column V and VI: daughter nuclei in anaphase (column V, C) or telophase (column V, A and B) and in G1 (column VI). Bars: 10 μm

18 of the 24 pairs of daughter nuclei showed similar patterns, i.e. both nuclei showed either a clustering of unbleached chromatin or a dispersed pattern. In six cases scattering of unbleached chromatin patches was more pronounced in one daughter nucleus than in the other. Most of the pairs of daughter nuclei, of which both nuclei belonged to the same pattern, had a symmetrical arrangement of the unbleached patches (Figure 3.36, Figure 3.37, Figure 3.38).

To test, whether fluorescent patches reflect areas of high chromatin density rather than unbleached chromosome segments, fixed daughter cells of cells with partially bleached nuclei were stained with propidium iodide (PI) for a nuclear counterstain. Confocal image stacks of the three pairs of daughter nuclei showed no particularly strong PI signal at sites of strong GFP fluorescence (Figure 3.39). In another control experiment nuclei were bleached completely and followed through mitosis. In this experiment strongly fluorescent patches like the patches in daughter cells of partially bleached nuclei were not detected (Figure 3.40). These experiments show that the strongly fluorescent patches in daughter nuclei of partially bleached nuclei in fact show chromatin from the unbleached nuclear region.

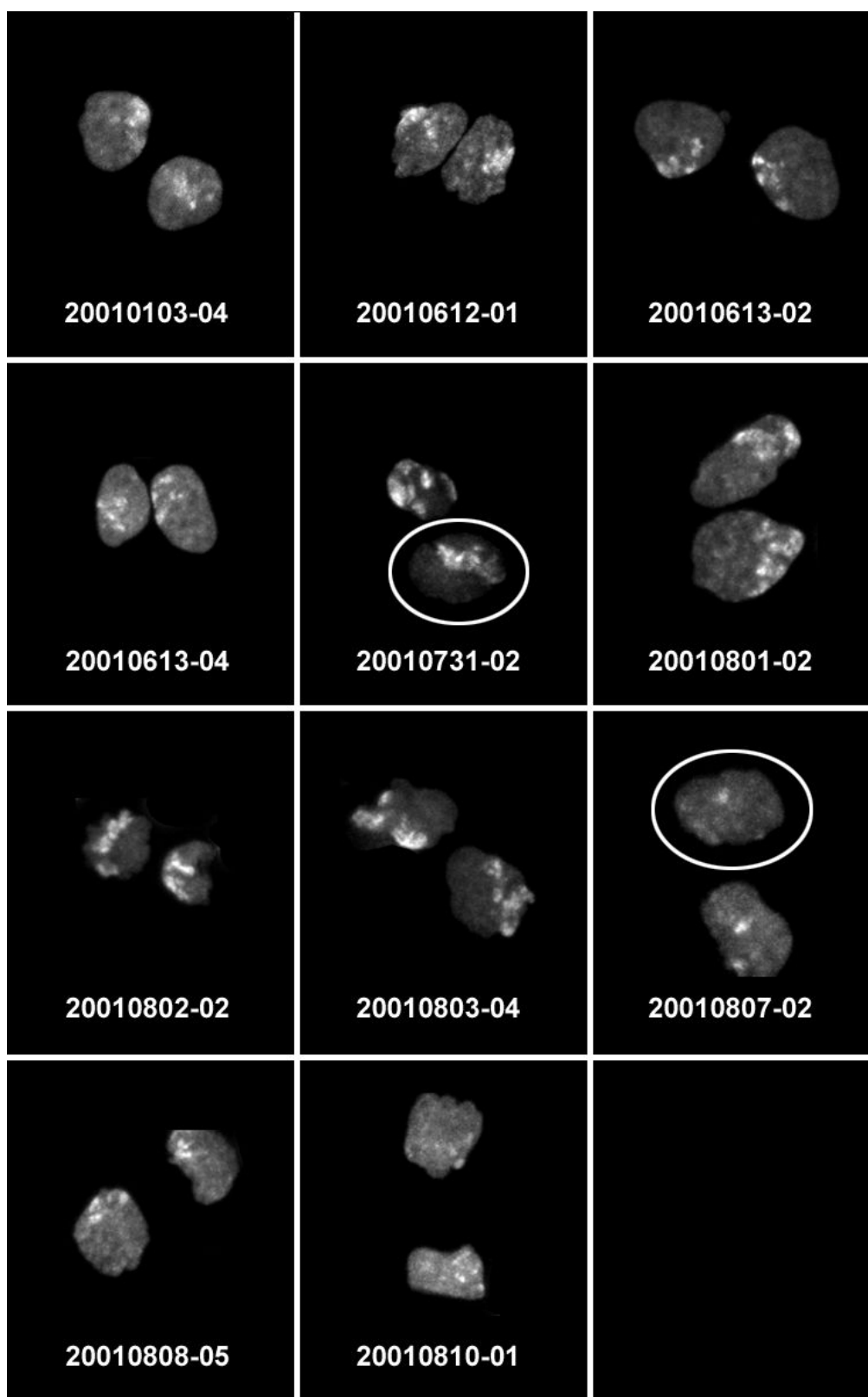


Figure 3.36: Daughter nuclei with clustered unbleached patches (pattern 1)

The panel shows maximum intensity projections of confocal image stacks of all evaluated pairs of daughter nuclei, which contain at least one nucleus with pattern 1. The numbers specify the date of the experiment and the number of the nucleus within the experiment. In cases, where daughter nuclei were assigned to different patterns (20010731-02 and 20010807-02), nuclei assigned to pattern 1 are encircled.

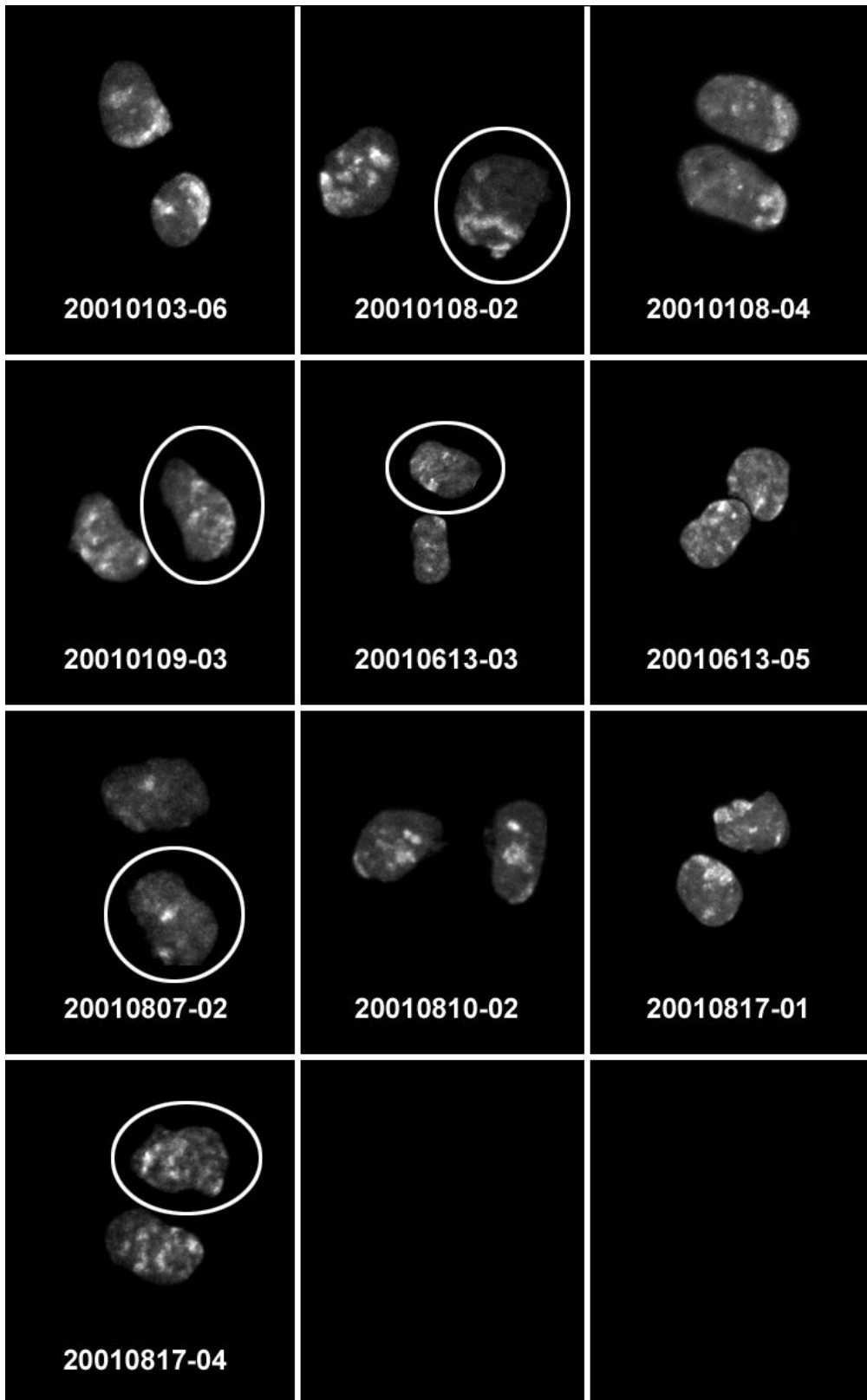


Figure 3.37: Daughter nuclei with a cluster of unbleached patches and individual patches remote from the cluster (pattern 2)

Same as Figure 3.36, but for all daughter nuclei showing pattern 2. In cases, where daughter nuclei were assigned to different patterns (20010108-02, 20010109-03, 20010613-03, 20010807-02, 20010817-04), nuclei assigned to pattern 2 are encircled.

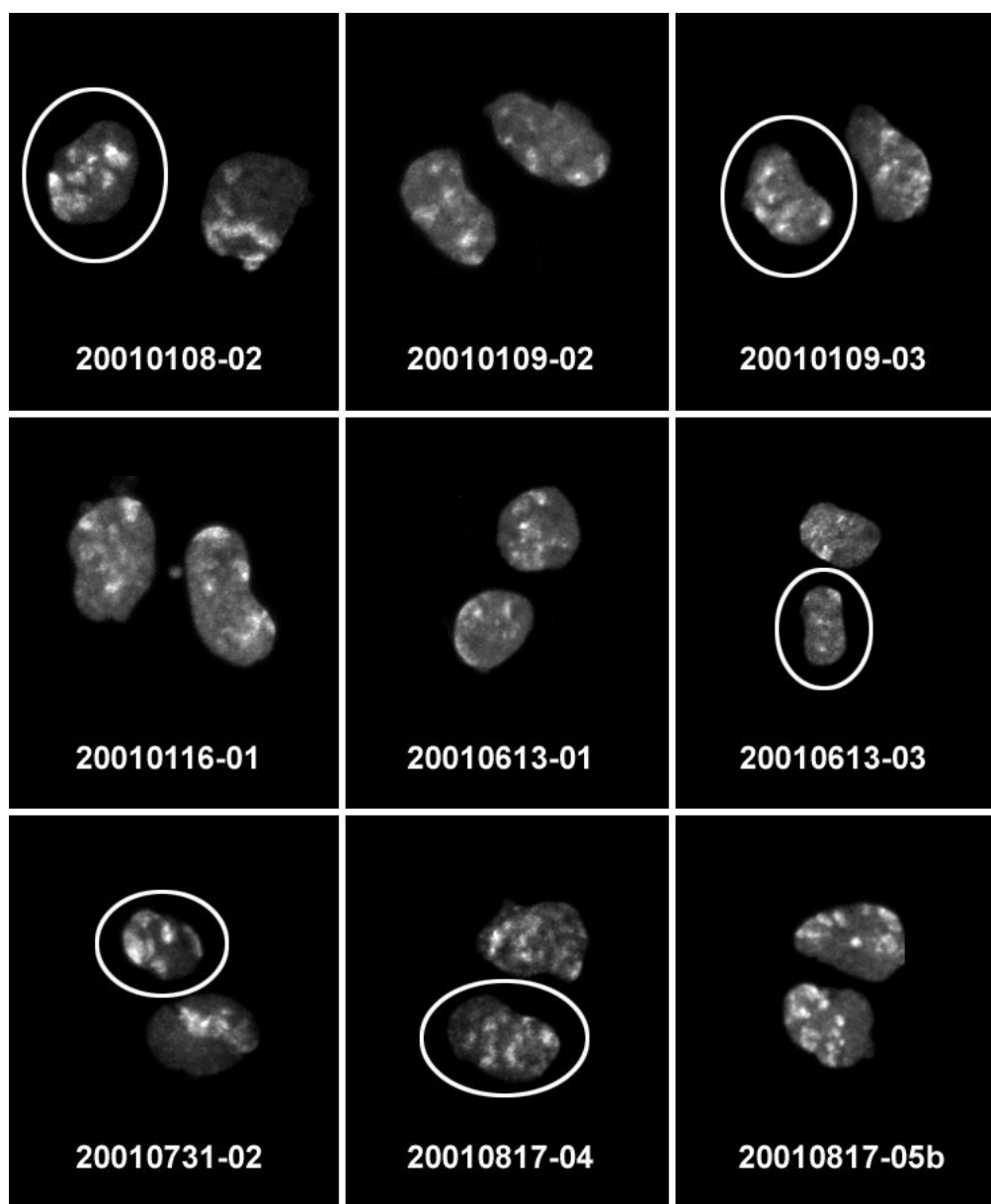


Figure 3.38: Daughter nuclei with unbleached patches scattered over the nucleus

Same as Figure 3.36, but for all daughter nuclei showing pattern 3. In cases, where daughter nuclei were assigned to different patterns (20010108-02, 20010109-03, 20010613-03, 20010731-02, 20010817-04), nuclei assigned to pattern 3 are encircled.

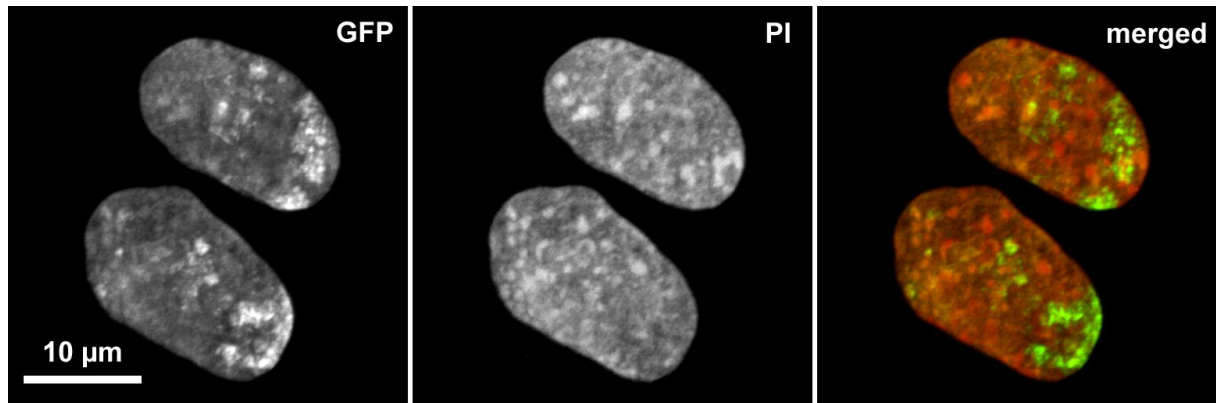


Figure 3.39: Signal of unbleached H2B-GFP-patches and nuclear counterstain of a pair of daughter nuclei of a partially bleached nucleus

Shown are maximum intensity projections of confocal image stacks after fixation and PI staining (compare Figure 3.37 experiment 20010108-04). The unbleached H2B-GFP patches (“GFP”) cluster at the lower right end of the nuclei. Individual patches are remote from the clusters. The nuclear counterstain (“PI”) has a more even distribution. The overlay of the two images (“merged”; green: GFP, red: PI) shows that there is no correlation between the unbleached H2B-GFP patches and high intensity regions of PI.

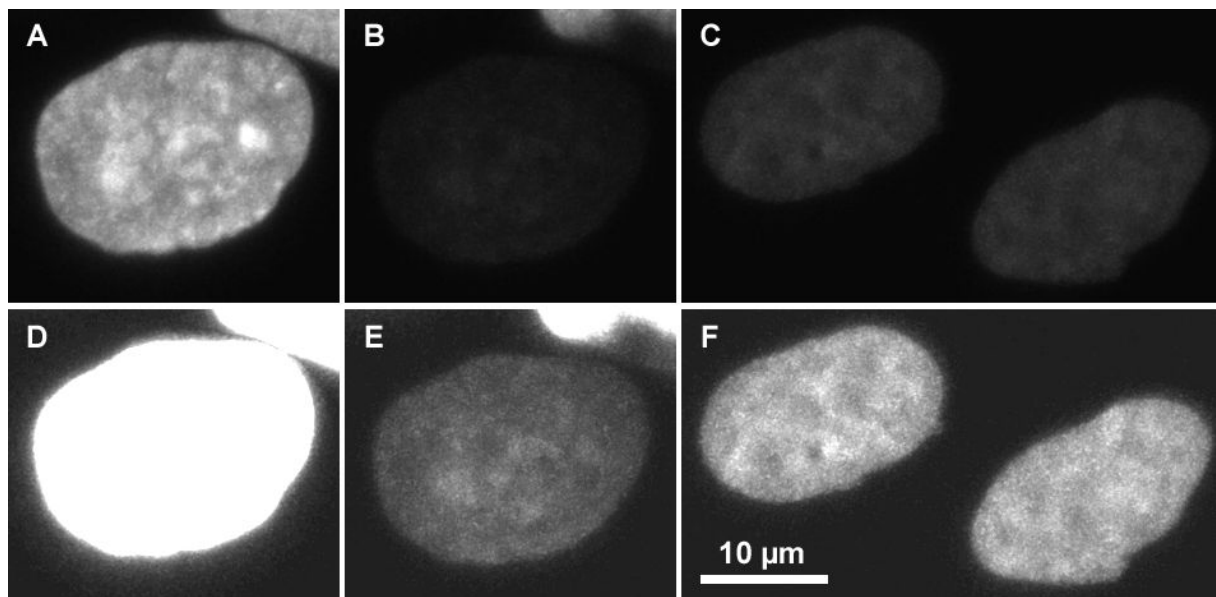


Figure 3.40: GFP staining pattern of a completely bleached nucleus and its daughter nuclei

The images show maximum intensity projections of confocal image stacks.

(A) Nucleus before bleaching. The H2B-GFP staining has the pattern of a nuclear counterstain. Part of a neighboring nucleus is seen in the upper right corner.

(B) Image recorded immediately after bleaching of the whole nucleus. The nucleus is only faintly visible.

(C) Image of the daughter cell nuclei. The nuclei look brighter than the nucleus in (B) due to the recovery of H2B-GFP fluorescence.

(D, E, F) The same recordings as (A, B, C), respectively, but with the contrast enhanced by a factor of four. The unbleached nucleus (D) is overexposed. The H2B-GFP staining of the daughter nuclei (F) has the pattern of a nuclear counterstain. Compare to the H2B-GFP staining and the PI staining in Figure 3.39

3.2.5 Quantitative evaluation of changes in the radial distribution of unbleached chromatin in mitosis

CTs in human cell nuclei have a reproducible radial distribution (Boyle *et al.* 2001; Cremer *et al.* 2001). E.g. in human lymphocyte nuclei CT #19 assumes a more interior position than CT #18. This distribution is evolutionary conserved (Tanabe *et al.* 2002b) implying a functional role.

As in the experiments in section 3.2.4 above a peripheral zone of the nucleus remained unbleached, it was assumed that the unbleached patches in the daughter nuclei would also be located at the nuclear periphery. This hypothesis was tested as follows: The cells in these experiments lacked a nuclear counterstain for the total chromatin, because the H2B-GFP had been partially bleached. Therefore the upper and lower nuclear border could not be clearly identified, and the evaluation was performed on 2 - 4 mid-nuclear sections.

The nuclear area in these sections was segmented by selection of a threshold, which was lower than the residual GFP fluorescence in the bleached area, but higher than the background fluorescence outside the nucleus. As in nuclei just after bleaching the residual fluorescence was very low, a low threshold had to be selected, which could lead to an overestimation of the nuclear area. To estimate the effect of this overestimation, the nuclear area in nuclei before bleaching was segmented with two thresholds. A high threshold was selected according to the visual impression, and compared to a low threshold corresponding to the one used on nuclei after bleaching (Figure 3.41 A, B).

In each section the nuclear area was divided into 50 shells each containing pixels with the same relative distance from the geometric nuclear center. The relative distance from the center was calculated for each pixel by extending the line from the nuclear center to the regarded pixel until the nuclear border was hit. The distance of the pixel from the center divided by the distance of the border from the center along this line was the relative distance. The 50 shells of equal relative distance were combined to five shells of equal area shell #1 being the innermost shell and shell #5 the most peripheral one. The proportion of unbleached chromatin in each of the five shells was determined. The unbleached chromatin regions were identified as 2% and 10% of the pixels of highest intensity GFP-signal within the evaluated mid-nuclear sections (Figure 3.41). 2% was a lower estimate, which contained exclusively pixels of the unbleached regions, but did not completely cover the unbleached regions. 10% was an upper estimate, which completely covered the unbleached regions, but included some pixels not belonging to the unbleached regions. The threshold for the segmentation of the respective percentage of high intensity nuclear pixels was determined, and subtracted from all intensity values. This procedure suppressed the contribution of unspecific signals with intensities just above the threshold level. For the evaluation a plugin written for ImageJ (Rasband 1997-2003) was used.

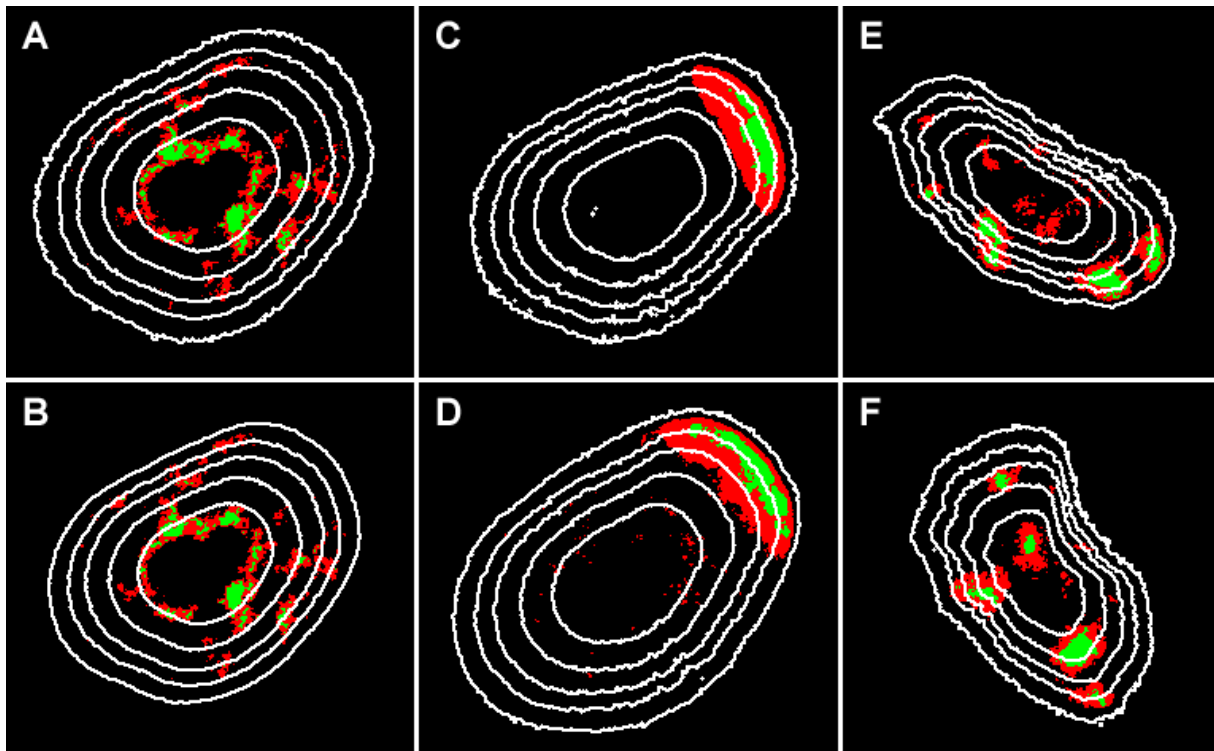


Figure 3.41: Segmentation of a nucleus for the quantification of the radial distribution of unbleached chromatin

Shown are maximum intensity projections of the mid-nuclear sections used for evaluation of the nucleus / daughter nuclei displayed in Figure 3.35 C. Red/green: 10% highest intensity chromatin; green: 2% highest intensity chromatin; white lines outline five radial shells with equal area.

(A): The nucleus just before bleaching. A low threshold is selected for the segmentation of the nuclear counterstain. Most of the high intensity chromatin is located around the nucleoli (not shown).

(B): The nucleus just before bleaching. A high threshold is selected for the segmentation of the nuclear counterstain. Consequently, the nucleus appears smaller.

(C): The nucleus immediately after bleaching. The high intensity chromatin is located at one nuclear pole. As there is low GFP-fluorescence in the bleached region, some pixels within the nucleus have intensities below the threshold for selecting the nuclear counterstain. White “dots” within the shells are the outlines of such pixels.

(D): The last recorded image before the nucleus enters prophase. The bulk of the high intensity chromatin is still located at one nuclear pole. Additionally, there are small speckles belonging to the 10% highest intensity fraction scattered all over the nucleus resulting from the recovery of GFP-fluorescence in bleached areas.

(E), (F): The daughter nuclei. The highest intensity chromatin is located in patches scattered over the nucleus.

The evaluation was performed on image stacks recorded before bleaching, immediately after bleaching, just before the cells entered prophase and after mitosis for the 24 mother nuclei and their 48 daughter nuclei evaluated in section 3.2.4. Figure 3.42 and Figure 3.43 show the resulting proportions of the 10% highest intensity chromatin fraction and the 2% fraction, respectively, averaged over the evaluated nuclei. The results for the 10% fraction and the 2% fraction are similar.

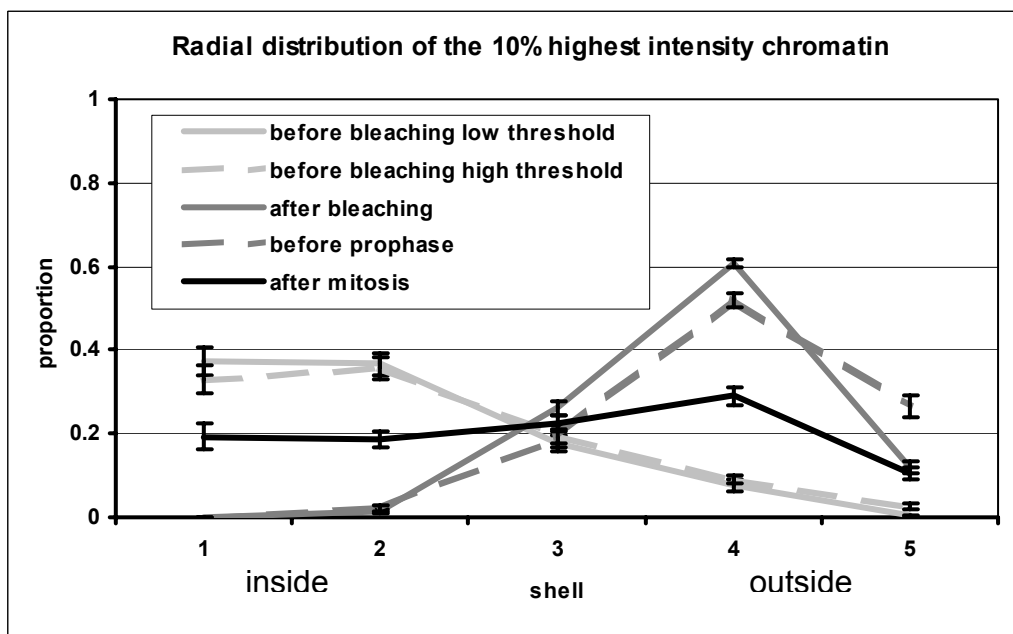


Figure 3.42: Average radial distribution of the 10% highest intensity chromatin fraction in partially bleached and unbleached H2B-GFP HeLa cells

The proportion of the 10% highest intensity chromatin fraction in each of the five radial shells of equal area is shown. The data are average values from 24 nuclei and their daughter nuclei. #1: innermost shell; #5: most peripheral shell. In unbleached nuclei more than 60% of the 10% fraction are located in the two inner shells (“before bleaching low threshold”). This situation does not change, when a higher threshold is selected for defining the nuclear area (“before bleaching high threshold”, compare Figure 3.41 A and B). Just after bleaching almost 100% of the 10% fraction is in the three outer shells as a peripheral part of the nucleus has been left unbleached. The proportion in shell #5 is lower than that in shell #4 due to the difficulty to define a threshold for the counterstain in bleached nuclei. The same result is obtained just before the nuclei enter prophase. In the daughter nuclei (“after mitosis”) the 10% fraction is distributed almost equally over the five shells with a slight increase in shell 4. Error bars denote standard errors of the mean.

In unbleached nuclei the major proportion of the high intensity chromatin was located in the two inner shells for both levels of the nuclear threshold. In contrast, just after bleaching almost 100% of the high intensity chromatin were in the three outer shells. The reason for this is that the major part of the nucleus except for a peripheral part had been bleached, and high intensity fluorescence did no longer appear at areas of high chromatin density but at areas which had been deliberately selected to remain unbleached. The proportion in shell #5 was lower than that in shell #4 due to the aforementioned problem of defining a threshold for the counterstain in bleached nuclei. The same result was obtained just before the nuclei entered prophase. At this time, however, a larger proportion was in the outer shell #5. This can be attributed to the recovery of nuclear GFP-fluorescence in the time period after bleaching. The higher fluorescence signal in the whole nucleus allowed to select a higher threshold. Due to this higher threshold the nuclear rim as segmented by the threshold moved closer to the unbleached region.

In the daughter nuclei the high intensity fraction was distributed almost equally over the five shells with only a slight increase in shell #4. This finding is in contrast to the strongly peripheral localization of the high intensity fraction in nuclei just after bleaching and before prophase. Therefore, these results do not argue for a localization of the peripheral unbleached chromatin in mother nuclei to the periphery of the daughter nuclei.

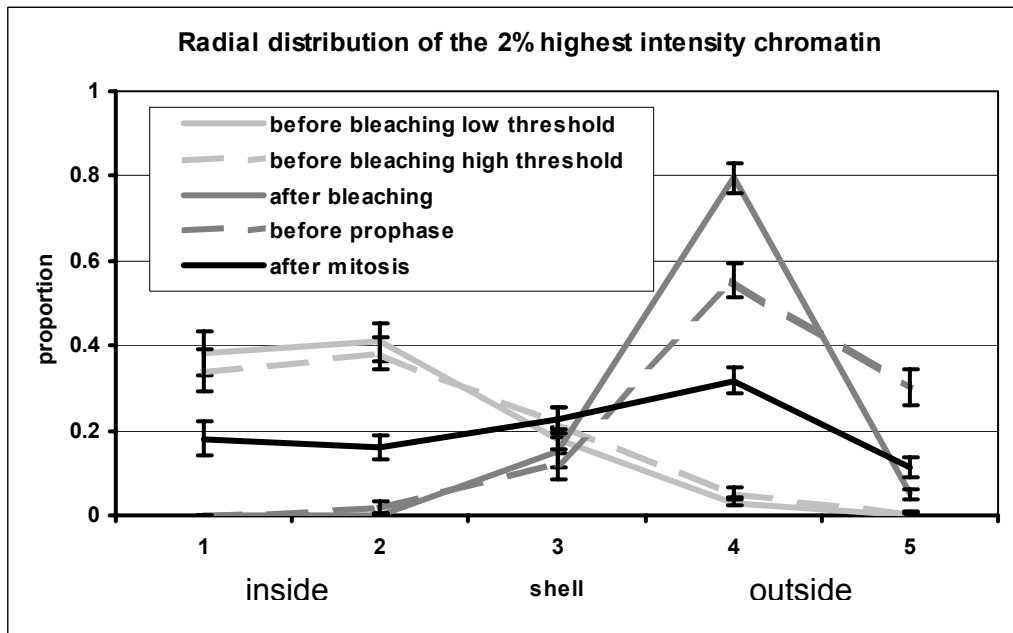


Figure 3.43: Average radial distribution of the 2% highest intensity chromatin fraction in partially bleached and unbleached H2B-GFP HeLa cells

Same as Figure 3.42 for the 2% highest intensity chromatin fraction. The distribution of the 2% fraction is the same as that of the 10% fraction. Note that for nuclei immediately after bleaching and just before prophase the peak in shell #4 is higher than in Figure 3.42, because GFP-fluorescence in the unbleached zone but close to the bleached area has been affected by the bleaching.

3.2.6 Quantitative evaluation of the degree of clustering of unbleached chromatin by an autocorrelation method

In addition to the visual analysis of the apparent changes of higher order chromatin arrangements between mother and daughter cell nuclei described in section 3.2.4 a procedure to quantify the degree of clustering of unbleached chromatin was applied. This method was based on the distribution of distances between pairs of high intensity signals, which was quantified by means of an autocorrelation approach.

As the cells in these experiments did not have a counterstain for the total chromatin, the evaluation was performed on 2 - 4 mid-nuclear sections. In these sections the nuclear area was segmented at low threshold on the basis of the residual fluorescence in the bleached area. Thereafter the threshold for the segmentation of a fraction of high intensity nuclear pixels (2% or 10%) was determined and subtracted from all intensity values. These fractions were taken as the representation of the unbleached chromatin. See section 3.2.5 above for a more detailed description of the evaluation steps up to this point. Average intensity projections of the segmented mid-sections were calculated, and the mean nuclear area was calculated from the areas in the evaluated sections.

Distances between all possible pairs of pixels (i and j) representing unbleached chromatin were determined and normalized to the size of the nucleus (relative distance d), i.e.

$$d(i, j) = \frac{1}{\sqrt{A}} \sqrt{(\bar{x}_i - \bar{x}_j)^2} \quad , \text{ with}$$

\bar{x}_i, \bar{x}_j : the positions of pixels i and j .

A : the nuclear area

Distance values were grouped into intervals of increasing relative distances. As an intensity weighted measure, which reflects how many pairs of pixels fall into each relative distance interval, a correlation function, here called radial autocorrelation function (*RAC*), was established.

$$RAC(d) = \frac{1}{(\sum_i I_i)^2} \sum_{i,j; d \leq d(i,i) < d+0.1} I_i \cdot I_j, \text{ with}$$

I_i, I_j : fluorescence signals of pixels i and j (minus the threshold intensity)

d : The starting value of a relative distance interval. $d = 0, 0.1, 0.2, \dots$

The calculation was performed by means of a plugin for ImageJ (Rasband 1997-2003).

Another way of obtaining the *RAC* would be to first calculate the autocorrelation image (Gonzalez and P. 1987; Jähne *et al.* 1999) of the 2% or 10% highest intensity pixels in the maximum intensity projection. In the autocorrelation image each pixel represents one possible distance vector between pairs of pixels in the original image. The intensity value of this pixel is large if there are many pairs of high intensity pixels in the original image, which are separated by the corresponding distance vector. The *RAC* for a relative distance interval d can then be computed from the autocorrelation image by summing the intensities of all pixels, whose relative distance from the origin (e.g. the pixel corresponding to the distance vector of zero length) is between d and $d+0.1$ and afterwards applying a normalization. This procedure yields the average radial variation of the autocorrelation image, hence the term “radial” autocorrelation function.

An important property of the *RAC* is that its values summed over all d add up to 1. Furthermore, all values of the *RAC* are positive. These two properties allow it to be interpreted as a probability distribution. If the intensity of a pixel in an image is assumed to be proportional to the number of fluorescence molecules contributing to that pixel, the value of the *RAC* for a distance interval d is the probability that two arbitrarily selected fluorescence molecules in the nucleus are separated by a distance within this distance interval. With this interpretation in mind the mean relative distance $\langle d \rangle$ for a *RAC* curve can be calculated. *RAC* curves for schematic example nuclei and the corresponding mean relative distances $\langle d \rangle$ are displayed in Figure 3.44 to visualize how the *RAC* depends on the degree of clustering of high intensity signals. The *RAC* for all nuclear pixels has a broad distribution with low values for low and high values of d and a maximum at $d = 0.4$ (Figure 3.44 A). In contrast the *RAC* for a high intensity region, which occupies 10% of the nuclear area, or for patches occupying 10% (Figure 3.44 B) has a pronounced maximum at $d = 0.1$ reflecting the localization of all high intensity pixels in a small region. If the patches of high intensity pixels are less clustered or scattered over the nucleus (Figure 3.44 D, E) the *RAC* extends to larger values of d . Note, however, that in these cases the *RAC* still has a pronounced local maximum at small values of d . This maximum reflects the concentration of the high intensity pixels in patches. Only if the individual high intensity pixels are scattered randomly over the nucleus (Figure 3.44 F), the *RAC* has the same broad shape as for all nuclear pixels.

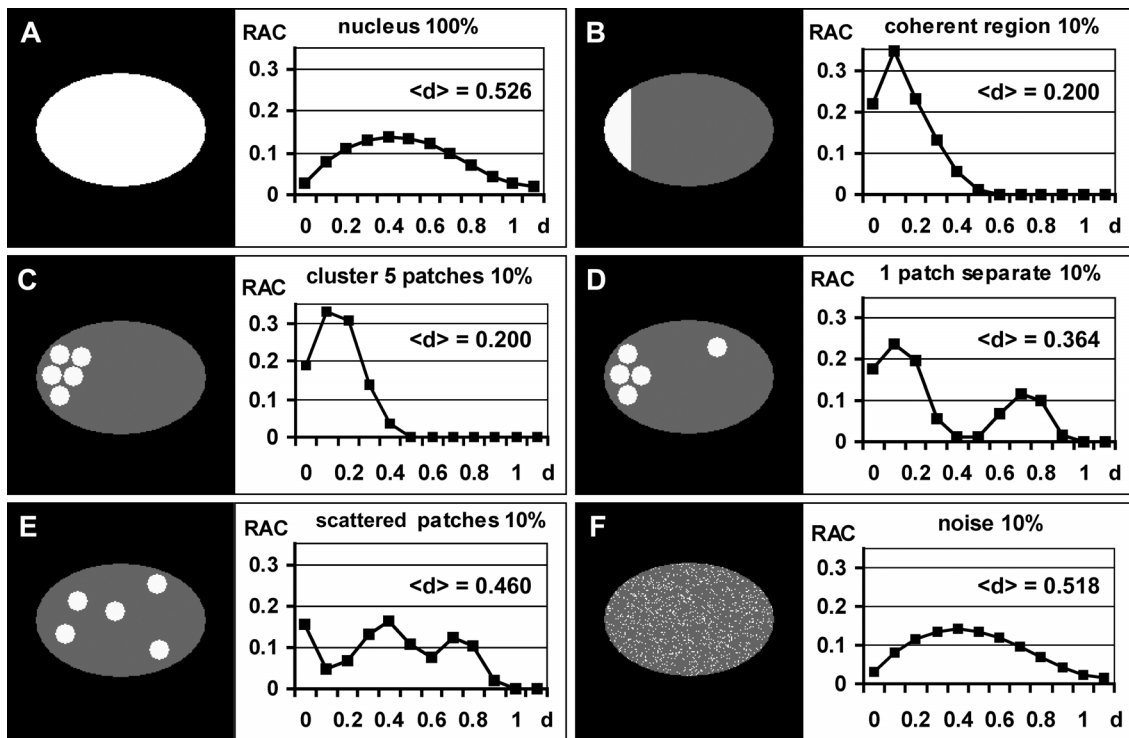


Figure 3.44: Radial autocorrelation function (*RAC*) shown for simulations of typical distributions of unbleached chromatin.

The ordinate represents *RAC* values, the abscissa normalized distances between pixels for different distance intervals d . Note that the contribution of pixels to the *RAC* curve depends on their intensity values. In this simulation all pixels counted were of the same intensity, whereas pixel intensities varied in experimental nuclei.

(A) *RAC* curve calculated from all nuclear pixels (100%) of a nucleus showing equal pixel intensities at all sites. The curve shows a broad distribution with a maximum at $d = 0.4$. $\langle d \rangle = 0.526$.

(B) *RAC* curve calculated for a coherent, high intensity region at one nuclear pole, which occupies 10% of the nuclear area. It has a peak at the relative distance interval 0.1 (comprising relative distances $d \geq 0.1$ and < 0.2) and is zero for relative distances ≥ 0.6 . $\langle d \rangle = 0.200$

(C) A nucleus with 5 high intensity patches, which together occupy 10% of the nuclear area. The patches are clustered. The maximum of the *RAC* at $d = 0.1$ has become broader. $\langle d \rangle$ has not changed considerably: $\langle d \rangle = 0.200$

(D) A nucleus with 5 high intensity patches. Four of the patches form a cluster and one is located at a distant site. The *RAC* still has its maximum at $d = 0.1$. In addition there is a second lower maximum at 0.7. $\langle d \rangle = 0.364$

(E) A nucleus with 5 high intensity patches scattered over the whole nuclear area. The *RAC* curve shows three local maxima that represent small, medium and large distance clusters. $\langle d \rangle = 0.460$

(F) A nucleus, which contains Gaussian noise after thresholding of the 10% highest intensity pixels. The *RAC* was calculated from the thresholded pixels. It is almost identical to the *RAC* in (A). $\langle d \rangle = 0.518$

The *RAC* was calculated for the highest intensity 10% and 2% chromatin fractions for all 24 mother nuclei immediately after bleaching and just before prophase, as well as for the 48 daughter nuclei. Figure 3.45 displays the averages of the resulting curves for each regarded cell cycle stage. The *RAC* for 100% of the chromatin in the unbleached mother nuclei is displayed as a reference, which represents the maximally possible degree of spreading of unbleached chromatin (compare Figure 3.44 A). The mean relative distance $\langle d \rangle$ was calculated for each nucleus, and the median values of $\langle d \rangle$ for each cell cycle stage are listed in Table 3.6. The statistical significance of differences in the median values of $\langle d \rangle$ were tested with the Mann-Whitney U-test (Barlow 1989). This test is a non-parametric test for differences of the median values of two samples. It is not based on an assumption

about the distribution of $\langle d \rangle$. Particularly, it does not assume that the values of $\langle d \rangle$ have a Gaussian distribution.

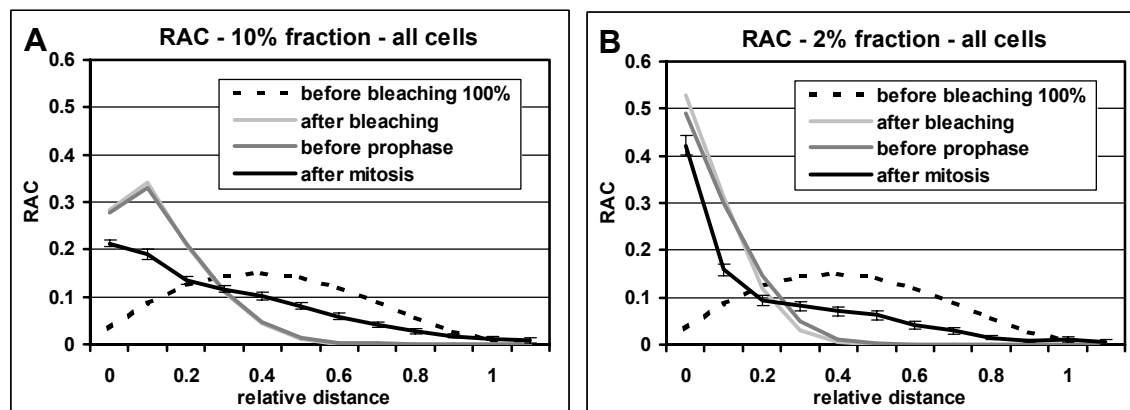


Figure 3.45: Average RAC curves established from 24 mother cell nuclei before bleaching, after bleaching and before prophase, as well as for their 48 daughter cell nuclei

The 10% (A) and 2% (B) highest intensity fractions were evaluated. Standard deviations of the mean are indicated only for nuclei after mitosis, but are within the same order for all stages. The distribution of unbleached chromatin remains closely similar in mother nuclei after bleaching till the end of G2. Compared with the curves for mother nuclei the curves for daughter nuclei for both 10% and 2% show increased values at larger relative distances reflecting a wider spreading of the highest intensity fractions. Note the complete match of the RAC curves established for the mother nuclei immediately after bleaching and before the onset of prophase in (A), while a small difference is noted in (B).

median ($\langle d \rangle$)	after bleaching	before prophase	after mitosis
10%	0.179 (0.161 - 0.209)	0.187 (0.161 - 0.219)	0.321 (0.183 - 0.612)
2%	0.116 (0.082 - 0.184)	0.124 (0.087 - 0.207)	0.243 (0.088 - 0.596)

Table 3.6: Median and Min-Max values of the mean relative distances for the 10% and 2% highest intensity chromatin fraction in nuclei after bleaching, before prophase and after mitosis

The values were calculated from the RAC curves shown in Figure 3.45. For both the 10% and the 2% fraction the values before prophase are slightly smaller than the values after bleaching. This difference is significant ($p = 0.03$) for the 2% fraction, but not significant ($p = 0.2$) for the 10% fraction (see the differences of the respective curves in Figure 3.45). The values after mitosis are highly significantly larger than the values before prophase ($p < 0.001$) for both fractions, and for both fractions the difference between $\langle d \rangle$ after mitosis and before prophase is more than 10x larger than the difference between $\langle d \rangle$ before prophase and after bleaching.

The RAC curves for the daughter nuclei (“after mitosis”) differ strongly from the curves for the mother nuclei before prophase (Figure 3.45) in that they have higher values for large relative distances. The respective median values of $\langle d \rangle$ differ by 0.146 (10% fraction) and 0.119 (2% fraction, Table 3.6). This difference is highly significant ($p < 0.001$ for both fractions). In contrast the RAC curves for the mother nuclei after bleaching and before prophase are closely similar (Figure 3.45 B) or even match completely (Figure 3.45 A), and the respective median values of $\langle d \rangle$ differ by only 0.008 (both fractions) reflecting the observation that till the onset of prophase the area of unbleached nuclear chromatin retained its shape (see Figure 3.35). The difference is not significant for the 10% fraction ($p = 0.2$) and significant for the 2% fraction ($p = 0.03$). The small but significant difference for the 2% fraction is in agreement with the slight difference of the respective RAC curves in Figure 3.45 B. It can possibly be explained by constrained diffusive movements of chromatin during interphase (Bornfleth *et al.* 1999). The relatively large and highly significant difference of the median values of $\langle d \rangle$ between nuclei after mitosis and nuclei before

prophase clearly supports the observation that the unbleached patches in nuclei after mitosis were more strongly distributed over the nucleus than the coherent unbleached regions in the mother nuclei (section 3.2.4).

Since daughter nuclei with scattered, unbleached chromatin patches (pattern 3 as defined in section 3.2.4) might have contributed decisively to this significance level, the class of daughter nuclei showing a single cluster of unbleached chromatin patches (pattern 1) was tested against the nuclei before prophase. Again a highly significant difference ($p < 0.001$) was found for both high intensity fractions. The average *RAC* curves for daughter nuclei with patterns 1-3 are shown in Figure 3.46, and the respective median values of $\langle d \rangle$ are listed in Table 3.7. Interestingly, the relative distances of pattern 1 and pattern 2 do not differ significantly, whereas those of pattern 3 differ with high significance from the other two patterns. A possible reason for this is that the individual patches, which are remote from the cluster of unbleached patches in nuclei with pattern 2, are relatively small.

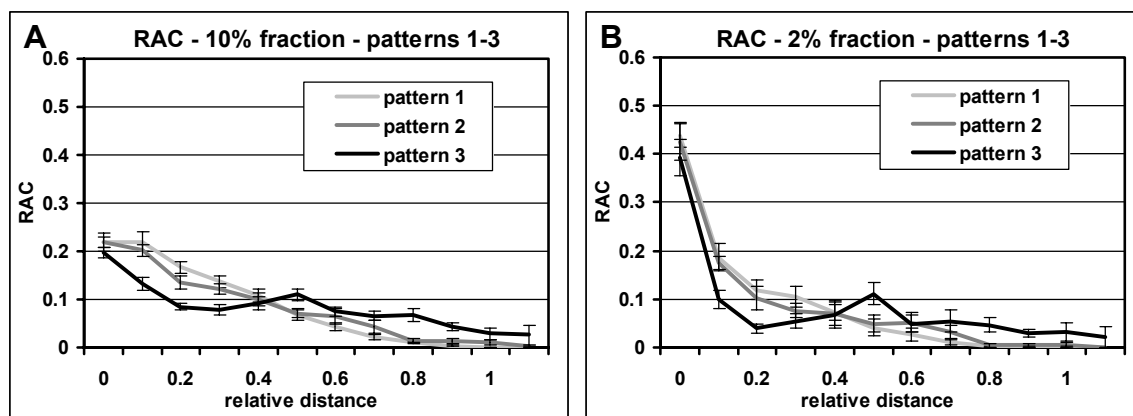


Figure 3.46: Average *RAC* curves established from the daughter nuclei classified by the degree of clustering of their unbleached chromatin patches

The daughter nuclei were classified into the patterns introduced in section 3.2.4: 20 nuclei with a single cluster of unbleached chromatin patches, 15 nuclei with a cluster of unbleached chromatin patches but individual patches remote from the cluster. 13 nuclei with patches scattered over the nucleus. Standard deviations of the mean are indicated. Note the close similarity of the *RAC* curves for nuclei displaying pattern 1 and pattern 2 for both the 10% and the 2% fraction, while the curve for nuclei with pattern 3 differs from these curves.

median ($\langle d \rangle$)	pattern 1	pattern 2	pattern 3
10%	0.274 (0.183 - 0.376)	0.327 (0.184 - 0.416)	0.446 (0.308 - 0.612)
2%	0.196 (0.088 - 0.346)	0.240 (0.088 - 0.359)	0.358 (0.149 - 0.596)

Table 3.7: Median and Min-Max values of the mean relative distances for the 10% and 2% highest intensity chromatin fraction in nuclei after mitosis classified by the degree of clustering of their unbleached chromatin patches

The values were calculated from the *RAC* curves shown in Figure 3.46. Compare with the values printed Figure 3.44. For both fractions the values for pattern 1 and pattern 2 do not differ significantly ($p > 0.1$). The values for pattern 1 and pattern 3 and the values for pattern 2 and pattern 3 have a highly significant difference ($p \leq 0.001$).

As the *RAC* was normalized with the square root of the nuclear area, an inconsistent measurement of the nuclear area in the different cell cycle stages could lead to different values of the relative distances not caused by an actual change in the distribution of unbleached chromatin. In particular, in section 3.2.5 it was noted that in nuclei just before prophase a different threshold for the nuclear counterstain was selected than in nuclei immediately after bleaching, which caused the

unbleached region to appear more peripheral. As bleaching was presumably performed in G2 phase, the measured nuclear area was not expected to change after bleaching. To test, whether this was in fact the case, the ratio of the normalization factor (i.e. the square root of the area) for nuclei before prophase and after bleaching was calculated for all nuclei. The ratio ranged from 0.82 to 1.10 with a median value of 1.01. To test, whether the ratio differed significantly from 1 the sign test (Barlow 1989) was applied. There was no indication for a significant difference from 1 ($p = 0.19$) excluding the possibility that differences in the average relative distances of unbleached chromatin regions arose from an incorrect determination of the size of the nuclear area.

The results obtained by this autocorrelation analysis add quantitative support to the observation that the unbleached patches in nuclei after mitosis were more strongly distributed over the nucleus than the coherent unbleached regions in the mother nuclei (section 3.2.4).

4 Discussion

The goal of this thesis was to track DNA repair proteins and chromosomes in living cells to gain insight into nuclear dynamics during the cell cycle and during DNA-repair. To this end two modern light microscopical methods were adapted and applied: laser-UVA-microirradiation and laser-photobleaching in combination with 4D live cell imaging.

Laser-UVA-microirradiation was applied to living cells which had been sensitized to UVA light (Limoli and Ward 1993). This treatment induced DNA single-strand breaks (SSBs) and double-strand breaks (DSBs) in defined subnuclear sites. By irradiating distinct patterns in cell nuclei it was found that Rad51, a protein involved in the repair of DSBs by homologous recombination, accumulates at damaged sites. The kinetics of the accumulation of Rad51 at damaged sites was compared to that of Mre11, a protein involved in the repair of DSBs by homologous recombination and by non-homologous end joining. Rad51 forms nuclear foci during S-Phase. Using microirradiation it was examined, whether in damaged cells Rad51 redistributes from these S-Phase foci to the damaged sites. Finally, the accumulation of Rad51 in microirradiated patterns spanning whole nuclei was followed for several hours. As Rad51 binds to chromatin around sites of DSBs during homologous recombination repair, Rad51 was used to observe the dynamics of damaged chromatin during repair by homologous recombination.

By laser-photobleaching and 4D live cell imaging chromatin dynamics was followed in living HeLa cells expressing a GFP-tagged histone 2B construct (H2B-GFP, Kanda *et al.* 1998). The cells stably incorporated H2B-GFP into the nucleosomes. In interphase cell nuclei grid-like nuclear patterns were bleached into H2B-GFP. This way chromatin containing bleached H2B-GFP was marked and could be followed by live cell microscopy for several hours until GFP fluorescence had recovered due to the slow exchange of H2B-GFP. During the observation period the patterns remained unchanged indicating the absence of large-scale chromatin movements in this time. To follow chromosome arrangements from one cell cycle to the next, nuclei were photobleached in G2 except for a contiguous zone of unbleached chromatin at one nuclear pole. This zone was stably preserved until the onset of prophase, whereas the contiguity of unbleached chromosome segments was lost to a variable extent, when the metaphase plate was formed. Accordingly, chromatin patterns observed in daughter nuclei differed significantly from the mother cell nucleus showing that CT arrangements were stably maintained from mid G1 to late G2/early prophase, whereas major changes of CT neighborhoods occurred from one cell cycle to the next.

4.1 Technical advances in laser-microirradiation

Experimental setup

To study the recruitment of DNA repair factors to damaged sites and the kinetics of their accumulation laser-UVA-microirradiation of sensitized cells was employed. For this purpose I initially used a P.A.L.M. microdissection system, which had been integrated with a Zeiss LSM 410 confocal microscope. This particular setup offers for the first time the opportunity to start 4D observations directly after microirradiation. Although the opportunity was not used in this work, recently GFP-constructs of several proteins involved in HRR became available (Essers *et al.* 2002; Pellegrini *et al.* 2002). By the use of cells transfected with these constructs it will be

possible to directly follow the dynamics of the assembly of repair complexes at microirradiated sites in living cells.

During my stay at the University of Hiroshima I adapted a Zeiss LSM 510 with a UV-laser intended for imaging of UV-excitable dyes to be used for laser-UVA-microirradiation. In this system the selection of the irradiation positions and the control of the microirradiation process is integrated into the microscope control software. It allows the convenient storage and retrieval of the irradiated positions. An additional benefit of this system is that the only modifications to the microscope were software modifications. As the hardware is available in numerous cell biological labs or core facilities, microirradiation can be easily established at these sites. However, in its present state the software has only been tested on version 2.02 of the LSM 510 control software and has to be recompiled or even partially rewritten for the use with newer versions of the control software.

Both laser-microirradiation systems described here allow the induction of DNA strand breaks within subnuclear sites of living cells and the subsequent imaging by confocal microscopy. One apparent technical difference between the systems is that the P.A.L.M. system has a fixed UVA-laser, and the microscope stage has to be moved to select the position of the beam, whereas the UVA-laser of the LSM 510 setup can be moved over the whole field of view. An advantage of the fixed laser is that it should produce the smaller focus, as the optical quality of microscope objectives is best on the optical axis. However, in these experiments the difference was not noticeable. Another difference is that the control electronics of the P.A.L.M. system is separated from the control electronics of the confocal microscope, whereas in the LSM 510 setup microirradiation and confocal microscopy are integrated in one system. With an integrated system it will in principle be easier to run complex protocols involving multiple steps of irradiation and live cell imaging.

Sensitization to UVA light

In the experiments described here the sensitization of cellular DNA to UVA light was performed by incorporation of BrdU into the DNA either alone or in combination with staining with the dye Hoechst 33258. The combination of BrdU and Hoechst treatment has been characterized with respect to its sensitizing effect to UVA light (Limoli and Ward 1993). In contrast, there have been no measurements of the amount of DSBs induced by UVA-illumination of BrdU treated cells. There is, however, indirect evidence for the production of DSBs by UVA illumination of BrdU-sensitized cells: Illumination of BrdU treated cells with UVB light introduces DSBs (Krasin and Hutchinson 1978), and the same photochemical reaction probably takes place after illumination with UVA light (Limoli and Ward 1993). Furthermore, it has been shown here (section 3.1.2) that Rad51, a protein known to work in the repair of double-strand breaks, accumulates at UVA-illuminated sites in BrdU sensitized cell nuclei. Finally, a recent publication reports the accumulation of NBS1, which also works in the repair of DSBs, at UVA-illuminated sites in BrdU sensitized cell nuclei (Lukas *et al.* 2003).

It has to be noted that the incorporation of BrdU into cellular DNA and its combination with Hoechst staining by itself produces low levels of DNA damage without any UVA-illumination (Stetka and Carrano 1977; Natarajan *et al.* 1986). In the experiment presented here this effect was not apparent by the dynamics of Rad51, as no Rad51 accumulations were found in cells, which had been sensitized but not irradiated. However, the low level mutagenicity of the chemicals used for sensitization to UVA-light has to be considered in the design of a microirradiation experiment, and its effects as well as the effects of the light used for locating the cells have to be assessed in appropriate control experiments. Considering that the use of

possibly damaging chemicals should be kept low, BrdU (“alone”) sensitization should be preferred to BrdU / Hoechst sensitization. It has been reported that treatment of cells with Hoechst 33258 inhibits the condensation of constitutive heterochromatin (Vig and Willcourt 1998; Haaf and Schmid 2000). Furthermore, the energies required to produce Rad51 accumulations in BrdU sensitized cells were about 10 times higher than the energies required for BrdU / Hoechst sensitized cells. This means that unspecific damage due to stray light and incomplete protection from room light will pose a larger risk when the BrdU / Hoechst sensitization is used.

Estimation of the damage induced by laser-UVA-microirradiation

One limitation of the systems presented here is, that the exact UVA-dose in the laser focus and its efficiency in introducing DSBs is not known, which limits the comparability to irradiation experiments employing ionizing radiation. In theory the number of DSBs introduced by microirradiation can be calculated from the results of the measurements performed by Limoli and Ward (1993). Using the BrdU / Hoechst system, the authors found a sensitivity in Chinese hamster V79 cells of 5.1×10^{-9} DSBs per BrdU residue for a fluence of 1 Jm^{-2} of UVA light with a wavelength of 365 nm, when the cells had been incubated with $10 \text{ }\mu\text{g/ml}$ Hoechst for 10 min. This value was linearly dependent on the UVA-fluence, the percentage of BrdU substitution in DNA and the concentration of Hoechst. They also measured the percentage of BrdU-substitution after incubation with defined concentrations of BrdU and dThd and found that 7.5% of dThd in the DNA replicated in presence of $0.3 \text{ }\mu\text{M}$ BrdU and $2.5 \text{ }\mu\text{M}$ dThd (as used here) was substituted by BrdU. Under the assumption that the values measured by Limoli and Ward (1993) are likewise applicable to GM02063 cells and that the linear dependence on the UVA-fluence still holds even at the high fluences used applied in microirradiation, one can estimate the number of DSBs produced in the microirradiation experiments described here. As GM02063 cells are approximately triploid, incubation with the given concentrations of BrdU / dThd for one S-Phase leads to the incorporation of 200×10^6 BrdU residues into a G1 genome, which implies a sensitivity of $0.2 \text{ DSB} / \text{Jm}^{-2}$ of G1 cells incubated with $2 \text{ }\mu\text{g/ml}$ Hoechst 33258. Assuming $1000 \text{ }\mu\text{m}^3$ for the volume and $5 \text{ }\mu\text{m}$ for the height of GM02063 nuclei and neglecting the variable chromatin density within the nucleus, this calculation amounts to a yield of 1 DSB in a spot irradiated with 1 nJ of UVA-light (365 nm). The yield for the induction of SSBs is 100 times that for the induction of DSBs (Limoli and Ward 1993).

Clearly, the above assumptions are questionable, and some - like the even distribution of chromatin in the nucleus - are known to be wrong. However, a few Rad51 accumulations were found at sites irradiated with 1 nJ, and a substantial amount at sites irradiated with 10 nJ (Figure 3.7), hence the estimation corresponds reasonably well with the experiment. Nevertheless, a direct measurement of the DSB-yield of laser-UVA-microirradiation is desirable. This could be performed by the use of antibodies against phosphorylated histone H2AX (γ -H2AX). The histone variant H2AX is phosphorylated in chromatin around sites of DSBs (Rogakou *et al.* 1999). The size of the regions containing γ -H2AX around DSBs is around one megabase and γ -H2AX signals can be detected by immunofluorescence staining (see for example Figure 3.17). A γ -H2AX immunofluorescence signal at a nuclear position shows that at this position there are one or more DSBs (Rothkamm and Lobrich 2003). When nuclear positions are irradiated with energies that induce on average one DSB, some of the positions will show a γ -H2AX immunofluorescence signal and the other positions will not show a signal. Irradiation with lower energies will result in a lower fraction of irradiated sites with γ -H2AX signals. Increasing the

irradiation energy will result in a higher fraction of sites with signals until all irradiated positions show γ -H2AX. If the assumption is valid that a UV induced DSB in sensitized DNA results from a single photochemical event (Krasin and Hutchinson 1978; Limoli and Ward 1993) the number of DSBs at irradiated nuclear positions has a Poissonian distribution. Using this distribution and the measured fraction of γ -H2AX positive sites (p) the mean number of DSBs (μ) induced by a given irradiation energy can be calculated as

$$\mu = \ln \frac{1}{1-p}.$$

This calibration method has the limitation that it works only, if p is sufficiently different from one, i.e. at low irradiation energies. This limitation is a direct consequence of the fact that this method treats the γ -H2AX signals only as binary information ("yes/no"). It would be interesting to see, whether the intensity of a γ -H2AX signal relates to the number of DSBs, which contribute to it. Another limitation of the method is that it does not account for variations of chromatin density and incorporation of BrdU at the irradiated sites. Nevertheless this calibration method is far more direct than the above estimation of the irradiation energy.

The above discussion shows that a significant limitation of laser-UVA-microirradiation is that the damage introduced by this method is - at least presently - less well characterized than that introduced by "classical" irradiation methods as ionizing irradiation or UV irradiation. This limitation is avoided when localized irradiation is performed with ionizing radiation. Systems for this type of irradiation have been established. These systems employ either ultrasoft X-rays or focused or collimated ion beams (for an overview see Brenner 2000). One problem in the use of these systems is the identification of the cell nucleus and nuclear substructures to select the position of irradiation. The currently used systems solve this problem by imaging Hoechst-stained cells by fluorescence microscopy. This approach leads to images, in which the nuclei can be easily segmented, and allows automating the selection of the irradiation positions. On the other hand, staining with Hoechst dye and UV-excitation can induce unspecific damage and influence the cellular reaction to ionizing radiation. This problem does not appear when the nuclei are located by a contrast mode employing transmitted light, e.g. phase contrast. However, transmission light microscopy requires a light optical setup on both sides of the specimen limiting the space available for the irradiation beam. A setup, which solves this geometrical problem, has recently been established at the Munich 15 MV tandem ion accelerator in Garching. In future it is planned to upgrade this system to perform live cell microscopy in transmitted light and epifluorescence contrast modes. Therefore it will be possible to image GFP-tagged repair proteins after localized ion irradiation without compromising image quality. As ion accelerators are large facilities and measurement time at these facilities is always limited, the completion of this system will not abolish the need for UVA-laser-microirradiation. Rather it should be expected that the two systems complement each other.

Applications of laser-UV-microirradiation

Laser-UVA-microirradiation has been used to study local modifications at sites containing DNA breaks, such as the phosphorylation of the histone variant H2AX (Rogakou *et al.* 1999) or accumulation of repair proteins (Paull *et al.* 2000; Tashiro *et al.* 2000 and this work). The particular advantage of microirradiation compared to other forms of irradiation ("global irradiation") is, that the damage is limited to a small subnuclear site, whose location is known, so that a local response to DNA damage can be separated from a global response involving the whole nucleus. In this context

a recent report by Lukas *et al.* (2003) is particularly noteworthy. The authors investigated the dynamics of the checkpoint regulators NBS1 and Chk2. They found that after laser-UVA-microirradiation of cells sensitized with BrdU NBS1 localized to damaged sites. The mobility of NBS1 was reduced at these sites. In contrast, the diffusion of Chk2 through the nucleus was not impaired after the irradiation. However, phosphorylation of Chk2 at residue Threonine 68 was induced. Using a fusion protein of the core histone H2B, GFP and Chk2, which was stably integrated into nucleosomes, they showed that the phosphorylation of Chk2 occurs exclusively at damaged sites. This report therefore gives a mechanistical insight into the way a locally restricted modification can induce a global cellular response.

It is possible to change the type of DNA damage produced by laser-UVA-microirradiation by changing the sensitization method. For example, sensitization with psoralens (Cimino *et al.* 1985) instead of BrdU/Hoechst can be used to induce DNA-crosslinks in UVA-irradiated spots (Dardalhon and Averbeck 1988). In combination with microbeam experiments this approach was used to crosslink RNA present in centrioles (Peterson and Berns 1978) and nuclear DNA (Cremer *et al.* 1981b).

Laser-microirradiation experiments employing UVC light at 257 nm (Cremer *et al.* 1974) provided first evidence that chromosomes occupy spatially distinct territories within the interphase nucleus (Zorn *et al.* 1979) and allowed an indirect analysis of chromosome neighborhoods (Cremer *et al.* 1982b) and the orientation of chromosomes within the nucleus (Cremer *et al.* 1982a). In these experiments cells were microirradiated with UVC-light, and radioactive ³H-thymidine was added to the cell culture medium after irradiation. During the repair of the damage induced by microirradiation ³H-thymidine was incorporated into the repaired DNA. When the cells were fixed in the first postmitotic metaphase and subjected to autoradiography, the chromosomes hit by the UV-laser and the subchromosomal position of the hit could be identified.

4.2 Localization and dynamics of DNA-repair proteins

4.2.1 Rad51-accumulation at irradiated sites and its relation to Mre11

To test, whether Rad51 locates to sites of DNA damage during the repair of DSBs, primary human fibroblasts and cells of a fibroblast cell line were sensitized with BrdU or BrdU/Hoechst and microirradiated. After a post-irradiation incubation time the cells were fixed and immunostained for Rad51. In addition to Rad51 foci, which appear in cell nuclei during S-Phase and after ionizing radiation, microirradiated nuclei also contained larger and more intense Rad51 signals termed "accumulations" (see section 3.1.2, page 44). Rad51 accumulations were precisely located at the microirradiated nuclear positions and were a specific reaction to DNA damage. Rad51 accumulations colocalized with sites of single-stranded DNA (ssDNA), which were detected by immunostaining for BrdU incorporated into the nuclear DNA without a denaturation step. A denaturation step is necessary when BrdU incorporated into double-stranded DNA is to be detected in order to make the epitope of BrdU accessible to the antibody. In nuclei, which were immunostained for Mre11 after microirradiation, Mre11 accumulations were visible at microirradiated sites. Mre11 accumulations at microirradiated sites were visible already 0-5 minutes after microirradiation and the maximal number of accumulations was reached 5-10

minutes after microirradiation. In contrast, only a low percentage of the microirradiated cells carried Rad51 accumulations after 5-10 minutes, and percentage of microirradiated cells with Rad51 accumulations became maximal 20-30 minutes after microirradiation. Notably, at this time, in a significant proportion of the microirradiated nuclei Rad51 and Mre11 accumulations colocalized at the microirradiated sites.

The results of the laser-UVA-microirradiation experiments are in accord with previous reports but also differ in various aspects:

Accumulation of Rad51 at laser-UVA-microirradiated nuclear sites

After laser-UVA-microirradiation Rad51 accumulated at damaged nuclear sites. This experiment confirms earlier results from Raderschall *et al.* (1999) stating that Rad51 foci induced by γ -irradiation are formed at sites of ssDNA. These results correspond well with the model that Rad51 forms nucleoprotein filaments along long stretches of ssDNA at broken DNA ends to promote homologous pairing and strand exchange (Symington 2002). However, they are in conflict with a report by Nelms *et al.* (1998), who irradiated human fibroblast cell nuclei with ultrasoft X-rays through a striped mask (mean nuclear dose 100 Gray). After this treatment DSBs were clustered in stripes reflecting the striped pattern of the mask, and Mre11 but not Rad51 accumulated in these stripes.

Accumulation of Rad51 in G1 cells

After microirradiation with 100 nJ almost all cells showed Rad51 accumulations. This means that also G1 cells contain such accumulations. This finding is in conflict with reports that Rad51 performs repair in postreplicative chromatin (Tashiro *et al.* 2000), and that in DSB repair by gene conversion the preferred intact template strand is the sister chromatid as opposed to the homologous chromosome (Johnson and Jasin 2000). However, it has been shown that homologous recombination employing the homologous chromosome exists in mammalian cells (Zhu *et al.* 1992), although 2-3 orders of magnitude suppressed compared to the sister chromatid (Moynahan and Jasin 1997). Therefore it is possible that after microirradiation with high doses Rad51 accumulates also in G1 cells. As the Rad51 accumulations induced by microirradiation are remarkably stable (see section 3.1.8) and homologous chromosomes in human fibroblasts are usually not neighboring (Bolzer 2002), Rad51 accumulations in G1 cells may mark sites, where repair events are initiated but not completed.

Accumulation of Mre11 at microirradiated nuclear sites

The accumulation of Mre11 at laser-UVA-microirradiated nuclear sites is in accord with the report by Nelms *et al.* (1998), that in nuclei irradiated with patterned ultrasoft X-rays Mre11 accumulates in the damaged nuclear regions (see above). During DSB repair Mre11 forms a complex (MRN-complex) with the proteins Rad50 and NBS1 (Symington 2002). Recently, the redistribution of Rad50 (Paull *et al.* 2000) and NBS1 (Lukas *et al.* 2003) to damaged nuclear sites has been shown by laser-UVA-microirradiation. Together these data support the view that MRN-complexes are recruited to damaged sites after the induction of DSBs.

Sequential accumulation of Mre11 and Rad51

The finding that Mre11 accumulations in microirradiated cell nuclei appeared earlier than Rad51 accumulations is in accord with data reported by Paull *et al.* (2000), who found that after γ -irradiation of human fibroblasts radiation induced nuclear Rad50-foci appeared earlier than radiation induced Rad51 foci. The two experiments support a function of the MRN complex in DSB repair upstream of

Rad51. The results of the two experiments differ in that accumulation of Mre11 at microirradiated sites was completed 5-10 minutes after microirradiation and accumulation of Rad51 was completed 20-30 minutes after microirradiation, whereas the appearance of foci induced by γ -irradiation took several hours.

Colocalization of Rad51 and Mre11 at microirradiated nuclear sites

It was shown here that Mre11 accumulates at microirradiated sites and that Rad51 accumulations colocalize with Mre11 accumulations to a high degree. This finding is in conflict with the report by Nelms *et al.* (1998), who found that in human fibroblast cell nuclei irradiated with ultrasoft X-rays through a striped mask Mre11 accumulated in stripes reflecting the striped pattern of the mask, whereas the distribution of Rad51 showed no correlation with the stripe pattern. Furthermore, Paull *et al.* (2000) reported that foci of Rad51 and Rad50 induced by γ -irradiation did not appear together in the same nuclei of unsynchronized human fibroblast cells, and Mirzoeva *et al.* (2001) reported that γ -irradiation induced foci of Rad51 and Mre11 appeared in the same nuclei but did not colocalize.

Possible explanations for the conflicting results of experiments employing laser-UVA-microirradiation and ionizing radiation

The absence of Rad51 accumulations in damaged subnuclear areas produced by partial volume irradiation with ultrasoft X-rays (Nelms *et al.* 1998) can possibly be explained considering the dose response of Rad51 accumulation in laser-UVA-microirradiated cells (Figure 3.7). The percentage of cells showing Rad51 accumulations initially increases with higher UVA-doses up to 100 nJ, but decreases for even higher doses. Following the discussion in section 4.1 above, 100 nJ induce roughly 100 DSBs. Nelms *et al.* (1998) irradiated the cells with mean doses of 100 Gray leading to 1600 to 4000 DSBs per nucleus (Friedberg *et al.* 1995). This estimation indicates that the doses applied by Nelms *et al.* (1998) were too high to induce Rad51 accumulations at damaged DNA sites. It hints towards a mechanism, which at high amounts of DNA damage prevents the initiation of DNA repair by gene conversion either by switching to other repair mechanisms or by arresting the cell or inducing apoptosis.

In the experiments performed by Paull *et al.* (2000) and Mirzoeva *et al.* (2001) γ -irradiation with a dose of 12 Gray was applied. This dose induces 200 - 500 DSBs in a mammalian cell nucleus (Friedberg *et al.* 1995), an amount, which is comparable to the estimated damage induced in the laser-UVA-microirradiation experiments (1 - 500 DSBs, see Figure 3.7 and section 4.1). Nevertheless, the focus formation of Mre11/Rad50 observed in these experiments proceeded significantly slower than the accumulation at microirradiated sites reported here. Furthermore, in contrast to the microirradiation data, both groups did not find colocalizations of damage induced foci of Mre11/Rad50 with damage induced foci of Rad51. Two explanations for the observed differences, which are not necessarily mutually exclusive, have to be considered:

- A sequential assembly and disassembly of repair factors at single DSBs acting at different stages of the repair process
- The different distribution of lesions induced by laser-UVA-microirradiation and whole-cell γ -irradiation

Sequential assembly and disassembly of repair factors

It is well established that Mre11, Rad50 and NBS1 form a stable complex ("MRN-complex"), which is essential for the repair of DSBs, and, in fact, for the viability of vertebrate cell lines (Symington 2002). Rad51 interacts with several proteins of the Rad52 epistasis group, most notably with Rad52 and Rad54, and with

p53 and BRCA2. However, in FRAP experiments it was shown that Rad51 is stably associated with sites of DNA damage, whereas Rad52 and Rad54 rapidly and reversibly interact with these sites (Essers *et al.* 2002). This result supports the view that on the molecular level DNA repair factors do not all assemble in one large “repaosome” complex, but that the factors independently associate with damaged sites and dissociate from them (Symington 2002). The time, during which an individual factor binds to a damaged site, may vary between seconds and minutes depending on the factor’s function. Furthermore, binding sites that mediate the association of a factor with a damaged site may be available only at specific times in the repair process.

Such a dynamic model of protein binding at damaged sites could explain the absence of damage-induced foci containing Mre11/Rad50 and Rad51 after γ -irradiation. If MRN-complexes associate with a lesion induced by γ -irradiation and then dissociate before Rad51 nucleoprotein filaments assemble, no colocalization of the proteins will be detected. In contrast, all DSBs induced by microirradiation are concentrated in the irradiated spot. Within these spots there will be a faster disassembly of MRN and assembly of Rad51 at some lesions and a persistence of MRN at other lesions. At light-optical resolution this situation then appears as a colocalization of MRN and Rad51. This model would also explain the faster assembly of repair factors in microirradiation experiments as compared to γ -irradiation. Shortly after irradiation, only few damage induced foci of repair factors are detectable, but if these foci are all located at one irradiation spot, they appear as a protein accumulation. As this explanation is founded on the assumption that the lesions induced by laser-UVA-microirradiation are more clustered than the lesions induced by γ -irradiation, the effect of the two types of irradiation deserves a closer look.

Distribution of the lesions induced by laser-UVA-microirradiation and γ -irradiation

The current model of the effect of UV light on BrdU-sensitized cells is that absorption of a photon at a BrdU-site initiates a photochemical reaction at that site, which can result in the formation of a DSB (Krasin and Hutchinson 1978). As the absorption of a photon is a statistical process, DSBs induced by the UV-illumination are distributed randomly within the irradiated region, modulated by the local light intensity and the local density of BrdU-sites. (This discussion neglects possible secondary effects like changes in the chemical environment around individual BrdU-sites.) The DSBs induced by UVA-microirradiation are necessarily all clustered in the microirradiated region. The region hit by the microirradiation beam contains several Mbp of DNA (the beam hits a volume of several μm^3 , and the volume of a GM02063 nucleus with $\sim 9 \times 10^9$ bp DNA is about $1000 \mu\text{m}^3$). In a microirradiation spot with 10 DSBs the DSBs therefore have an average genomic distance of roughly 100 kb. The distance may actually be larger, as some DNA loops out and back inside the irradiated volume.

When cells are γ -irradiated, hits of γ -photons in each cell nucleus are statistically distributed over the whole nucleus. However, due to the high energy of the γ -photons, each hit has the potential to produce more than one lesion. It has been proposed that ionizing irradiation induces “regionally multiply damaged sites” or “locally multiply damaged sites” (LMDS) (Goodhead 1994; Rydberg 1996), in which DSBs are separated by short distances (0.1-2 kb of DNA) and are accompanied by a number of other lesions. Therefore, although it seems that the lesions induced by microirradiation are strongly clustered, on the nanometer scale lesions induced by γ -irradiation are possibly even more strongly clustered.

It has been argued that LMDS are particularly difficult to repair for cells and that the mechanisms active in their repair are different from those in the repair of single DSBs induced e.g. during DNA replication or by enzymatic treatment (Goodhead 1994; Rydberg 1996; Paull *et al.* 2000). An indication that this is in fact the case is given by the observation, that H2AX phosphorylation in response to DSBs is mainly performed by ATM after γ -irradiation (Andegeko *et al.* 2001; Burma *et al.* 2001) but by ATR after replicational stress (Ward and Chen 2001). As the damage in a microirradiated spot is less clustered than that in the putative LMDS, it is conceivable that microirradiation triggers mechanisms different from γ -irradiation. Such a difference could explain the different time scales and colocalizations observed in microirradiation and γ -irradiation experiments.

However, neither the process of damage formation by UVA-illumination of BrdU-sensitized cells nor the significance of the LMDS has been fully elucidated so far. Therefore, the conclusions drawn here are speculative. Further experiments are indicated to clarify differences and common features of damage induced by laser-UVA-microirradiation and damage induced by ionizing radiation. One such experiment would be to observe the extent and timing of the phosphorylation of H2AX in response to each of the two damage types in cell lines defective of ATM and in cell lines defective of ATR. As ATM and ATR phosphorylate H2AX in response to different inducers of DSBs, different responses of these cell lines to the two types of irradiation would indicate that the lesions induced by laser-UVA-microirradiation and ionizing radiation are repaired by distinct pathways.

4.2.2 Persistence of Rad51 S-Phase foci during repair

The significance of the scattered Rad51 S-Phase foci in undamaged cells is not clear at present. The foci are more abundant in tumor cells than in untransformed cells suggesting that they play a role in protecting those cells from apoptosis or promoting their genomic diversity (Raderschall *et al.* 2002b). Foci may indicate nuclear repair sites of endogenous DNA damage or they may represent Rad51 storage sites. If the Rad51 foci are storage sites, upon induction of DNA damage Rad51 protein should be redistributed from these sites to the damaged sites.

To test this hypothesis, GM02063 cells and primary human fibroblasts were microirradiated and fixed 0 - 40 minutes later. In fluorescence images of Rad51 immunostaining the fraction of cells with Rad51 foci and the fraction of cells with Rad51 accumulations were counted. (See section 3.1.2, page 44 for the distinction between foci and accumulations.) The analysis revealed that the fraction of irradiated cells with Rad51 foci is not changed by the irradiation up to 40 minutes after irradiation. This result are consistent with the view that Rad51 S-Phase foci are not pure storage sites, but that the Rad51 in these foci is required for some important cellular function. An alternative explanation is that the Rad51 foci are in fact storage sites, but that the amount of Rad51 required at damaged sites in these experiments was not sufficient to deplete the foci. The finding that Rad51 expression is not induced in response to DNA damage (Haaf *et al.* 1995; Haaf *et al.* 1999) provides evidence for a redistribution of Rad51 during DSB-repair. However, it does not clarify, whether redistributed Rad51 is released from Rad51 foci or originates from the nucleoplasmic pool of Rad51. Recently, Tarsounas *et al.* (2003) studied the nuclear distribution of Rad51 in cells, which express truncated BRCA2 lacking a nuclear localization signal. They reported that Rad51 focus formation in response to ionizing radiation was inhibited, but that the formation of Rad51 S-phase foci was unaltered in these cells. This finding shows that Rad51 S-Phase foci and damage-induced foci are formed by different mechanisms, one without and one with the help of BRCA2. It

is not clear, however, whether this means that Rad51 S-Phase foci are in fact storage sites.

Further experiments with higher irradiation doses and a quantitation of the fluorescence of Rad51 foci are required to clarify this question. As recently GFP-Rad51 constructs became available, whose nuclear structure and dynamics is comparable to that of endogenous Rad51 (Essers *et al.* 2002; Pellegrini *et al.* 2002), a possible redistribution of Rad51 from S-Phase foci to microirradiated nuclear sites could be observed *in vivo*.

4.2.3 Post-irradiation arrangements of Rad51 accumulations are stably maintained

To address the question of possible CT movements during the repair of DSBs, large-scale nuclear patterns were microirradiated. The patterns were found to persist up to 8 hours after irradiation (section 3.1.7). As Rad51 is accumulated at damaged DNA, the persistence of the patterns implies that the large scale CT arrangement during repair by gene conversion (involving Rad51) is stable. The finding that the formation of DSBs does not trigger changes of the large-scale CT order is in accordance with the finding that chromatin damaged by ultrasoft X-rays structured by a striped irradiation mask stays located to the irradiated stripes up to 5 hours (Nelms *et al.* 1998).

Although it has been shown that recombinational repair is a time consuming process that may last for several hours in human cells (van Rongen *et al.* 1993; Lange *et al.* 1997), the long persistence of Rad51 recruitment to sites of DSBs may indicate that repair of microbeam damage was initiated, but too severe to allow completion and subsequent resolution of repair complexes. This possibility, however, does not affect the conclusion that the formation of DSBs does not trigger a mechanism to establish a CT topology favorable for recombinational repair between homologous CTs.

Recombinational repair between homologous chromosomes requires spatial proximity between intact and damaged homologous DNA strands. This experiment demonstrates that these topological requirements are rarely fulfilled in HeLa cell nuclei. Evidence against homologous associations was previously reported for diploid human and avian cells (Cremer *et al.* 1993; Dietzel *et al.* 1998; Cremer and Cremer 2001; Habermann *et al.* 2001). This explains that recombinational repair in mammalian cells is largely limited to the S- and G2 phase of the cell cycle, when sister chromatids are available (Hendrickson 1997), and that for the repair of DSBs by gene conversion homologous recombination with sister chromatids is preferred to homologous recombination with homologous chromosomes (Moynahan and Jasin 1997).

4.2.4 The relation of Rad51 to the Interchromatin compartment

Localization of endogenous Rad51 foci in areas of low chromatin density

To investigate the localization of Rad51 with respect to the interchromatin compartment (IC), Rad51 immunostaining was performed on GM02063 cells and nuclear DNA was counterstained with propidium iodide. In a second experiment Rad51 immunostaining was performed in HeLa, in which a fluorescently labeled histone (H2B-GFP) acted as nuclear counterstain. Confocal microscopy of the Rad51 immunostaining signal in combination with DNA counterstain indicated that endogenous Rad51 foci were located in areas of low chromatin density implying

localization to the interchromatin compartment (IC). This finding is compatible with different functions of the Rad51 foci (see section 4.2.2 above). A role of the Rad51 foci as storage sites in the IC, which release repair factors upon DNA-damage, would parallel the role of PML bodies, which are also located in the IC (Bridger *et al.* 1998) and release several factors in response to environmental stress (Nefkens *et al.* 2003). Another possibility is that DNA-repair involving endogenous Rad51 foci takes place in the IC. For Rad51 mediated repair of DNA normally located in the interior of a CT this model requires local chromatin movements around damaged sites that expose the damaged DNA to the IC (as opposed to large-scale movements, see section 4.2.3 above). As proteins of the Rad52 epistasis group are able to freely diffuse through the nucleoplasm (Essers *et al.* 2002), there is no indication that exposure of damaged sites to the IC is necessary to allow binding of repair factors. However, a decondensed chromatin configuration might be required for the search of a homologous sequence required for gene conversion.

Localization of filaments of overexpressed GFP-Rad51

Acute ectopic overexpression of human Rad51 leads to the formation of large-scale filamental Rad51 structures (Raderschall *et al.* 2002a). Here, the relation of these structures to the IC was tested by confocal imaging of GFP-Rad51 and antibody staining against cotransfected NLS-vimentin. NLS-vimentin has been described to mark the IC (Bridger *et al.* 1998; Reichenzeller *et al.* 2000). It was observed that GFP-Rad51 filaments colocalize. In a second experiment confocal images of GFP-Rad51 filaments in combination with a nuclear counterstain were recorded. It was found that GFP-Rad51 is localized in regions of low chromatin density. These experiments indicate that GFP-Rad51 filaments mark the interchromatin compartment.

The stability of GFP-Rad51 association in the filaments was tested in a FRAP experiment. It was found that GFP-Rad51 did not recover 70 seconds after bleaching. When cells were transfected with GFP-Rad51 and imaged by confocal microscopy 48 hours later it was found that nuclei expressing GFP-Rad51 appeared in pairs, which were connected by a GFP-Rad51 filament. Both findings indicate that GFP-Rad51 is stably integrated in the GFP-Rad51 filaments.

Overexpression of human Rad51 reduces the sensitivity of cells to DNA damage (Raderschall *et al.* 2002a). It has not been tested, whether this effect is caused by the formation of the large-scale filamental structures of Rad51 in these cells. Rad51 has the ability to form nucleoprotein filaments on ssDNA (Shinohara *et al.* 1993; Benson *et al.* 1994). These filaments are not only kept together by the binding of Rad51 to ssDNA, but also by the self-association of Rad51 (Pellegrini *et al.* 2002). It is possible that the formation of Rad51 filaments, i.e. the extensive self-association of Rad51, is simply a side effect of the high concentration of Rad51 in overexpressing cells. The slow recovery of GFP-Rad51 fluorescence in the FRAP experiment presented here and the appearance of daughter cells linked by GFP-Rad51 filaments two days after transfection of GFP-Rad51 indicates that Rad51 filaments in overexpressing cells are very stable structures (FRAP and FLIP experiments with longer observation times and live cell observations of GFP-Rad51 transfected cells passing through mitosis are required to confirm this interpretation). Therefore, it seems unlikely that Rad51 molecules release from the structures to participate in DNA-repair.

The stability of GFP-Rad51 filaments poses a problem in the interpretation that they outline an interchromatin space: Does this space exist in absence of the filaments or do the filaments create it? The observation that they are flexible and respond to nuclear deformations in the highly mobile 293T cells argue for the view

that Rad51 filaments can be seen as strings, which are stable structures, but do not create a newly formed space around them. The colocalization of GFP-Rad51 filaments with filaments formed by NLS-vimentin and the colocalization of NLS-vimentin with several higher order nuclear structures (Bridger *et al.* 1998) shows that these filaments assemble in a preformed space, the IC, which is accessible to large protein structures.

4.3 Chromosome territory dynamics

For the *in vivo* observations of chromosome territory dynamics a 4D live cell imaging system was established at a Zeiss LSM410. As the control software of the LSM410 by itself does not record time series of image stacks, it was extended with a macro written in the macro language of the control software. The macro allows recording of time series of image stacks with up to three fluorescence channels in several regions of interest within one field of view. A feature, which to my knowledge is not provided by similar systems on the market, is that the system compensates for z-axis drift by measuring the z-position of the coverslip, on which the cells grow, by confocal imaging with reflected light. Although to date all major microscope manufacturers offer live cell imaging systems, this system is an example of how 4D live cell imaging can be established at a confocal microscope of the previous generation thus significantly reducing the cost for setting up a live cell imaging system.

Chromosome territory dynamics was observed in HeLa cells with histone H2B-GFP-tagged chromatin. Selected chromatin regions were photobleached and the unbleached regions were followed by live cell microscopy. Although this experimental approach is similar to that of fluorescence recovery after photobleaching (FRAP) experiments, it differs in the object of interest. In contrast to the situation in FRAP-experiments the mobility of the GFP-tagged protein at the molecular level was already known and very low (Kimura and Cook 2001). In these experiments movements of higher order structures marked by stable integration of the protein were followed.

To compare the quality of the images recorded for the experiments reported here with images from other live cell experiments, the response of the photomultiplier of the LSM410 was calibrated. In images of unbleached nuclei on average 200 photons contributed to a nuclear pixel yielding a signal to noise ratio (S/N) of 14. In daughter cells pixels in the unbleached patches contained on average the signal from 50 photons (S/N = 7). The pixel size was between 100 and 200 nm in lateral and between 800 and 1000 nm in axial direction. Image stacks with 256x256 or 512x512 pixels and 15 to 25 sections were recorded with time intervals of 15 to 30 minutes. The observation period was up to 26 hours.

4.3.1 CT dynamics in interphase nuclei

In vivo observation of bleached cross-stripe patterns produced in histone H2B-GFP-tagged chromatin at different interphase stages were maintained during fluorescence recovery for 1-2 hours (section 3.2.3). Zones of unbleached chromatin produced at nuclear poles of late S or G2 nuclei retained their location and shape until the onset of mitosis (section 3.2.4). These data support the absence of large-scale CT movements in interphase, and is fully consistent with results from Abney *et al.* (1997) who demonstrated the local persistence of bleached spots in dihydroethidium-stained chromatin of mammalian cells over at least one hour.

The data is consistent with live cell observations of individual CTs (Schermelleh 2003; see also Walter *et al.* 2003b). For these observations chromosomal DNA was labeled by scratch replication labeling (SRL): cells on coverslips were transferred to medium containing fluorescently labeled dUTPs and the layer of cells was scratched with a hypodermic needle. This procedure led to transient damage of cell membranes in cells along the scratch path, and allowed the uptake of labeled dUTP and incorporation into replicating DNA (Schermelleh *et al.* 2001). In the following cell divisions labeled and unlabeled chromatids were randomly passed on to the daughter cells, and after several days the cells contained only one or few labeled CTs. Cells with fluorescently labeled CTs were followed by live cell microscopy for up to a whole cell cycle. A quantitative evaluation of the distances of individual CTs from the center of the nucleus and the distances between pairs of CTs revealed changes of CT positions on the order of several μm during early G1 phase. Thereafter, CT positions were constrained within a range of $\sim 1 \mu\text{m}$ from later G1 until the end of G2. These observations independently show the stability of CT positions in interphase at a higher resolution than that provided by the bleaching approach.

Live cell observations of GFP-labeled centromeres in HeLa cells also supported a stable arrangement of CTs during interphase (Shelby *et al.* 1996). In these experiments occasional movements of individual or small groups of centromeres at rates of up to 7-10 $\mu\text{m}/\text{h}$ were observed. It is possible that in the experiments presented in sections 3.2.3 and 3.2.4 such occasional movements happened in a part of the nucleus, which was not covered by the cross-stripe pattern (section 3.2.3) or completely bleached (section 3.2.4). In this case a movement would not be detectable.

The results presented here are compatible with the observation of diffusional movements of the intensity gravity centers of subchromosomal foci and chromosomes in living cells (e.g. Zink *et al.* 1998; Bornfleth *et al.* 1999; Edelmann *et al.* 2001; Chubb *et al.* 2002), as those movements appear on a smaller scale. Diffusional movements of chromatin, could, however, have contributed to the blurring of the bleached stripes and the apparent fluorescence recovery in addition to the exchange of bleached H2B-GFP from nucleosomes (Kimura and Cook 2001).

The stability of CT arrangements during interphase in cycling HeLa cells does not contradict possible chromosome movements in a functional context. Volpi *et al.* (2000) found that the major histocompatibility complex gene cluster on human chromosome #6 looped out from the CT #6 in response to upregulation by interferon-gamma.

In contrast to the relative stability of CTs during most of interphase and in accord with the observations by Schermelleh (2003) described above several groups found indications for CT movements in early G1. Csink and Henikoff (1998) described heterochromatic associations involving large-scale reorganization of chromosomes during G1 in *Drosophila* larval nuclei. In a study of painted CTs in fixed human diploid fibroblast nuclei Bridger *et al.* (2000) found that the final locations of CT#18 were established during the first 2 - 4 hours of G1. Furthermore, evidence for an increased mobility during early G1 compared to later interphase stages was presented for engineered GFP-labeled chromosome sites in living CHO cells (Tumbar and Belmont 2001).

4.3.2 Changes of CT order from one cell cycle to the next

Similarities of CT arrangements in daughter nuclei as well as changes as a result of mitosis were analyzed by tracking of unbleached chromatin regions through mitosis. Coherent unbleached chromatin zones produced in mother nuclei during late

S/G2 retained their position till early prophase. In prophase the unbleached chromatin became locally condensed into several unbleached chromosome segments. In daughter nuclei these segments were recognized as locally decondensed chromatin patches. The observation that locally constrained chromatin movements are sufficient for the transition of interphase into mitotic chromosomes and vice versa are consistent with findings reported by other groups (Manders *et al.* 1999; Lemke *et al.* 2002). The arrangements of the unbleached patches in the daughter nuclei differed significantly from the arrangement in the mother nucleus. Daughter nuclei with distantly located patches of unbleached chromatin demonstrate that mitosis is of major importance to explain the variability of CT arrangements in interphase nuclei.

Symmetry of the bleaching patterns in daughter nuclei but not in clones in the 4-cell stage

As a result of perfectly symmetrical chromatid movements during anaphase/telophase one would expect daughter nuclei with a translational or mirror-like symmetry of their CT arrangements. In the chromatin bleaching experiments presented here pairs of daughter nuclei often showed a notable symmetry of the labeled higher order chromatin structures, but this symmetry was not perfect and pairs without an obvious translational or mirror like symmetry were noted. Failure to achieve a symmetrical CT distribution may result from an imperfect symmetry of chromatid movements during anaphase. The finding that CT movements are significantly more pronounced in nuclei in early G1 compared to mid G1 to late G2 provides an additional possibility for movements, which disturb this symmetry (see above, Schermelleh 2003; Walter *et al.* 2003b). The relative symmetry observed in daughter cells fits well to the results from experiments with 2-cell clones and 4-cell clones, in which CTs were painted by FISH (Köhler 2002; Walter *et al.* 2003b). In 2-cell clones a symmetrical arrangement of the painted CTs was noted, although in some cases the arrangement deviated from a symmetrical arrangement. In 4-cell clones it was possible to identify two pairs of nuclei with symmetrically arranged CTs, but the CT arrangement in one pair was not symmetrical to that in the other pair. This finding supports the view that CT positions are rather symmetrical in daughter nuclei of the same cell, but change from one cell cycle to the next.

Conflicting data

Nagele *et al.* (1995; 1999) claimed that chromosomes in mitotic rosettes have a highly ordered, reproducible arrangement. In principle this finding is compatible with changing CT neighborhoods in subsequent cell cycles as found in this work, if one assumes that during prometaphase the chromosomes move to distinct positions in the rosette, but leave these positions during anaphase to early G1. However, this interpretation is in conflict with the rather symmetrical arrangement of CTs in sister nuclei reported here and elsewhere (Heitz 1931; Sun and Yokota 1999, Walter, 2003 #927; Habermann *et al.* 2001). Furthermore, direct evidence against Nagele's hypothesis was presented by Allison and Nestor (1999) and recently by Bolzer (2002) using M-FISH experiments, in which more than 70% of the CTs in each nucleus were identified simultaneously. These authors found "relatively random" relative positions of chromosomes in prometaphase rosettes of several human cell types.

Recently, Gerlich *et al.* (2003) reported experiments similar to the ones shown here with apparently contrary results. The authors observed nuclei of rat NRK cells expressing H2B-CFP and H2B-YFP. They bleached the YFP-signal in one half of each nucleus, left the CFP unbleached as a nuclear counterstain and followed the

cells through mitosis. In daughter cells the “global pattern” of the mother cell was restored, i.e. it was possible to identify two large regions in the nucleus; one containing bleached YFP, the other one containing unbleached YFP. The authors analyzed the influence of the direction of the spindle axis relative to the labeling boundary and found similar results for nuclei bleached parallel to and perpendicular to the spindle axis. This was in conflict with a computer model developed by the authors, which predicted a conservation of the bleached pattern in nuclei bleached parallel to the spindle axis, but a randomization in nuclei bleached perpendicular to the axis. To explain this conflict, they proposed that the timing of the separation of the sister chromatids at the onset of anaphase determines the position of a chromosome in the G1 daughter cell along the spindle axis. An experiment, in which they tracked GFP-tagged centromeres through mitosis supported this explanation. The authors hypothesized that the time, at which the sister chromatids of a particular chromosome separate, is determined by the content of constitutive heterochromatin of that chromosome. To test their hypothesis they inhibited the formation of constitutive heterochromatin by incubating cells with 10 µg/ml Hoechst 33258 for 20 h. They found that after this treatment patterns bleached parallel to the spindle axis were restored after mitosis but patterns bleached perpendicular to the spindle axis were randomized.

At present it is not clear, how the conflict between my and Gerlich’s data can be resolved. It has been proposed that the observed differences are a result of interpretation (Bickmore and Chubb 2003; Williams and Fisher 2003). In this work a small portion of the nucleus was left unbleached, and changes of this pattern are relatively easy to detect. Still, 40% of the daughter nuclei had showed a clustering of the unbleached chromatin and in 30% of the nuclei only few unbleached patches were distant from a cluster of unbleached chromatin. On the other hand, the daughter nuclei observed by Gerlich *et al.* did not show a straight border between bleached and unbleached YFP, and occasionally small patches of unbleached YFP were encircled by bleached YFP. To compare the extent of clustering of the unbleached chromatin in the two experiments, a quantitative evaluation of both experiments with the same method has to be performed. Such a method has been applied here: the *RAC*. It has to be tested, whether comparisons of the two different experimental setups (small unbleached patch - nuclear half bleached) with the *RAC* yield meaningful results. Likewise, it would be interesting to compare the quality of the recorded images in both experiments, i.e. resolution and S/N. In live cell microscopy there is always a tradeoff between cell viability and image quality. Gerlich *et al.* recorded two H2B-fusion proteins with different colors, one partially bleached and one unbleached, acting as a nuclear counterstain. The presence of a nuclear counterstain has the advantage that the upper and lower border of the nucleus can be segmented and a full 3D-evaluation can be performed (although Gerlich *et al.* did not do this). Another advantage is that the counterstain is a reference to distinguish bleached chromatin from chromatin in areas of low DNA density as done by Gerlich *et al.* However, the need to record two fluorescence signals might have lead Gerlich *et al.* to record images of lower quality than recorded for this work. In these images details like small patches of bleached chromatin within an area of unbleached chromatin could become obscured.

Conservation of radial, but not side-by-side, CT order

The variability of CT order in HeLa cell nuclei prompts the question, whether CTs may be arranged in an entirely random fashion in this cell line, but this is clearly not the case. In agreement with the non-random radial distribution pattern of the gene-dense CTs #19 and gene-poor CTs #18, which was demonstrated in diploid

nuclei of lymphocytes and lymphoblastoid cells from man and other primates (Croft *et al.* 1999; Cremer *et al.* 2001; Tanabe *et al.* 2002a; Tanabe *et al.* 2002b), a more interior location of gene-dense chromosome 19 material compared to chromosome 18 material was found in HeLa cell nuclei despite of rearrangements involving these chromosomes (Walter *et al.* 2003b).

A conserved radial distribution of CTs in HeLa cells would implicate that the unbleached chromatin, which in mother nuclei lies at the nuclear periphery, also has a preferentially peripheral location in the daughter nuclei. The results of a quantitative evaluation neither support nor rule out a conservation of the radial distribution of the unbleached chromatin regions through mitosis (section 3.2.5). It must be considered that, as the cells lacked a nuclear counterstain for the total chromatin, the evaluation was only performed on mid-nuclear sections. Therefore, probably most of the patches in the interior were counted, whereas unbleached patches, which were close to the upper or lower nuclear border, escaped detection. This introduces a bias against a peripheral localization of the unbleached patches. For a final answer to the question, whether the peripheral unbleached chromatin preferentially localizes at the nuclear periphery after mitosis a 3D evaluation on cells, which have a nuclear counterstain for the total chromatin, has to be performed.

A second quantitative evaluation employing an autocorrelation method (“*RAC*”) supported the variable distribution of the unbleached patches in daughter nuclei (section 3.2.6), but was likewise only performed on mid-nuclear sections. Considering that an evaluation on mid-nuclear sections cannot clarify the radial distribution of unbleached chromatin in the daughter cells, one might question, whether an evaluation of chromatin clustering with the same limitation is valid. However, additional unbleached patches located above or below the evaluated mid-nuclear sections would contribute to the *RAC* at larger relative distances and therefore enhance the apparent spreading of unbleached chromatin in daughter nuclei. In the bleached mother nuclei all unbleached chromatin is located in one patch, and the extension to a 3D evaluation would predominantly add contributions to small distances. The 2D evaluation on mid-nuclear sections is therefore a conservative estimate for the degree of clustering of the unbleached chromatin and clearly supports the view that CT order changes from one cell cycle to the next.

Literature

- Abney, J. R., B. Cutler, M. L. Fillbach, D. Axelrod and B. A. Scalettar (1997). "Chromatin dynamics in interphase nuclei and its implications for nuclear structure." *J Cell Biol* **137**(7): 1459-68.
- Allison, D. C. and A. L. Nestor (1999). "Evidence for a relatively random array of human chromosomes on the mitotic ring." *J Cell Biol* **145**(1): 1-14.
- Andegeko, Y., L. Moyal, L. Mittelman, I. Tsarfaty, Y. Shiloh and G. Rotman (2001). "Nuclear retention of ATM at sites of DNA double strand breaks." *J Biol Chem* **276**(41): 38224-30.
- Arnison, M. R., C. J. Cogswell, N. I. Smith, P. W. Fekete and K. G. Larkin (2000). "Using the Hilbert transform for 3D visualization of differential interference contrast microscope images." *J Microsc* **199**(Pt 1): 79-84.
- Ausio, J. and D. W. Abbott (2002). "The many tales of a tail: carboxyl-terminal tail heterogeneity specializes histone H2A variants for defined chromatin function." *Biochemistry* **41**(19): 5945-9.
- Axelrod, D., D. E. Koppel, J. Schlessinger, E. Elson and W. W. Webb (1976). "Mobility measurement by analysis of fluorescence photobleaching recovery kinetics." *Biophys J* **16**(9): 1055-69.
- Barlow, R. (1989). *Statistics*. Chichester, UK, Wiley.
- Baumann, P., F. E. Benson and S. C. West (1996). "Human Rad51 protein promotes ATP-dependent homologous pairing and strand transfer reactions in vitro." *Cell* **87**(4): 757-66.
- Benson, F. E., A. Stasiak and S. C. West (1994). "Purification and characterization of the human Rad51 protein, an analogue of E. coli RecA." *Embo J* **13**(23): 5764-71.
- Berns, M. W. (1978). "The laser microbeam as a probe for chromatin structure and function." *Methods Cell Biol* **18**: 277-94.
- Bezzubova, O., A. Shinohara, R. G. Mueller, H. Ogawa and J. M. Buerstedde (1993). "A chicken RAD51 homologue is expressed at high levels in lymphoid and reproductive organs." *Nucleic Acids Res* **21**(7): 1577-80.
- Bickmore, W. A. and J. R. Chubb (2003). "Chromosome position: now, where was I?" *Curr Biol* **13**(9): R357-9.
- Bischof, O., S. H. Kim, J. Irving, S. Beresten, N. A. Ellis and J. Campisi (2001). "Regulation and localization of the Bloom syndrome protein in response to DNA damage." *J Cell Biol* **153**(2): 367-80.
- Bishop, D. K. (1994). "RecA homologs Dmc1 and Rad51 interact to form multiple nuclear complexes prior to meiotic chromosome synapsis." *Cell* **79**(6): 1081-92.
- Bolzer, A. (2002). Analyse der Chromosomenverteilung in menschlichen Fibroblasten mittels 3D-Vielfarben Fluoreszenz in situ Hybridisierung. *Department Biologie II, Lehrstuhl für Anthropologie und Humangenetik*. München, LMU München.
- Bornfleth, H., P. Edelmann, D. Zink, T. Cremer and C. Cremer (1999). "Quantitative motion analysis of subchromosomal foci in living cells using four-dimensional microscopy." *Biophys J* **77**(5): 2871-86.
- Boveri, T. (1909). "Die Blastomerenkerne von *Ascaris megalocephala* und die Theorie der Chromosomenindividualität." *Archiv für Zellforschung* **3**: 181-268.
- Boyle, S., S. Gilchrist, J. M. Bridger, N. L. Mahy, J. A. Ellis and W. A. Bickmore (2001). "The spatial organization of human chromosomes within the nuclei of normal and emerin-mutant cells." *Hum Mol Genet* **10**(3): 211-9.
- Brakenhoff, G. J., P. Blom and P. Barends (1979). "Confocal scanning light microscopy with high aperture immersion lenses." *J Microsc* **117**: 219-232.
- Brenner, D. J. (2000). "Extended Abstracts; Proceedings of the 4th International Workshop: Microbeam Probes of Cellular Radiation Response; Killiney Bay, Dublin, Ireland, July 17-18, 1999." *Radiat Res* **153**: 200-238.
- Bressan, D. A., B. K. Baxter and J. H. Petrini (1999). "The Mre11-Rad50-Xrs2 protein complex facilitates homologous recombination-based double-strand break repair in *Saccharomyces cerevisiae*." *Mol Cell Biol* **19**(11): 7681-7.

- Bridger, J. M., S. Boyle, I. R. Kill and W. A. Bickmore (2000). "Re-modelling of nuclear architecture in quiescent and senescent human fibroblasts." *Curr Biol* **10**(3): 149-52.
- Bridger, J. M., H. Herrmann, C. Munkel and P. Lichter (1998). "Identification of an interchromosomal compartment by polymerization of nuclear-targeted vimentin." *J Cell Sci* **111**(Pt 9): 1241-53.
- Buchhop, S., M. K. Gibson, X. W. Wang, P. Wagner, H. W. Sturzbecher and C. C. Harris (1997). "Interaction of p53 with the human Rad51 protein." *Nucleic Acids Res* **25**(19): 3868-74.
- Burma, S., B. P. Chen, M. Murphy, A. Kurimasa and D. J. Chen (2001). "ATM phosphorylates histone H2AX in response to DNA double-strand breaks." *J Biol Chem* **276**(45): 42462-7.
- Carmo-Fonseca, M., L. Mendes-Soares and I. Campos (2000). "To be or not to be in the nucleolus." *Nat Cell Biol* **2**(6): E107-12.
- Carney, J. P., R. S. Maser, H. Olivares, E. M. Davis, M. Le Beau, J. R. Yates, 3rd, L. Hays, W. F. Morgan and J. H. Petrini (1998). "The hMre11/hRad50 protein complex and Nijmegen breakage syndrome: linkage of double-strand break repair to the cellular DNA damage response." *Cell* **93**(3): 477-86.
- Chen, F., A. Nastasi, Z. Shen, M. Brenneman, H. Crissman and D. J. Chen (1997). "Cell cycle-dependent protein expression of mammalian homologs of yeast DNA double-strand break repair genes Rad51 and Rad52." *Mutat Res* **384**(3): 205-11.
- Chen, J. J., D. Silver, S. Cantor, D. M. Livingston and R. Scully (1999). "BRCA1, BRCA2, and Rad51 operate in a common DNA damage response pathway." *Cancer Res* **59**(7 Suppl): 1752s-1756s.
- Chubb, J. R., S. Boyle, P. Perry and W. A. Bickmore (2002). "Chromatin motion is constrained by association with nuclear compartments in human cells." *Curr Biol* **12**(6): 439-45.
- Cimino, G. D., H. B. Gamper, S. T. Isaacs and J. E. Hearst (1985). "Psoralens as photoactive probes of nucleic acid structure and function: organic chemistry, photochemistry, and biochemistry." *Annu Rev Biochem* **54**: 1151-93.
- Cole, N. B., C. L. Smith, N. Sciaky, M. Terasaki, M. Edidin and J. Lippincott-Schwartz (1996). "Diffusional mobility of Golgi proteins in membranes of living cells." *Science* **273**(5276): 797-801.
- Connelly, J. C. and D. R. Leach (2002). "Tethering on the brink: the evolutionarily conserved Mre11-Rad50 complex." *Trends Biochem Sci* **27**(8): 410-8.
- Cornforth, M. N., K. M. Greulich-Bode, B. D. Loucas, J. Arsuaga, M. Vazquez, R. K. Sachs, M. Bruckner, M. Molls, P. Hahnfeldt, L. Hlatky and D. J. Brenner (2002). "Chromosomes are predominantly located randomly with respect to each other in interphase human cells." *J Cell Biol* **159**(2): 237-44.
- Cremer, C. and T. Cremer (1978). "Considerations on a laser-scanning-microscope with high resolution and depth of field." *Microsc Acta* **81**(1): 31-44.
- Cremer, C., T. Cremer and G. Jabbur (1981a). "Laser-UV-microirradiation of Chinese hamster cells: the influence of the distribution of photolesions on unscheduled DNA synthesis." *Photochem Photobiol* **33**(6): 925-8.
- Cremer, C., C. Zorn and T. Cremer (1974). "An ultraviolet laser microbeam for 257 nm." *Microsc Acta* **75**(4): 331-7.
- Cremer, M., L. Schermelleh, I. Solovei and T. Cremer (2003). Chromosomal arrangement during different phases of cell cycle. *Encyclopedia of the human genome*, Macmillan Publishers Ltd, Nature Publishing Group.
- Cremer, M., J. von Hase, T. Volm, A. Brero, G. Kreth, J. Walter, C. Fischer, I. Solovei, C. Cremer and T. Cremer (2001). "Non-random radial higher-order chromatin arrangements in nuclei of diploid human cells." *Chromosome Res* **9**(7): 541-67.
- Cremer, T. and C. Cremer (2001). "Chromosome territories, nuclear architecture and gene regulation in mammalian cells." *Nat Rev Genet* **2**(4): 292-301.
- Cremer, T., C. Cremer, H. Baumann, E. K. Luedtke, K. Sperling, V. Teuber and C. Zorn (1982a). "Rabl's model of the interphase chromosome arrangement tested in Chinese

- hamster cells by premature chromosome condensation and laser-UV- microbeam experiments." *Hum Genet* **60**(1): 46-56.
- Cremer, T., C. Cremer, T. Schneider, H. Baumann, L. Hens and M. Kirsch-Volders (1982b). "Analysis of chromosome positions in the interphase nucleus of Chinese hamster cells by laser-UV-microirradiation experiments." *Hum Genet* **62**(3): 201-9.
- Cremer, T., G. Kreth, H. Koester, R. H. Fink, R. Heintzmann, M. Cremer, I. Solovei, D. Zink and C. Cremer (2000). "Chromosome territories, interchromatin domain compartment, and nuclear matrix: an integrated view of the functional nuclear architecture." *Crit Rev Eukaryot Gene Expr* **10**(2): 179-212.
- Cremer, T., A. Kurz, R. Zirbel, S. Dietzel, B. Rinke, E. Schrock, M. R. Speicher, U. Mathieu, A. Jauch, P. Emmerich and et al. (1993). "Role of chromosome territories in the functional compartmentalization of the cell nucleus." *Cold Spring Harb Symp Quant Biol* **58**: 777-92.
- Cremer, T., S. P. Peterson, C. Cremer and M. W. Berns (1981b). "Laser microirradiation of Chinese hamster cells at wavelength 365 nm: effects of psoralen and caffeine." *Radiat Res* **85**(3): 529-43.
- Critchlow, S. E. and S. P. Jackson (1998). "DNA end-joining: from yeast to man." *Trends Biochem Sci* **23**(10): 394-8.
- Croft, J. A., J. M. Bridger, S. Boyle, P. Perry, P. Teague and W. A. Bickmore (1999). "Differences in the localization and morphology of chromosomes in the human nucleus." *J Cell Biol* **145**(6): 1119-31.
- Csink, A. K. and S. Henikoff (1998). "Large-scale chromosomal movements during interphase progression in *Drosophila*." *J Cell Biol* **143**(1): 13-22.
- D'Amours, D. and S. P. Jackson (2002). "The Mre11 complex: at the crossroads of dna repair and checkpoint signalling." *Nat Rev Mol Cell Biol* **3**(5): 317-27.
- Dardalhon, M. and D. Averbeck (1988). "Induction and removal of DNA interstrand cross-links in V-79 Chinese hamster cells measured by hydroxylapatite chromatography after treatments with bifunctional furocoumarins." *Int J Radiat Biol* **54**(6): 1007-20.
- Denk, W., D. W. Piston and W. W. Webb (1995). Two-Photon Molecular Excitation in Laser-Scanning Microscopy. *Handbook of Biological Confocal Microscopy*. J. B. Pawley. New York, Plenum Press.
- Dietzel, S., A. Jauch, D. Kienle, G. Qu, H. Holtgreve-Grez, R. Eils, C. Munkel, M. Bittner, P. S. Meltzer, J. M. Trent and T. Cremer (1998). "Separate and variably shaped chromosome arm domains are disclosed by chromosome arm painting in human cell nuclei." *Chromosome Res* **6**(1): 25-33.
- Dundr, M. and T. Misteli (2001). "Functional architecture in the cell nucleus." *Biochem J* **356**(Pt 2): 297-310.
- Edelmann, P., H. Bornfleth, D. Zink, T. Cremer and C. Cremer (2001). "Morphology and dynamics of chromosome territories in living cells." *Biochim Biophys Acta* **1551**(1): M29-39.
- Essers, J., A. B. Houtsmuller, L. van Veelen, C. Paulusma, A. L. Nigg, A. Pastink, W. Vermeulen, J. H. Hoeijmakers and R. Kanaar (2002). "Nuclear dynamics of RAD52 group homologous recombination proteins in response to DNA damage." *Embo J* **21**(8): 2030-7.
- Featherstone, C. and S. P. Jackson (1999). "Ku, a DNA repair protein with multiple cellular functions?" *Mutat Res* **434**(1): 3-15.
- Ferguson, M. and D. C. Ward (1992). "Cell cycle dependent chromosomal movement in pre-mitotic human T- lymphocyte nuclei." *Chromosoma* **101**(9): 557-65.
- Figgitt, M. and J. R. Savage (1999). "Interphase chromosome domain re-organization following irradiation." *Int J Radiat Biol* **75**(7): 811-7.
- Friedberg, E. C., G. C. Walker and W. Siede (1995). *DNA repair and mutagenesis*. Washington, American Society for Microbiology.
- Fujimori, A., S. Tachiiri, E. Sonoda, L. H. Thompson, P. K. Dhar, M. Hiraoka, S. Takeda, Y. Zhang, M. Reth and M. Takata (2001). "Rad52 partially substitutes for the Rad51 paralog XRCC3 in maintaining chromosomal integrity in vertebrate cells." *Embo J* **20**(19): 5513-20.
- Gall, J. G. (2000). "Cajal bodies: the first 100 years." *Annu Rev Cell Dev Biol* **16**: 273-300.
- Gasser, S. M. (2002). "Visualizing chromatin dynamics in interphase nuclei." *Science* **296**(5572): 1412-6.

- Gerlich, D., J. Beaudouin, B. Kalbfuss, N. Daigle, R. Eils and J. Ellenberg (2003). "Global Chromosome Positions Are Transmitted through Mitosis in Mammalian Cells." Cell **112**(6): 751-64.
- Goldberg, M., M. Stucki, J. Falck, D. D'Amours, D. Rahman, D. Pappin, J. Bartek and S. P. Jackson (2003). "MDC1 is required for the intra-S-phase DNA damage checkpoint." Nature **421**(6926): 952-6.
- Golub, E. I., R. C. Gupta, T. Haaf, M. S. Wold and C. M. Radding (1998). "Interaction of human rad51 recombination protein with single-stranded DNA binding protein, RPA." Nucleic Acids Res **26**(23): 5388-93.
- Gonzalez, R. C. and W. P. (1987). Digital image processing. Reading, Addison-Wesley.
- Goodhead, D. T. (1994). "Initial events in the cellular effects of ionizing radiations: clustered damage in DNA." Int J Radiat Biol **65**(1): 7-17.
- Greulich, K. O. and G. Leitz (1994). "Light as microsensor and micromanipulator: laser microbeams and optical tweezers." Experimental Technique of Physics **40**(1): 1-14.
- Guo, A., P. Salomoni, J. Luo, A. Shih, S. Zhong, W. Gu and P. Paolo Pandolfi (2000). "The function of PML in p53-dependent apoptosis." Nat Cell Biol **2**(10): 730-6.
- Haaf, T., E. I. Golub, G. Reddy, C. M. Radding and D. C. Ward (1995). "Nuclear foci of mammalian Rad51 recombination protein in somatic cells after DNA damage and its localization in synaptonemal complexes." Proc Natl Acad Sci U S A **92**(6): 2298-302.
- Haaf, T., E. Raderschall, G. Reddy, D. C. Ward, C. M. Radding and E. I. Golub (1999). "Sequestration of mammalian Rad51-recombination protein into micronuclei." J Cell Biol **144**(1): 11-20.
- Haaf, T. and M. Schmid (2000). "Experimental condensation inhibition in constitutive and facultative heterochromatin of mammalian chromosomes." Cytogenet Cell Genet **91**(1-4): 113-23.
- Haber, J. E. (1998). "The many interfaces of Mre11." Cell **95**(5): 583-6.
- Haber, J. E. (1999). "DNA repair. Gatekeepers of recombination." Nature **398**(6729): 665, 667.
- Habermann, F. A., M. Cremer, J. Walter, G. Kreth, J. von Hase, K. Bauer, J. Wienberg, C. Cremer, T. Cremer and I. Solovei (2001). "Arrangements of macro- and microchromosomes in chicken cells." Chromosome Res **9**(7): 569-84.
- Heintzmann, R. (1999). Resolution Enhancement of Biological Light Microscopic Data. Fakultät für Physik. Heidelberg, Rupertus Carola Universität Heidelberg.
- Heitz, E. (1931). "Die Ursache der gesetzmäßigen Zahl, Lage, Form und Größe pflanzlicher Nukleolen." Planta **12**: 775-884.
- Hendrickson, E. A. (1997). "Cell-cycle regulation of mammalian DNA double-strand-break repair." Am J Hum Genet **61**(4): 795-800.
- Hiraoka, Y., A. F. Dernburg, S. J. Parmelee, M. C. Rykowski, D. A. Agard and J. W. Sedat (1993). "The onset of homologous chromosome pairing during Drosophila melanogaster embryogenesis." J Cell Biol **120**(3): 591-600.
- Houtsmuller, A. B., S. Rademakers, A. L. Nigg, D. Hoogstraten, J. H. Hoeijmakers and W. Vermeulen (1999). "Action of DNA repair endonuclease ERCC1/XPF in living cells." Science **284**(5416): 958-61.
- Jackson, S. P. (2001). "Detecting, signalling and repairing DNA double-strand breaks." Biochem Soc Trans **29**(Pt 6): 655-61.
- Jähne, B., H. Haußecker and P. Geißler (1999). Handbook of Computer Vision and Applications. Boston, Massachusetts, USA, Academic Press.
- Johnson, R. D. and M. Jasin (2000). "Sister chromatid gene conversion is a prominent double-strand break repair pathway in mammalian cells." Embo J **19**(13): 3398-407.
- Johnson, R. D. and M. Jasin (2001). "Double-strand-break-induced homologous recombination in mammalian cells." Biochem Soc Trans **29**(Pt 2): 196-201.
- Kanaar, R., J. H. Hoeijmakers and D. C. van Gent (1998). "Molecular mechanisms of DNA double strand break repair." Trends Cell Biol **8**(12): 483-9.
- Kanda, T., K. F. Sullivan and G. M. Wahl (1998). "Histone-GFP fusion protein enables sensitive analysis of chromosome dynamics in living mammalian cells." Curr Biol **8**(7): 377-85.

- Khanna, K. K. and S. P. Jackson (2001). "DNA double-strand breaks: signaling, repair and the cancer connection." Nat Genet **27**(3): 247-54.
- Kimura, H. and P. R. Cook (2001). "Kinetics of core histones in living human cells: little exchange of H3 and H4 and some rapid exchange of H2B." J Cell Biol **153**(7): 1341-53.
- Kino, G. S. (1995). Intermediate Optics in Nipkow Disk Microscopes. Handbook of Biological Confocal Microscopy. J. B. Pawley. New York, Plenum Press.
- Kobayashi, J., H. Tauchi, S. Sakamoto, A. Nakamura, K. Morishima, S. Matsuura, T. Kobayashi, K. Tamai, K. Tanimoto and K. Komatsu (2002). "NBS1 localizes to gamma-H2AX foci through interaction with the FHA/BRCT domain." Curr Biol **12**(21): 1846-51.
- Köhler, D. (2002). Variabilität oder Konstanz der Chromosomenanordnung während des klonalen Wachstums menschlicher Zellen. Department Biologie II, Lehrstuhl für Anthropologie und Humangenetik, LMU Munich.
- Koss, L. G. (1998). "Characteristics of chromosomes in polarized normal human bronchial cells provide a blueprint for nuclear organization." Cytogenet. Cell Genet. **82**(3-4): 230-7.
- Krasin, F. and F. Hutchinson (1978). "Double-strand breaks from single photochemical events in DNA containing 5-bromouracil." Biophys J **24**: 645-656.
- Kruhlak, M. J., M. A. Lever, W. Fischle, E. Verdin, D. P. Bazett-Jones and M. J. Hendzel (2000). "Reduced mobility of the alternate splicing factor (ASF) through the nucleoplasm and steady state speckle compartments." J Cell Biol **150**(1): 41-51.
- Lamond, A. I. and W. C. Earnshaw (1998). "Structure and function in the nucleus." Science **280**(5363): 547-53.
- Lange, C. S., P. J. Mayer and N. M. Reddy (1997). "Tests of the double-strand break, lethal-potentially lethal and repair- misrepair models for mammalian cell survival using data for survival as a function of delayed-plating interval for log-phase Chinese hamster V79 cells." Radiat Res **148**(3): 285-92.
- LaSalle, J. M. and M. Lalande (1996). "Homologous association of oppositely imprinted chromosomal domains." Science **272**(5262): 725-8.
- Leitch, A. R. (2000). "Higher levels of organization in the interphase nucleus of cycling and differentiated cells." Microbiol Mol Biol Rev **64**(1): 138-52.
- Lemke, J., J. Claussen, S. Michel, I. Chudoba, P. Muhlig, M. Westermann, K. Sperling, N. Rubtsov, U. W. Grummt, P. Ullmann, K. Kromeyer-Hauschild, T. Liehr and U. Claussen (2002). "The DNA-Based Structure of Human Chromosome 5 in Interphase." Am J Hum Genet **71**(5): 1051-9.
- Leonhardt, H., H. P. Rahn, P. Weinzierl, A. Sporbert, T. Cremer, D. Zink and M. C. Cardoso (2000). "Dynamics of DNA replication factories in living cells." J Cell Biol **149**(2): 271-80.
- Lesko, S. A., D. E. Callahan, M. E. LaVilla, Z. P. Wang and P. O. Ts'o (1995). "The experimental homologous and heterologous separation distance histograms for the centromeres of chromosomes 7, 11, and 17 in interphase human T-lymphocytes." Exp Cell Res **219**(2): 499-506.
- Lever, M. A., J. P. Th'ng, X. Sun and M. J. Hendzel (2000). "Rapid exchange of histone H1.1 on chromatin in living human cells." Nature **408**(6814): 873-6.
- Limoli, C. L. and J. F. Ward (1993). "A new method for introducing double-strand breaks into cellular DNA." Radiat Res **134**(2): 160-9.
- Liu, Y. and N. Maizels (2000). "Coordinated response of mammalian Rad51 and Rad52 to DNA damage." EMBO Rep **1**(1): 85-90.
- Lucas, J. N. and E. Cervantes (2002). "Significant large-scale chromosome territory movement occurs as a result of mitosis, but not during interphase." Int J Radiat Biol **78**(6): 449-55.
- Lukas, C., J. Falck, J. Bartkova, J. Bartek and J. Lukas (2003). "Distinct spatiotemporal dynamics of mammalian checkpoint regulators induced by DNA damage." Nat Cell Biol **24**: 24.
- Manders, E. M., H. Kimura and P. R. Cook (1999). "Direct imaging of DNA in living cells reveals the dynamics of chromosome formation." J Cell Biol **144**(5): 813-21.
- Manuelidis, L. (1985). "Individual interphase chromosome domains revealed by in situ hybridization." Hum Genet **71**(4): 288-93.
- Marshall, W. F. (2002). "Order and disorder in the nucleus." Curr Biol **12**(5): R185-92.

- Martou, G. and U. De Boni (2000). "Nuclear topology of murine, cerebellar Purkinje neurons: changes as a function of development." *Exp Cell Res* **256**(1): 131-9.
- Maser, R. S., K. J. Monsen, B. E. Nelms and J. H. Petrini (1997). "hMre11 and hRad50 nuclear foci are induced during the normal cellular response to DNA double-strand breaks." *Mol Cell Biol* **17**(10): 6087-96.
- Maul, G. G., D. Negorev, P. Bell and A. M. Ishov (2000). "Review: properties and assembly mechanisms of ND10, PML bodies, or PODs." *J Struct Biol* **129**(2-3): 278-87.
- McNally, J. G., T. Karpova, J. Cooper and J. A. Conchello (1999). "Three-dimensional imaging by deconvolution microscopy." *Methods* **19**(3): 373-85.
- McNally, J. G., W. G. Muller, D. Walker, R. Wolford and G. L. Hager (2000). "The glucocorticoid receptor: rapid exchange with regulatory sites in living cells." *Science* **287**(5456): 1262-5.
- Meisterernst, M. and R. G. Roeder (1991). "Family of proteins that interact with TFIID and regulate promoter activity." *Cell* **67**(3): 557-67.
- Minski, M. (1957). Microscopy Apparatus. patent USA
- Mirzoeva, O. K. and J. H. Petrini (2001). "DNA damage-dependent nuclear dynamics of the Mre11 complex." *Mol Cell Biol* **21**(1): 281-8.
- Misteli, T. (2000). "Cell biology of transcription and pre-mRNA splicing: nuclear architecture meets nuclear function." *J Cell Sci* **113**(Pt 11): 1841-9.
- Misteli, T. (2001). "Protein dynamics: implications for nuclear architecture and gene expression." *Science* **291**(5505): 843-7.
- Misteli, T., A. Gunjan, R. Hock, M. Bustin and D. T. Brown (2000). "Dynamic binding of histone H1 to chromatin in living cells." *Nature* **408**(6814): 877-81.
- Miyagawa, K., T. Tsuruga, A. Kinomura, K. Usui, M. Katsura, S. Tashiro, H. Mishima and K. Tanaka (2002). "A role for RAD54B in homologous recombination in human cells." *Embo J* **21**(1-2): 175-80.
- Morita, T., Y. Yoshimura, A. Yamamoto, K. Murata, M. Mori, H. Yamamoto and A. Matsushiro (1993). "A mouse homolog of the Escherichia coli recA and Saccharomyces cerevisiae RAD51 genes." *Proc Natl Acad Sci U S A* **90**(14): 6577-80.
- Moynahan, M. E. and M. Jasin (1997). "Loss of heterozygosity induced by a chromosomal double-strand break." *Proc Natl Acad Sci U S A* **94**(17): 8988-93.
- Nagele, R. G., T. Freeman, L. McMorrow and H. Y. Lee (1995). "Precise spatial positioning of chromosomes during prometaphase: evidence for chromosomal order." *Science* **270**(5243): 1831-5.
- Nagele, R. G., T. Freeman, L. McMorrow, Z. Thomson, K. Kitson-Wind and H. Lee (1999). "Chromosomes exhibit preferential positioning in nuclei of quiescent human cells." *J Cell Sci* **112**(Pt 4): 525-35.
- Natarajan, A. T., A. H. Rotteveel, J. van Pieterse and M. G. Schliermann (1986). "Influence of incorporated 5-bromodeoxyuridine on the frequencies of spontaneous and induced sister-chromatid exchanges, detected by immunological methods." *Mutat Res* **163**(1): 51-5.
- Nefkens, I., D. G. Negorev, A. M. Ishov, J. S. Michaelson, E. T. Yeh, R. M. Tanguay, W. E. Muller and G. G. Maul (2003). "Heat shock and Cd(2+) exposure regulate PML and Daxx release from ND10 by independent mechanisms that modify the induction of heat-shock proteins 70 and 25 differently." *J Cell Sci* **116**(Pt 3): 513-524.
- Nelms, B. E., R. S. Maser, J. F. MacKay, M. G. Lagally and J. H. Petrini (1998). "In situ visualization of DNA double-strand break repair in human fibroblasts." *Science* **280**(5363): 590-2.
- Parada, L. and T. Misteli (2002). "Chromosome positioning in the interphase nucleus." *Trends Cell Biol* **12**(9): 425.
- Patterson, G. H., S. M. Knobel, W. D. Sharif, S. R. Kain and D. W. Piston (1997). "Use of the green fluorescent protein and its mutants in quantitative fluorescence microscopy." *Biophys J* **73**(5): 2782-90.
- Patterson, G. H. and D. W. Piston (2000). "Photobleaching in two-photon excitation microscopy." *Biophys J* **78**(4): 2159-62.
- Paull, T. T. and M. Gellert (1998). "The 3' to 5' exonuclease activity of Mre 11 facilitates repair of DNA double-strand breaks." *Mol Cell* **1**(7): 969-79.

- Paull, T. T., E. P. Rogakou, V. Yamazaki, C. U. Kirchgessner, M. Gellert and W. M. Bonner (2000). "A critical role for histone H2AX in recruitment of repair factors to nuclear foci after DNA damage." *Curr Biol* **10**(15): 886-95.
- Pawley, J. B. (1995a). *Fundamental Limits in Confocal Microscopy*. Handbook of Biological Confocal Microscopy. J. B. Pawley. New York, Plenum Press.
- Pawley, J. B., Ed. (1995b). Handbook of Biological Confocal Microscopy. New York, Plenum Press.
- Pellegrini, L., D. S. Yu, T. Lo, S. Anand, M. Lee, T. L. Blundell and A. R. Venkitaraman (2002). "Insights into DNA recombination from the structure of a RAD51-BRCA2 complex." *Nature* **420**(6913): 287-293.
- Peterson, S. P. and M. W. Berns (1978). "Evidence for centriolar region RNA functioning in spindle formation in dividing PTK2 cells." *J Cell Sci* **34**: 289-301.
- Pfeiffer, P., W. Goedecke and G. Obe (2000). "Mechanisms of DNA double-strand break repair and their potential to induce chromosomal aberrations." *Mutagenesis* **15**(4): 289-302.
- Phair, R. D. and T. Misteli (2000). "High mobility of proteins in the mammalian cell nucleus." *Nature* **404**(6778): 604-9.
- Quignon, F., F. De Bels, M. Koken, J. Feunteun, J. C. Ameisen and H. de The (1998). "PML induces a novel caspase-independent death process." *Nat Genet* **20**(3): 259-65.
- Rabl, C. (1885). "Über Zelltheilung." *Morphologisches Jahrbuch* **10**: 214-330.
- Raderschall, E., A. Bazarov, J. Cao, R. Lurz, A. Smith, W. Mann, H. H. Ropers, J. M. Sedivy, E. I. Golub, E. Fritz and T. Haaf (2002a). "Formation of higher-order nuclear Rad51 structures is functionally linked to p21 expression and protection from DNA damage-induced apoptosis." *J Cell Sci* **115**(Pt 1): 153-64.
- Raderschall, E., E. I. Golub and T. Haaf (1999). "Nuclear foci of mammalian recombination proteins are located at single-stranded DNA regions formed after DNA damage." *Proc Natl Acad Sci U S A* **96**(5): 1921-6.
- Raderschall, E., K. Stout, S. Freier, V. Suckow, S. Schweiger and T. Haaf (2002b). "Elevated levels of Rad51 recombination protein in tumor cells." *Cancer Res* **62**(1): 219-25.
- Ramsden, D. A. and M. Gellert (1998). "Ku protein stimulates DNA end joining by mammalian DNA ligases: a direct role for Ku in repair of DNA double-strand breaks." *Embo J* **17**(2): 609-14.
- Rasband, W. S. (1997-2003). ImageJ National Institutes of Health, Bethesda, Maryland, USA <http://rsb.info.nih.gov/ij/>
- Redon, C., D. Pilch, E. Rogakou, O. Sedelnikova, K. Newrock and W. M. Bonner (2002). "Histone H2A variants H2AX and H2AZ." *Curr Opin Genet Dev* **12**(2): 162-9.
- Reichenzeller, M., A. Burzlaff, P. Lichter and H. Herrmann (2000). "In vivo observation of a nuclear channel-like system: evidence for a distinct interchromosomal domain compartment in interphase cells." *J Struct Biol* **129**(2-3): 175-85.
- Reits, E. A. and J. J. Neefjes (2001). "From fixed to FRAP: measuring protein mobility and activity in living cells." *Nat Cell Biol* **3**(6): E145-7.
- Rogakou, E. P., C. Boon, C. Redon and W. M. Bonner (1999). "Megabase chromatin domains involved in DNA double-strand breaks in vivo." *J Cell Biol* **146**(5): 905-16.
- Rogakou, E. P., D. R. Pilch, A. H. Orr, V. S. Ivanova and W. M. Bonner (1998). "DNA double-stranded breaks induce histone H2AX phosphorylation on serine 139." *J Biol Chem* **273**(10): 5858-68.
- Rothkamm, K. and M. Lobrich (2003). "Evidence for a lack of DNA double-strand break repair in human cells exposed to very low x-ray doses." *Proc Natl Acad Sci U S A* **4**: 4.
- Rydberg, B. (1996). "Clusters of DNA damage induced by ionizing radiation: formation of short DNA fragments. II. Experimental detection." *Radiat Res* **145**(2): 200-9.
- Schärer, O. D. (2003). "Chemistry and biology of DNA repair." *Angew Chem Int Ed Engl* **42**(26): 2946-74.
- Schermelleh, L. (2003). *Dynamic organization of chromosomes in the mammalian cell nucleus*. Department Biologie II, Lehrstuhl für Anthropologie und Humangenetik. München, LMU München.
- Schermelleh, L., I. Solovei, D. Zink and T. Cremer (2001). "Two-color fluorescence labeling of early and mid-to-late replicating chromatin in living cells." *Chromosome Res* **9**(1): 77-80.

- Schultz, L. B., N. H. Chehab, A. Malikzay and T. D. Halazonetis (2000). "p53 binding protein 1 (53BP1) is an early participant in the cellular response to DNA double-strand breaks." J Cell Biol **151**(7): 1381-90.
- Scully, R., J. Chen, R. L. Ochs, K. Keegan, M. Hoekstra, J. Feunteun and D. M. Livingston (1997a). "Dynamic changes of BRCA1 subnuclear location and phosphorylation state are initiated by DNA damage." Cell **90**(3): 425-35.
- Scully, R., J. Chen, A. Plug, Y. Xiao, D. Weaver, J. Feunteun, T. Ashley and D. M. Livingston (1997b). "Association of BRCA1 with Rad51 in mitotic and meiotic cells." Cell **88**(2): 265-75.
- Shaw, P. J. (1995). Comparison of Wide-Field/Deconvolution and Confocal Microscopy for 3D Imaging. Handbook of Biological Confocal Microscopy. J. B. Pawley. New York, Plenum Press.
- Shelby, R. D., K. M. Hahn and K. F. Sullivan (1996). "Dynamic elastic behavior of alpha-satellite DNA domains visualized in situ in living human cells." J Cell Biol **135**(3): 545-57.
- Shen, Z., K. G. Cloud, D. J. Chen and M. S. Park (1996). "Specific interactions between the human RAD51 and RAD52 proteins." J Biol Chem **271**(1): 148-52.
- Shinohara, A., H. Ogawa, Y. Matsuda, N. Ushio, K. Ikeo and T. Ogawa (1993). "Cloning of human, mouse and fission yeast recombination genes homologous to RAD51 and recA." Nat Genet **4**(3): 239-43.
- Shinohara, A., H. Ogawa and T. Ogawa (1992). "Rad51 protein involved in repair and recombination in *S. cerevisiae* is a RecA-like protein." Cell **69**(3): 457-70.
- Siede, W., A. A. Friedl, I. Dianova, F. Eckardt-Schupp and E. C. Friedberg (1996). "The *Saccharomyces cerevisiae* Ku autoantigen homologue affects radiosensitivity only in the absence of homologous recombination." Genetics **142**(1): 91-102.
- Skalnikova, M., S. Kozubek, E. Lukasova, E. Bartova, P. Jirsova, A. Cafourkova, I. Koutna and M. Kozubek (2000). "Spatial arrangement of genes, centromeres and chromosomes in human blood cell nuclei and its changes during the cell cycle, differentiation and after irradiation." Chromosome Res **8**(6): 487-99.
- Smith, G. C. and S. P. Jackson (1999). "The DNA-dependent protein kinase." Genes Dev **13**(8): 916-34.
- Snaar, S., K. Wiesmeijer, A. G. Jochemsen, H. J. Tanke and R. W. Dirks (2000). "Mutational analysis of fibrillarin and its mobility in living human cells." J Cell Biol **151**(3): 653-62.
- Solovei, I., J. Walter, M. Cremer, F. Habermann, L. Schermelleh and T. Cremer (2002). FISH on Three-dimensionally Preserved Nuclei. FISH: a practical approach. B. Beatty, S. Mai and J. Squire. Oxford, Oxford University Press: 119-157.
- Song, B. and P. Sung (2000). "Functional interactions among yeast Rad51 recombinase, Rad52 mediator, and replication protein A in DNA strand exchange." J Biol Chem **275**(21): 15895-904.
- Spector, D. L. (1996). "Nuclear organization and gene expression." Exp Cell Res **229**(2): 189-97.
- Sporbert, A., A. Gahl, R. Ankerhold, H. Leonhardt and M. C. Cardoso (2002). "DNA polymerase clamp shows little turnover at established replication sites but sequential de novo assembly at adjacent origin clusters." Mol Cell **10**(6): 1355-65.
- Stenoién, D. L., K. Patel, M. G. Mancini, M. Dutertre, C. L. Smith, B. W. O'Malley and M. A. Mancini (2001). "FRAP reveals that mobility of oestrogen receptor-alpha is ligand- and proteasome-dependent." Nat Cell Biol **3**(1): 15-23.
- Stetka, D. G. and A. V. Carrano (1977). "The interaction of Hoechst 33258 and BrdU substituted DNA in the formation of sister chromatid exchanges." Chromosoma **63**(1): 21-31.
- Sugiyama, T. and S. C. Kowalczykowski (2002). "Rad52 protein associates with replication protein A (RPA)-single-stranded DNA to accelerate Rad51-mediated displacement of RPA and presynaptic complex formation." J Biol Chem **277**(35): 31663-72.
- Sun, H. B., J. Shen and H. Yokota (2000). "Size-dependent positioning of human chromosomes in interphase nuclei." Biophys J **79**(1): 184-90.
- Sun, H. B. and H. Yokota (1999). "Correlated positioning of homologous chromosomes in daughter fibroblast cells." Chromosome Res **7**(8): 603-10.

- Swaminathan, R., C. P. Hoang and A. S. Verkman (1997). "Photobleaching recovery and anisotropy decay of green fluorescent protein GFP-S65T in solution and cells: cytoplasmic viscosity probed by green fluorescent protein translational and rotational diffusion." *Biophys J* **72**(4): 1900-7.
- Symington, L. S. (2002). "Role of RAD52 Epistasis Group Genes in Homologous Recombination and Double-Strand Break Repair." *Microbiol Mol Biol Rev* **66**(4): 630-670.
- Tanabe, H., F. A. Habermann, I. Solovei, M. Cremer and T. Cremer (2002a). "Non-random radial arrangements of interphase chromosome territories: evolutionary considerations and functional implications." *Mutat Res* **504**(1-2): 37-45.
- Tanabe, H., S. Muller, M. Neusser, J. von Hase, E. Calcagno, M. Cremer, I. Solovei, C. Cremer and T. Cremer (2002b). "Evolutionary conservation of chromosome territory arrangements in cell nuclei from higher primates." *Proc Natl Acad Sci U S A* **99**(7): 4424-4429.
- Tarsounas, M., D. Davies and S. C. West (2003). "BRCA2-dependent and independent formation of RAD51 nuclear foci." *Oncogene* **22**(8): 1115-23.
- Tashiro, S., N. Kotomura, A. Shinohara, K. Tanaka, K. Ueda and N. Kamada (1996). "S phase specific formation of the human Rad51 protein nuclear foci in lymphocytes." *Oncogene* **12**(10): 2165-70.
- Tashiro, S., J. Walter, A. Shinohara, N. Kamada and T. Cremer (2000). "Rad51 accumulation at sites of DNA damage and in postreplicative chromatin." *J Cell Biol* **150**(2): 283-91.
- Terasawa, M., A. Shinohara, Y. Hotta, H. Ogawa and T. Ogawa (1995). "Localization of RecA-like recombination proteins on chromosomes of the lily at various meiotic stages." *Genes Dev* **9**(8): 925-34.
- Trujillo, K. M., S. S. Yuan, E. Y. Lee and P. Sung (1998). "Nuclease activities in a complex of human recombination and DNA repair factors Rad50, Mre11, and p95." *J Biol Chem* **273**(34): 21447-50.
- Tschachotin, S. (1912). "Die mikroskopische Strahlenstichmethode, eine Zelloperationsmethode." *Biol Centralblatt* **32**: 623-630.
- Tsien, R. Y. and B. J. Bacskai (1995). Video-Rate Confocal Microscopy. *Handbook of Biological Confocal Microscopy*. J. B. Pawley. New York, Plenum Press.
- Tumbar, T. and A. S. Belmont (2001). "Interphase movements of a DNA chromosome region modulated by VP16 transcriptional activator." *Nat Cell Biol* **3**(2): 134-9.
- Van Dyck, E., N. M. Hajibagheri, A. Stasiak and S. C. West (1998). "Visualisation of human rad52 protein and its complexes with hRad51 and DNA." *J Mol Biol* **284**(4): 1027-38.
- Van Dyck, E., A. Z. Stasiak, A. Stasiak and S. C. West (1999). "Binding of double-strand breaks in DNA by human Rad52 protein." *Nature* **398**(6729): 728-31.
- van Rongen, E., H. D. Thames, Jr. and E. L. Travis (1993). "Recovery from radiation damage in mouse lung: interpretation in terms of two rates of repair." *Radiat Res* **133**(2): 225-33.
- Varon, R., C. Vissinga, M. Platzer, K. M. Cerosaletti, K. H. Chrzanowska, K. Saar, G. Beckmann, E. Seemanova, P. R. Cooper, N. J. Nowak, M. Stumm, C. M. Weemaes, R. A. Gatti, R. K. Wilson, M. Digweed, A. Rosenthal, K. Sperling, P. Concannon and A. Reis (1998). "Nibrin, a novel DNA double-strand break repair protein, is mutated in Nijmegen breakage syndrome." *Cell* **93**(3): 467-76.
- Vig, B. K. and M. Willcourt (1998). "Decondensation of pericentric heterochromatin alters the sequence of centromere separation in mouse cells." *Chromosoma* **107**(6-7): 417-23.
- Volpi, E. V., E. Chevret, T. Jones, R. Vatcheva, J. Williamson, S. Beck, R. D. Campbell, M. Goldsworthy, S. H. Powis, J. Ragoussis, J. Trowsdale and D. Sheer (2000). "Large-scale chromatin organization of the major histocompatibility complex and other regions of human chromosome 6 and its response to interferon in interphase nuclei." *J Cell Sci* **113**(Pt 9): 1565-76.
- von Mikecz, A., S. Zhang, M. Montminy, E. M. Tan and P. Hemmerich (2000). "CREB-binding protein (CBP)/p300 and RNA polymerase II colocalize in transcriptionally active domains in the nucleus." *J Cell Biol* **150**(1): 265-73.
- Walter, J., T. Cremer, K. Miyagawa and S. Tashiro (2003a). "A new system for laser-UVA-microirradiation of living cells." *J Microsc* **209**(2): 71-75.

- Walter, J., L. Schermelleh, M. Cremer, S. Tashiro and T. Cremer (2003b). "Chromosome order in HeLa cells changes during mitosis and early G1, but is stably maintained during subsequent interphase stages." J Cell Biol **160**(5): 685-97.
- Wang, Z. G., D. Ruggero, S. Ronchetti, S. Zhong, M. Gaboli, R. Rivi and P. P. Pandolfi (1998). "PML is essential for multiple apoptotic pathways." Nat Genet **20**(3): 266-72.
- Ward, I. M. and J. Chen (2001). "Histone H2AX is phosphorylated in an ATR-dependent manner in response to replicational stress." J Biol Chem **276**(51): 47759-62.
- White, J. and E. Stelzer (1999). "Photobleaching GFP reveals protein dynamics inside live cells." Trends Cell Biol **9**(2): 61-5.
- Williams, R. R. and A. G. Fisher (2003). "Chromosomes, positions please!" Nat Cell Biol **5**(5): 388-90.
- Wong, A. K., R. Pero, P. A. Ormonde, S. V. Tavtigian and P. L. Bartel (1997). "RAD51 interacts with the evolutionarily conserved BRC motifs in the human breast cancer susceptibility gene *brca2*." J Biol Chem **272**(51): 31941-4.
- Xia, S. J., M. A. Shamma and R. J. Shmookler Reis (1996). "Reduced telomere length in ataxia-telangiectasia fibroblasts." Mutat Res **364**(1): 1-11.
- Yamamoto, A., T. Taki, H. Yagi, T. Habu, K. Yoshida, Y. Yoshimura, K. Yamamoto, A. Matsushiro, Y. Nishimune and T. Morita (1996). "Cell cycle-dependent expression of the mouse Rad51 gene in proliferating cells." Mol Gen Genet **251**(1): 1-12.
- Zhu, X., J. M. Dunn, A. D. Goddard, J. A. Squire, A. Becker, R. A. Phillips and B. L. Gallie (1992). "Mechanisms of loss of heterozygosity in retinoblastoma." Cytogenet Cell Genet **59**(4): 248-52.
- Zink, D., T. Cremer, R. Saffrich, R. Fischer, M. F. Trendelenburg, W. Ansorge and E. H. Stelzer (1998). "Structure and dynamics of human interphase chromosome territories in vivo." Hum Genet **102**(2): 241-51.
- Zöfel, P. (2001). Statistik verstehen. München, Addison-Wesley.
- Zorn, C., C. Cremer, T. Cremer and J. Zimmer (1979). "Unscheduled DNA synthesis after partial UV irradiation of the cell nucleus. Distribution in interphase and metaphase." Exp. Cell Res. **124**(1): 111-9.
- Zorn, C., T. Cremer, C. Cremer and J. Zimmer (1976). "Laser UV microirradiation of interphase nuclei and post-treatment with caffeine. A new approach to establish the arrangement of interphase chromosomes." Hum Genet **35**(1): 83-9.

Appendix

Abbreviations

AOTF	acousto-optical tunable filter
CFP	cyan fluorescent protein
CT	chromosome territory
CTD	carboxy-terminal domain of RNA Pol II
DNA-PK	DNA dependent protein kinase
DNA-PKcs	DNA dependent protein kinase catalytic subunit
DSB	double-strand break
FRAP	fluorescence recovery after photobleaching
GFP	green fluorescent protein
γ -H2AX	phosphorylated histone H2AX
HRR	homologous recombination repair
IC	interchromatin compartment
LMDS	locally multiply damaged site
MRN/MRX	protein complex of Mre11-Rad50-NBS1/Xrs1
NHEJ	non-homologous end joining
PC	personal computer
PI	propidium iodide
PSF	point spread function
RAC	radial autocorrelation function
R.I.	refractive index
RNA Pol II	RNA polymerase II
ROI	region of interest
RPA	replication protein A
S/N	signal to noise ratio
SSA	single-strand annealing
ssDNA	single-stranded DNA
SRL	scratch replication labeling
UV	ultraviolet light (wavelength 100 - 400 nm)
UVA	ultraviolet light with wavelenghts 320 - 400 nm
YFP	yellow fluorescent protein

Contents of the supplemental CD

The supplemental CD contains PDF-files of this thesis in three sizes: one file with uncompressed images, one file with compressed images of high quality and one small file with strongly compressed images (lower quality). In addition there is a version of the thesis with comments, which link the results described in the thesis to the primary data.

The directory "Video" contains a quicktime movie showing the progression of the cells displayed in Figure 3.35 through mitosis.

The directory "Literature" contains PDF-files of the cited papers, theses and patent as far as they were accessible to me. Notably, scanned versions of the Limoli and Ward paper (1993) describing the BrdU/Hoechst sensitization method and of Minsky's patent on the confocal microscope (1957) are included.

The directory "Software" contains add-ons to several programs I wrote and used for this work:

1. "Amira-scripts" contains scripts for loading image stacks and time series into Amira™ and for facilitating their display.
2. "ImageJ-plugins" contains plugins (source files and Java bytecode files) used to for the first processing steps the primary data and to do quantitative evaluations with ImageJ. In particular it contains the Sync_Windows and Sync_Measure_3D plugins for simultaneously displaying several color channels and measuring positions, distances and Volumes and the plugins used to evaluate the radial distribution and the degree of spreading of unbleached chromatin patches in H2B-GFP HeLa cells.
3. "LSM410-macros" contains macros for the LSM 410 and for the dummy software of the LSM 410 ("LSMdummy"). Most notable are "Jwdual" / "Jwtriple" for recording confocal serial sections of specimen with two or three fluorochromes and the "TimePr" macros for recording time series of 3D image stacks. It also contains a full installation of the LSMdummy software downloaded from the Zeiss FTP-server. The microscope parameters come from the LSM 410 used in our lab, and the macros are installed.
4. "LSM510-Microirradiation" contains the VBA-scripts for the LSM 510 macro language used to perform microirradiation with the LSM 510 with UV-laser for laser-scanning.

Danksagung

An erster Stelle danke ich meinem Doktorvater Prof. Thomas Cremer für die engagierte Betreuung meiner Arbeit und das Verständnis für die Nöte eines Physikers in ungewohnter Umgebung. Seine Begeisterung für die Zellkernarchitektur und sein breit gefächertes wissenschaftliches Interesse haben mich immer wieder aufs Neue angespornt.

Dr. Satoshi Tashiro introduced me to the “complex story” of DNA repair. I am deeply indebted to him for tutoring my first steps in cell culture and immunostaining. Together with him I performed the microirradiation experiments, and the experiments concerning the distribution of Rad51 in undamaged cells. It was delightful to work with him and to experience his cheerful but - “you know” - serious approach to things.

Ein bedeutender Teil der Arbeit, der die Lebendzelleexperimente zur Beobachtung der CT-Dynamik umfasst, ist in enger Zusammenarbeit mit Lothar Schermelleh entstanden. Ihm gilt deshalb mein Dank für diese äußerst produktive und fruchtbare Zeit und meine Bewunderung für sein methodisches Geschick und sein Streben nach Perfektion.

Dr. Marion Cremer hat mich in die FISH-Technik eingewiesen und mich auch ansonsten mit Rat und Tat unterstützt. Dafür vielen Dank! Besonders wird mir unser gemeinsames Ringen um englische Formulierungen in Erinnerung bleiben.

Dr. Irina Solovei und Alessandro Brero danke ich für ihre stets vorhandene Hilfsbereitschaft und die perfekte Organisation des Labors.

Prof. Cristoph Cremer hat mich durch eine einjährige Finanzierung unterstützt. Dafür und für viele interessante Diskussionen mit ihm möchte ich mich bedanken. Weiterhin gilt mein Dank den Mitgliedern seiner Arbeitsgruppe für die Unterstützung in Fragen der Mikroskopie und der Auswertung, besonders Dr. Rainer Heintzmann für die anregenden Gespräche über die Theorie der Mikroskopabbildung.

Frau Prof. Eckardt-Schupp danke ich für den fruchtbaren Gedankenaustausch mit ihr und ihrer Arbeitsgruppe und für die Übernahme des Zweitgutachtens.

Bei Dr. Anna Friedl möchte ich mich für das Durchlesen der Arbeit und die hilfreichen Anregungen zur Verbesserung bedanken.

Prof. Heinrich Leonhardt und Dr. Cristina Cardoso haben mir einen zweiwöchigen Forschungsaufenthalt an der Franz-Volhard-Klinik in Berlin-Buch ermöglicht. Dafür vielen Dank.

Thanks to Dr. Tashiro I had the opportunity to stay in Hiroshima for five months and do research at the University of Hiroshima. I am grateful for the kind hospitality with which Prof. Igarashi and his group welcomed me to their lab in the Department of Biomedical Chemistry, and I gladly remember my time with them from my first Okonomi-yaki to my leaving party including Karaoke. I would like to thank Prof. Miyagawa from the institute of radiation research for the productive collaboration and for financing two months of my stay in Hiroshima. Big thanks also to Prof. Inaba for his help in “social engineering”, which made it possible for me to use the LSM 510 in the institute of radiation research.

Prof. Rainer Uhl danke ich dafür, dass er mir die Zeit gegeben hat, neben meiner Tätigkeit bei Till I.D. diese Arbeit abzuschließen.

Kurt Scudder from Biolume helped me to connect the perfusion pump of our live cell imaging system to the control PC of the LSM 410. Thanks a lot for that!

Schließlich möchte ich mich bei allen Mitgliedern der AG Cremer für die sehr angenehme Arbeitsatmosphäre, die große Hilfsbereitschaft und den regen wissenschaftlichen Austausch bedanken. Nicht zu vergessen Umräumarbeiten im

Keller, Schaschlikparties an der Isar, den Fakultätstag im eigenen Institut, Eisessen im Innenhof, einen Ausflug nach Holland und vieles andere mehr.

Vor allem aber danke ich meinen Eltern dafür, dass sie mir während dieser Zeit mit Liebe und Verständnis zur Seite standen.

Lebenslauf

<i>Name</i>	Joachim Walter
<i>Geburtsdatum</i>	2. April 1970
<i>Geburtsort</i>	Kassel
<i>08/1976 - 07/1982</i>	Grundschule und Förderstufe Witzenhausen
<i>08/1982 - 05/1989</i>	Grotefend-Gymnasium Hannoversch Münden
<i>06/1989 - 08/1990</i>	Wehrdienst bei der 3./Panzeraufklärungsbataillon 2 in Hessisch Lichtenau
<i>10/1990 - 10/1997</i>	Physikstudium (Diplom) an der Universität Heidelberg
<i>währenddessen</i>	
<i>10/1992 - 09/1993</i>	Studium an der University of Oklahoma im Rahmen eines Austauschprogramms
<i>07/1996 - 09/1997</i>	Diplomarbeit am Europäischen Molekularbiologie Laboratorium (EMBL) Heidelberg in der Arbeitsgruppe von Prof. Oschkinat zum Thema „ <i>Mustererkennung in dreidimensionalen NMR-Spektren von Proteinen zur automatischen Zuordnung und Strukturbestimmung</i> “
<i>seit 02/1998</i>	Promotion am Institut für Anthropologie und Humangenetik, Fakultät für Biologie der LMU München, AG Cremer
<i>währenddessen</i>	
<i>02/2001 - 06/2001</i>	Forschungsaufenthalt am Department of Biomedical Chemistry der Universität Hiroshima
<i>seit 03/2002</i>	Beschäftigt bei Till I.D. als wissenschaftlicher Entwickler

List of Publications

- Walter, J., L. Schermelleh, M. Cremer, S. Tashiro and T. Cremer (2003). "Chromosome order in HeLa cells changes during mitosis and early G1, but is stably maintained during subsequent interphase stages." J Cell Biol **160**(5): 685-97.
- Walter, J., T. Cremer, K. Miyagawa and S. Tashiro (2003). "A new system for laser-UVA-microirradiation of living cells." J Microsc **209**(2): 71-75.
- Schermelleh, L., and J. Walter (2002). "Long term live cell confocal microscopy." G.I.T. Imaging & Microscopy **4**: 47-50 and (2003) BIOforum International **7**: 48-50.
- Solovei, I., J. Walter, M. Cremer, F. Habermann, L. Schermelleh and T. Cremer (2002). FISH on Three-dimensionally Preserved Nuclei. FISH: a practical approach. B. Beatty, S. Mai and J. Squire. Oxford, Oxford University Press: 119-157.
- Habermann, F. A., M. Cremer, J. Walter, G. Kreth, J. von Hase, K. Bauer, J. Wienberg, C. Cremer, T. Cremer and I. Solovei (2001). "Arrangements of macro- and microchromosomes in chicken cells." Chromosome Res **9**(7): 569-84.
- Cremer, M., J. von Hase, T. Volm, A. Brero, G. Kreth, J. Walter, C. Fischer, I. Solovei, C. Cremer and T. Cremer (2001). "Non-random radial higher-order chromatin arrangements in nuclei of diploid human cells." Chromosome Res **9**(7): 541-67.
- Tashiro, S., J. Walter, A. Shinohara, N. Kamada and T. Cremer (2000). "Rad51 accumulation at sites of DNA damage and in postreplicative chromatin." J Cell Biol **150**(2): 283-91.
- Jasencakova, Z., A. Meister, J. Walter, B. M. Turner and I. Schubert (2000). "Histone H4 acetylation of euchromatin and heterochromatin is cell cycle dependent and correlated with replication rather than with transcription." Plant Cell **12**(11): 2087-100.